QUANTIFYING THE EFFECTS OF PROCESSING AND DETERIORATING ENVIRONMENTS ON POLYPROPYLENE BY INFRARED MICROSCOPY

Vom Fachbereich Chemie
der Technischen Universität Darmstadt

zur Erlangung des akademischen Grades eines

Doctor rerum naturalium (Dr. rer. nat.)

genehmigte
Dissertation

vorgelegt von

M. Sc. Subin Damodaran
aus Kerala, India

Referent:	Professor Dr. Matthias Rehahn
Korreferent:	Professor Dr. Markus Busch
Tag der Einreichung:	30.03.2016
Tag der mündlichen Prüfung:	23.05.2016

Darmstadt 2016
D 17

Diese Arbeit wurde unter der Leitung von Herrn Professor Dr. Matthias Rehahn in der Zeit von Januar 2012 bis November 2014 am Fraunhofer LBF (ehemals Deutsches Kunststoff-Institut, DKI) durchgeführt.

Journal articles

1. **S. Damodaran**, T. Schuster, K. Rode, A. Sanoria, R. Brüll, N. Stöhr.
   Measuring the orientation of chains in polypropylene welds by infrared microscopy: A tool to understand the impact of thermo-mechanical treatment and processing.
   Polymer (2015) 60, 125-136.

2. **S. Damodaran**, T. Schuster, K. Rode, A. Sanoria, R. Brüll, M. Wenzel, M. Bastian.
   Monitoring the effect of chlorine on the ageing of polypropylene pipes by infrared microscopy.
   Polym. Degrad. Stab. (2015) 111, 7-19.

3. T. Schuster, **S. Damodaran**, K. Rode, F. Malz, R. Brüll, B. Gerets, M. Wenzel, M. Bastian.
   Quantification of highly oriented nucleating agent in PP-R by IR-microscopy, polarised light microscopy, differential scanning calorimetry and nuclear magnetic resonance spectroscopy.
   Polymer (2014) 44, 1724-1736.

4. **S. Damodaran**, T. Schuster, K. Rode, A. Sanoria, R. Brüll, M. Wenzel, M. Bastian.
   Influence of the morphology of polypropylene on deterioration with chlorinated water. 2015 (in preparation)

Poster presentations

1. Effect of Chlorinated hot water on Pipes Alpha and Beta Polypropylene.
   5th International Conference on Polyolefin Characterization (ICPC), Valencia, Spain, 23 Sept. 2014.

2. Three dimensional orientations by FT-IR and polyrized light microscopy.
   21st World Forum on Advanced Polymers and Materials (Polychar 21), Gwangju, Korea, 11 March 2013

Dedicated to the passionate researchers in the realm of polyolefins……

To begin with, I would like to thank Prof. Dr. Matthias Rehahn who gave me the opportunity to work in his research group. I am also thankful to him for providing me a challenging research topic.

I most gratefully record that the work imbibed in this project is solely due to deep insight and vision of my guide and supervisor, Dr. Robert Brüll. Besides being moral support all through for the execution of my work, critical discussions and his meticulous approach towards my experimental work have not only proved valuable for the project but they, I am sure, will go a long way to mold my future research career and for this I shall ever remain indebted.

I would like to express my gratitude to Karsten Rode, Tobias Schuster and Abhishek Sanoria for their friendship, moral support and scientific contributions during this study.

I acknowledge Prabhu Kavimani Nagar for his help with the SEC measurements.

I thank Dr. Mirko Wenzel for his help with the OIT measurements at the Süddeutsches Kunststoff-Zentrum (SKZ).

I am thankful to all my past and present colleagues of Fraunhofer LBF and DKI for the pleasant working atmosphere.

I feel a deep sense of gratitude for my parents, brother and sister for their encouragement, support and patience during the course of my PhD as well their support to reach my goals during my life.

Table of Contents

Abbreviations

PE	Polyethylene
PP	Polypropylene
MMD	Molar mass distribution
PP-H	Polypropylene homo polymer
PP-R	Polypropylene random copolymer
iPP	Isotactic polypropylene
aPP	Atactic polypropylene
sPP	Syndiotactic polypropylene
α	Alpha
β	Beta
γ	Gamma
M	Slope
ORP	Oxidation reduction potential
AO	Antioxidant
IR	Infrared
ATR	Attenuated total reflectance spectroscopy
μFT-IR	Infrared microscopy
E_1	Excited energy level
E_0	Ground energy level
MD	Machine direction
TD	Transverse direction
ND	Normal direction
DSC	Differential scanning calorimetry
SEC	Size exclusion chromatography
DI	Dispersity index
M_i	Molecular mass of a chain
n_i	Number of chains of a particular molecular mass
PLM	Polarized light microscopy

HPLC	High performance liquid chromatography
OIT	Oxidative induction time

Physical constants

h	Planck's constant
C_l	Velocity of light

Physical variables

ν	Frequency
$\tilde{\nu}$	Wavenumber
A	Absorbance
I	Transmitted intensity
I_0	Incident intensity
ε	Molar absorption coefficient
c	Content
d	Path length
D	Dichroism
r	Chain axis
μ	Transition moment vector
φ	Angle between the X axis and the projection of the chain axis on XY plane
α_T	Angle between the chain axis and the transition moment vector
θ	Angle between the preferred direction (Z axis) and the chain axis
E_{II}	Electric vector parallel to Z axis
$E_{\perp}$	Electric vector parallel to y axis
f	Hermans orientation function
f_F	Fraser's orientation function
ΔH_f	Enthalpy of fusion

ΔH_f^0	Enthalpy of fusion of a sample with 100 % crystallinity
X_c	Crystallinity
L	Thickness of the lamellae
σ_e	Free surface energy of the ends at which chains fold
T_m	Melting temperature of the investigated PP
T_m^0	Equilibrium melting temperature
K_α	Content of α polymorph
K_β	Content of β polymorph
ΔH_α	Enthalpy of fusion of the α-phase
ΔH_β	Enthalpy of fusion of the β-phase
M_n	Number average molar mass
M_w	Weight average molar mass
B	Birefringence
n	Refractive index

1 Summary

Polypropylene (PP) is a highly versatile polyolefin, which is being used in a wide variety of applications. Depending on the final application, the chemical and morphological properties of PP have to be tailored. The current research work was performed with a particular focus towards the morphological changes in PP triggered by welding. Welding is a widely applied method for joining plastics which, however, generates a complex morphological polymer structure at the weld. The effect of processing on the morphology of PP was studied for welds between plates of PP homopolymer (PP-H). Due to the complex interplay of heating and cooling rates as well as the mechanical forces during welding, the PP chains rearrange themselves in different patterns and forms different zones in the weld, which were qualitatively analyzed by polarized light microscopy (PLM). Three distinct zones, which differ in their crystal structure and size, were observed in PLM, namely the injection molded plate with the original morphology, the weld seam and the weld core. The different cooling and heating rates cause the polymer to crystallize at different rates. Quantitative studies on these effects raised upon welding are a prerequisite to modulate the end use properties of a welded PP. Hence, the orientation of polymer chains was quantified by infrared microscopy (μFT-IR) across PP welds. Thus it could be shown that the polymer chains were oriented along machine direction (MD) at the plates and normal direction (ND) at the weld seams.

One of the major applications of PP is the sector of pipes which are being used to transport various kinds of liquid media. Disinfection of water by strong oxidants due to health reasons is a routine process in the current situation. Yet, the transportation of this disinfected water can cause severe damages to PP. A detailed research on the deterioration rates and the mechanisms underlaying when PP is in contact with hot water and chlorinated water with different chlorine concentrations and at different temperatures was carried out. The pipes chosen for the durability studies were a random copolymer of propylene with ethylene (PP-R) nucleated with α- and β-nucleating agents (PP-R1 and PP-R2 respectively).

The pipes were stabilized with 1,3,5-tris (3,5-di-tert-butyl-4-hydroxybenzyl)-2,4,6-methylbenzene (AO-13), Pentaerythritol tetrakis (3-3,5-di-tert-butyl-4-hydroxyphenyl) propionate (AO-18) and the processing stabilizer tris(2,4-di-tert-butylphenyl) phosphite (PS-2). The characteristic ester carbonyl absorption in the infrared

spectrum at 1740 cm^{-1} was used to quantify AO-18. However, the characteristic bands of AO-13 overlapped with the bands of AO-18 and PS-2. To overcome this problem a new method has been developed for μFT-IR to quantify AO-13 from a mixture with AO-18 and PS-2. The quantification results of AOs obtained from μFT-IR were well supported by Extraction→HPLC.

PP is vulnerable to deterioration in the absence of stabilizers. Thus, monitoring the stabilizer loss is an alternative approach to determine the durability of polymers in reactive environments. Degradation/extraction of AOs is highly dependent on the morphology of the material. In that case, the extrusion of polymer melt into the form of hollow cylindrical pipes generates a distinct morphological profile across the pipe wall. Using μFT-IR it could be shown that the polymer chains in PP-R1 were orientated along the extrusion direction due to the fast crystallization of the injected melt triggered by α-nucleation. The diffusion of small molecules through these kinds of oriented networks is faster than randomly oriented ones. In PP-R2, the β-nucleation led to a random orientation of polymer chains at the inner surface which gave impermeability towards the small molecules. This difference in the penetration characteristics of PP-R1 and PP-R2 manifested in different deterioration rates of the pipes. The faster penetration of the media caused the formation of a higher amount of macroradicals in PP-R1. Hence a higher amount of AOs was required to stabilize these macroradicals to prevent the polymer chain scission.

In order to understand the influence of temperature on the degradation of the polymer, ageing was carried out at two temperatures 95 and 110 °C. Out of these experiments, the degradative processes of the polymer, namely the loss of antioxidants and reduction in molar mass of the polymer, proceeded more rapidly at 110 °C. Experiments with different chlorine concentrations showed that deterioration was more pronounced at higher chlorine concentrations. The depletion of the two AOs, AO-18 and AO-13, differs in their rates. In detail it was found that AO-18 is lost faster to the inner medium than AO-13, irrespective of ageing condition and temperature. The degradation of AO-18 can be caused via two mechanisms: The hydrolysis of the ester bond and via the intended donation of phenolic hydrogen to the macroradicals. On the contrary AO-13 is susceptible towards degradation solely by the quenching of macroradicals. Therefore, an accelerated degradation of AO-18 was observed irrespective of the ageing temperature.

2 Zusammenfassung

Polypropylen (PP) ist ein sehr vielseitiges Polyolefin, welches in einer großen Vielzahl von Anwendungen zum Einsatz kommt. Die chemischen und morphologischen Eigenschaften von PP müssen entsprechend der Endanwendung maßgeschneidert werden. In der vorliegenden Arbeit wurde ein Schwerpunkt bei den durch Schweißen ausgelösten morphologischen Veränderungen von PP gesetzt. Schweißen ist eine sehr weit verbreitete Methode des Fügens von Kunststoffen, bei der eine komplexe morphologische Struktur in der Schweißnaht erzeugt wird. Der Effekt des Schweißens auf die Morphologie des PP wurde für Schweißnähte zwischen zwei geschweißten Platten aus PP-Homopolymer (PP-H) untersucht. Bedingt durch das komplexe Zusammenspiel von Heiz- und Kühlraten und die mechanischen Kräfte ordnen sich die PP-Ketten in unterschiedlichen Strukturen und bilden unterscheidbare Zonen in der Schweißnaht, die in qualitativer Art und Weise mittels Polarisationsmikroskopie (PLM) untersucht wurden. Drei Zonen, die sich in der Art und Ausdehnung ihrer Kristalle unterscheiden (die spritzgegossene Platte mit der Originalmorphologie, die Schweißfuge und der Kern der Schweißnaht) wurden mittels PLM beobachtet. Die unterschiedlichen Kühl- und Heizraten bedingen unterschiedliche Kristallisationsgeschwindigkeiten des Polymeren. Quantitative Untersuchungen dieser Auswirkungen des Schweißens sind die Vorbedingung, um die Eigenschaften von geschweißtem PP maßzuschneidern. Dies war die Motivation, die Orientierung der Polymerketten in der Schweißnaht mittels Infrarotmikroskopie (μ-FTIR) zu untersuchen. So konnte gezeigt werden, dass die Polymerketten in der Nähe der Platten entlang der machine direction (MD) un in der Schweißnaht in normal direction (ND) ausgerichtet sind.

Eine bedeutende Anwendung von PP ist der Sektor von Rohren zum Transport einer Vielzahl flüssiger Medien. Die Desinfektion von Wasser durch starke Oxidantien mit dem Ziel der Gesundheit ist heutzutage Routine. Dennoch kann der Transport derartig desinfizierten Wassers zu schweren Schäden am PP führen. Eine detaillierte Studie zu den Schädigungsraten und den der Schädigung von PP im Kontakt mit heißem und chloriertem Wasser zugrunde liegenden Mechanismen wurde durchgeführt. Für diesen Zweck wurden Rohre aus einen statistischen Copolymer aus Propylen und Ethylen (PP-R), nukleiert mit α- und ß-Nukleierungsmitteln (PP-R1 bzw. PP-R2), ausgewählt.

Die Rohre waren mit 1,3,5-Trimethyl-2,4,6-tris-(3,5–di-tert-butyl-4-hydroxybenzyl)-benzol (AO-13), Pentaerythritol tetrakis (3-3,5-ditert-butyl-4-hydroxyphenyl) propionat (AO-18) und dem Verarbeitungsstabilisator tris(2,4-ditert-butylphenyl)phosphit (PS-2) stabilisiert. Die charakteristische Absorption der Estercarbonylbande im Infrarotspektrum bei 1740 cm^{-1} wurde zur Quantifizierung von AO-18 herangezogen. Dennoch überlappten die charakteristischen Banden des AO-13 mit denen des AO-18 und PS-2. Um dieses Problem zur lösen, wurde eine Methode für μ-FTIR entwickelt, um AO-13 in Mischungen mit AO-18 und PS-2 zu quantifizieren. Die Ergebnisse der Quantifizierung der AOs mit dieser Methode sind in guter Übereinstimmung mit denen der Extraktion→HPLC.

PP ist in der Abwesenheit von Stabilisatoren anfällig für Abbau. Daher ist die Verfolgung des Stabilisatorverlustes eine Alternative zur Abschätzung der Dauerhaftigkeit von Polymeren in aggressiven Umgebungen. Der Abbau und die Extraktion von AOs hängen stark von der Morphologie des Materials ab. Die Extrusion der Polymerschmelze in die Form hohlzylidrischer Rohre generiert ein ausgeprägtes Morphologieprofil über die Rohrwandung. Mittels μ-FTIR konnte gezeigt werden, dass die Polymerketten in PP-R1, bedingt durch die schnelle Kristallisation der Schmelze aufgrund der α-Nukleierung, entlang der Extrusionsrichtung ausgerichtet waren. Die Diffusion durch diese Art des Netzwerkes verläuft rascher als durch ein solches mit statistischer Kettenausrichtung. Die ß-Nukleierung in PP-R2 führte zu einer zufälligen Ausrichtung der Ketten an der inneren Rohroberfläche. Die Unterschiede in den Durchlässigkeiten von PP-R1 und PP-R2 manifestierten sich in unterschiedlichen Abbauraten der Rohre. Das schnellere Eindringen von Medien in PP-R1 führte zu einer vermehrten Bildung von Macroradikalen. Aus diesem Grunde war eine erhöhte Menge an AOs erforderlich, um eine Spaltung der Polymerketten durch diese Macroradikale zu verhindern.

Um den Einfluss der Temperatur abzuschätzen, wurde die Alterung der Rohre bei 95 und 110 °C durchgeführt. Die Untersuchungen zeigten, dass der Verlust von Antioxidantien und die Reduktion des Molekulargewichtes des Polymeren bei 110 °C beschleunigt abliefen. Versuche mit unterschiedlichen Chlorkonzentrationen zeigten, dass der Abbau bei 110 °C verstärkt auftritt. Die Antioxidantien AO-13 und AO-18 weisen unterschiedliche Verlustraten auf. Konkret wurde gefunden, dass AO-18, unabhängig von Alterungsbedingungen und Temperatur, schneller an das Innenmedium abgegeben wird. Der Abbau von AO-18 kann durch zwei Mechanismen verursacht werden: Hydrolyse der Estergruppe oder durch Abgabe

des phenolischen Wasserstoffs an das Macroradikal. Demgegebüber verläuft der Abbau von AO-13 lediglich durch Quenchen der Macroradikale. Aus diesem Grunde wurde ein beschleunigter Abbau von AO-18, unabhängig von der Testtemperatur, beobachtet.

3 Introduction

Within the broad division of synthetic polymers, polyolefins are of immense economic importance, and, due to their extremely flexible and adaptable application properties, find use in many application areas like packaging, construction industries, electrical, electronics, transportation, telecommunication, aerospace, biomedical applications, households etc. [1, 2]. Polyethylene (PE) and polypropylene (PP) are the two important polyolefins widely available in the market. As a result of their diverse applications, paired with the economic significance, polyolefins have been subjected to detailed research, comprising methodologies to tailor the end use properties and elucidate problems associated with their applications.

Polyolefins, like other polymers, are often in contact with different environments during their application, which may severely affect the lifetime of final products made from these materials [3, 4]. These effects in general can be regarded as degradation, in which the physical and chemical properties of the polymer change. The factors that adversely affect the properties of the material can be temperature, light, air, mechanical forces and chemicals.

3.1 Polypropylene

PP is a highly versatile semicrystalline thermoplastic, which is being used for both short term and long term (durable) applications [5]. The application properties of PP are mainly governed by its molecular metrics. Among these the microstructure of PP is an important determinant for many macroscopic properties like mechanical strength, stiffness, elongation. [6]. PP exhibits exceptional mechanical and chemical properties, such as high stiffness and resistance towards stress crack propagation. According to the chemical composition, PP is in the commercial parlance classified into the homopolymer (PP-H) and a copolymer (PP-R), which is a copolymer of propylene with small amounts of ethylene. PP is made by transition metal catalyzed polymerization of propylene [7]. Depending on the orientation of the pendant methyl group in the chain, the isotactic (iPP), syndiotactic (sPP), and atactic (aPP) variant can be distinguished (Figure 1).

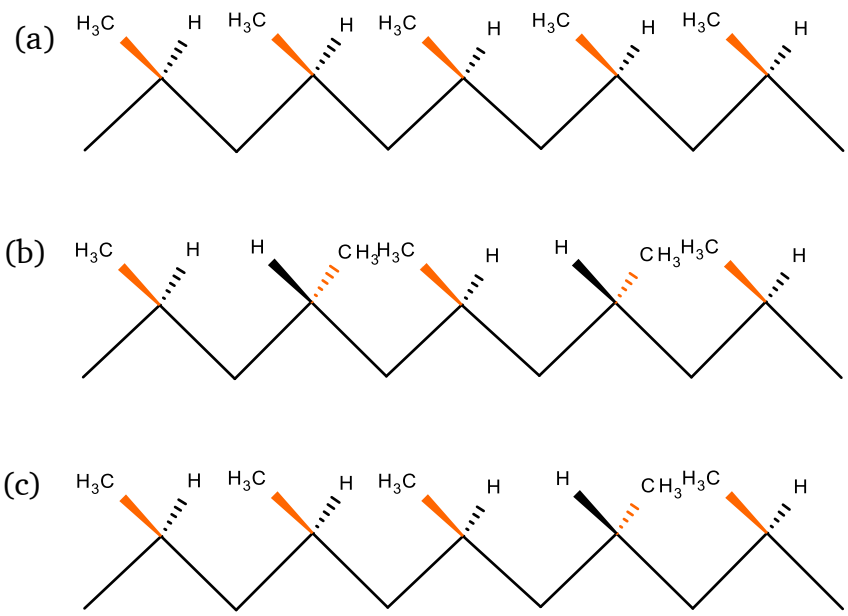

Figure 1: (a) iPP (b) sPP (c) aPP.

In iPP (Figure 1.2) the pendant methyl groups are all on the same side of the polymer chain, while in sPP the neighboring methyl groups point opposite to each other. In aPP, the pendant methyl groups display a random orientation with respect to the polymer backbone. Due to this regular arrangement, iPP and sPP are characterized by a high degree of crystallinity, while aPP is an amorphous material.

Statistic copolymers of propylene (PP-R) are formed by adding ethylene or, less commonly, 1-butene or 1-hexene (~ 1.5 – 6 wt. %) as comonomer, which will be incorporated randomly among the propylene units. The incorporation of comonomer units reduces the degree of crystallinity (X_c) and thereby increases the impact strength [8].

Morphology of PP

During crystallization the PP macromolecules arrange into a three fold helix, which may be right (R) or left (L) handed [9], with the methyl groups pointing either up or down [10] (Figure 2).

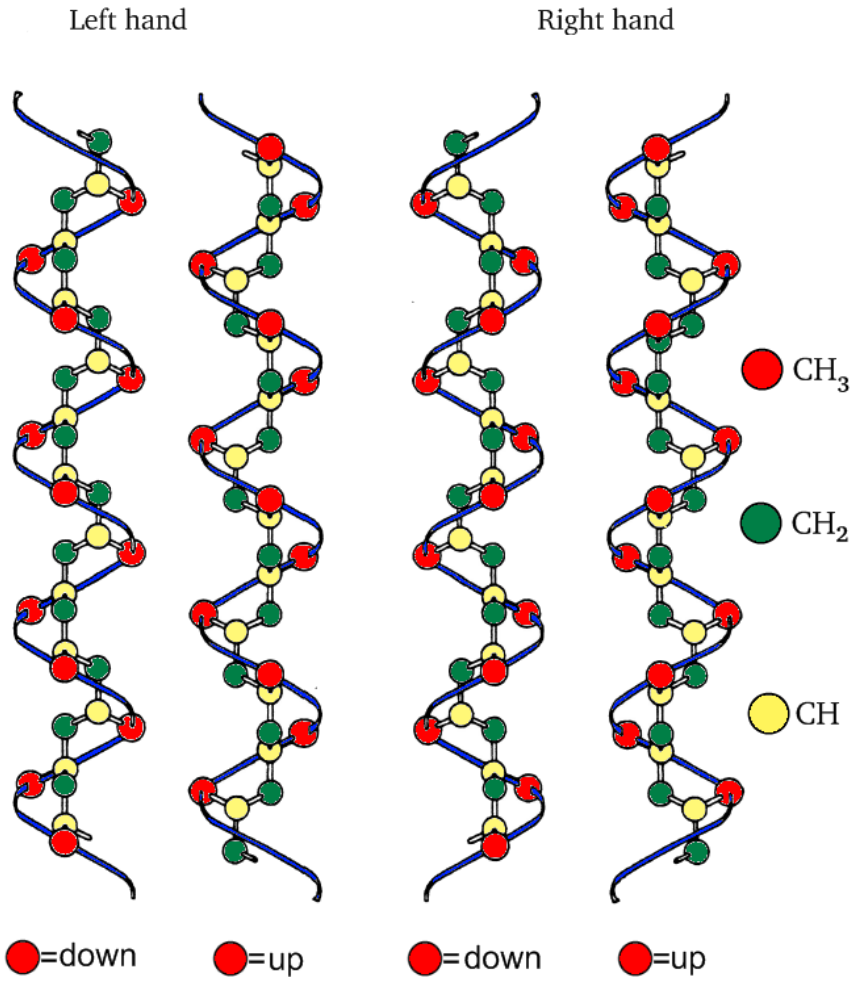

Figure 2: Helical structure of PP.

The helical strands arrange back and forth to lamellae, which grow radially and tangentially from the nucleation centers, thus forming spherulites. Non crystallized polymer chains, so called tie molecules, connect the lamellae.

Based on the crystallographic structure, three polymorphs of PP, referred to as alpha (α), beta (β) and gamma (γ) modification, can be distinguished. Adding nucleating agents is a popular method to favor the formation of a desired polymorph. The mechanical properties of PP depend on the polymorphic composition [11, 12], and an enriched percentage of β-phase leads to higher tensile elongation and improved impact resistance [13]. The extended mechanical properties of the β-phase have been explained with respect to the spherulite structures [14].

Alpha form

In the α-form the carbon atoms of the helically coiled PP chains occupy a monoclinic unit cell [15]. Lamellae growth in this polymorph is generally dominant in the radial direction. However, the radial lamellae undergo branching as cross hatching which is a characteristic of the α-form, and the branches formed on the lamellae are regarded as quadrites [16]. The crystallite axis/chain axis (c-axis) of the polymer chain is perpendicular to the plane of the radially grown lamellae [17]. The spherulite structure of the non-nucleated and α-nucleated PP is shown in Figure 3.

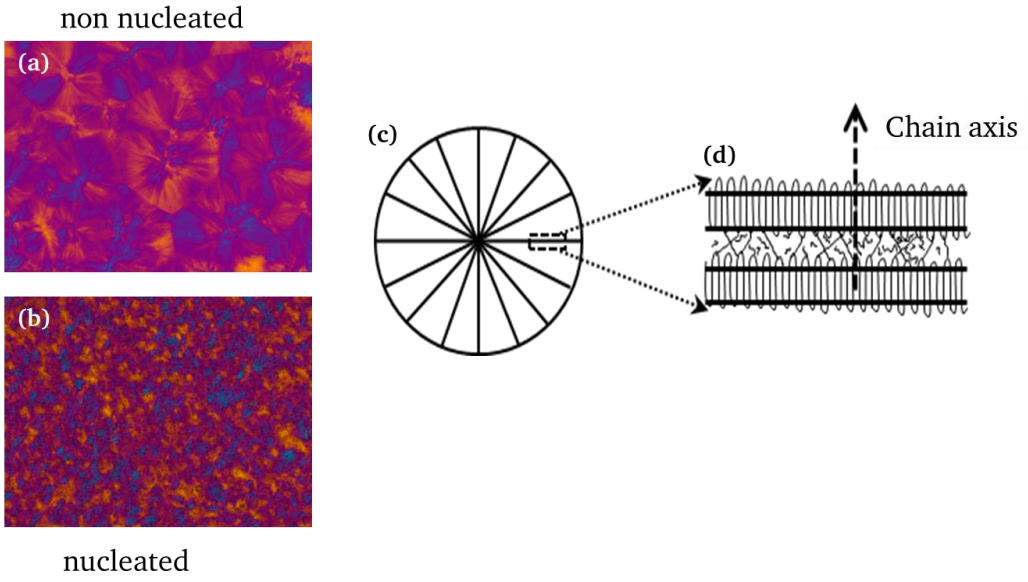

Figure 3: Spherulite structure of the α-form of PP. (a) Non nucleated, (b) nucleated, (c) schematic representation of spherulite and (d) arrangement of polymer chains in lamellae and the direction of chain axis.

The α-crystals of PP are positively birefringent under polarized light, and this form is considered as the thermodynamically stable one [18-20].

Beta form

The β-form of PP crystallizes in a hexagonal crystal lattice. The lamellae are stacked radially from a nucleation point without cross hatching. The spherulitic structure of the β-form is known as sheaf like spherulitic structure. Thermodynamically, the β-form is the least stable one and its melting point is 12-15 °C lower than that of the α-form. The β-crystals in PP exhibit excellent toughness and durability, followed by the α- and γ-form [21-24]. The β-spherulites are negatively birefringent under polarized

light [25-27]. The spherulite structure of the non-nucleated and β-nucleated PP is shown in Figure 4.

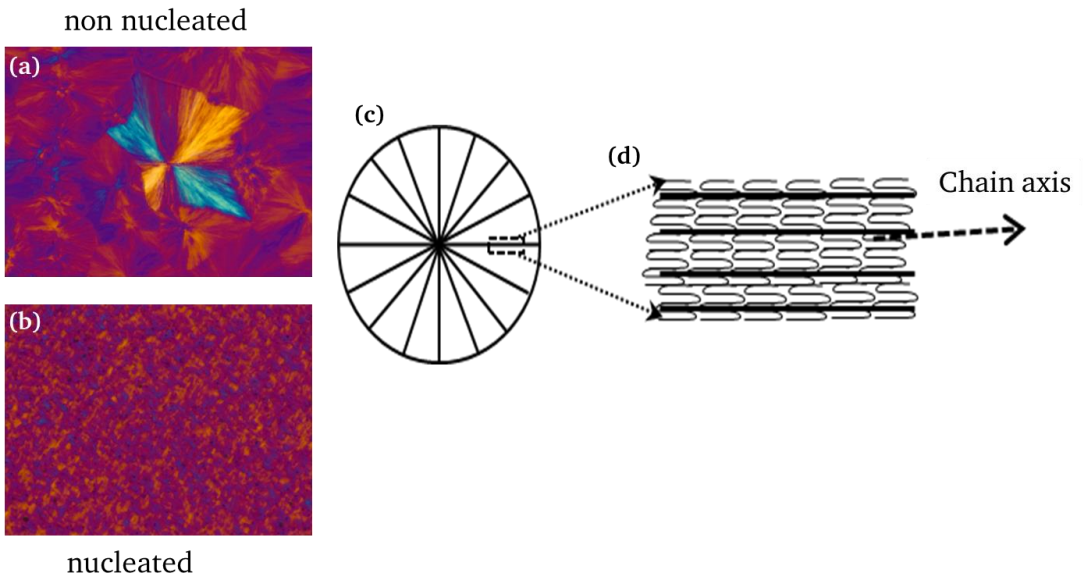

Figure 4: Spherulite structure of the β-polymorph. (a) Non nucleated, (b) nucleated, (c) schematic representation of a spherulite and (d) arrangement of polymer chains in lamellae and the direction of chain axis.

Gamma form

The γ-form crystallizes in an orthorhombic unit cell [28], which is usually associated with the α-form. The formation of the γ-phase is favored by low molar mass or crystallization at elevated pressure [28, 29].

3.2 Applications of polypropylene

PP is confectioned to films, non wovens, fabrics, and a wide range of semi-finished articles. The major sectors utilizing PP are automotive, construction, packaging and textiles [30] (Figure 5).

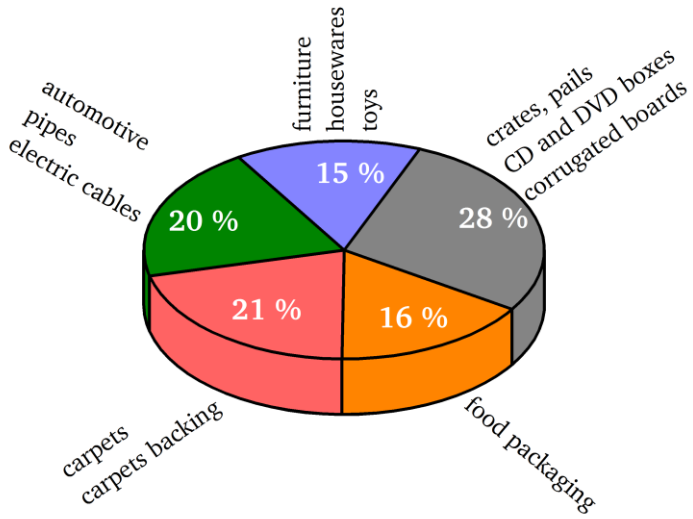

Figure 5: Use of PP in various industries.

In the automotive sector, the widely tunable haptics make PP the preferred material for many interior applications (e.g. dashboards), while the mechanical properties have been exploited in exterior applications (e.g. bumpers). Building and construction industries account for a major percentage of the PP consumption, which includes insulation of power cables and pipes.

PP pipes

Pipes made of PP play a major role in the transportation of liquid media, where, due to their excellent property profile, they continue to replace metallic ones [31]. Comparatively high temperature resistance, low density and heat conductivity are characteristics, which make PP the preferred material for plumbing components. Ease of installation, long term resistance towards internal pressure and a wide range of chemicals, in combination with easy weldability make PP attractive for pipe applications.

PP weld seams

Welding is a widely used technique for joining plastic parts without the addition of any foreign material which is an inevitable step in the processing of some of the polyolefin based products. However, welds are always a weak point with respect to mechanical properties. During welding, the joint surfaces undergo melting followed by solidification. Different welding techniques like butt welding, IR welding, hot gas welding etc. have been used to join plastics. Butt welding is a highly versatile variant of welding [32], which has been regularly applied to join injection molded semi-

finished products and pipes for installations. During injection molding, pre-orientation of the polymer chains along the extrusion direction was induced in the semi-finished parts. These are then brought into contact with a heated metallic plate until the polymer melts. The melted surfaces are compressed with a constant pressure until the melt solidifies. An image showing injection molded plates and the weld joining these is presented in Figure 6.

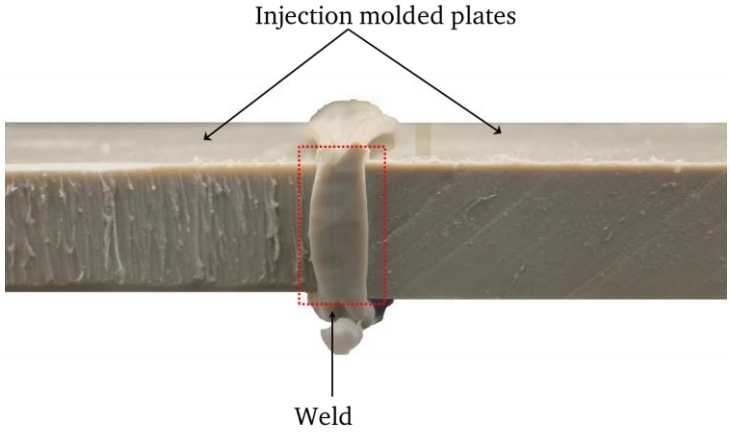

Figure 6: Welded sample showing the injection molded plates and the weld.

3.3 Degradation of polypropylene

PP is susceptible to degradation during processing and end use. During processing, PP is in contact with air at elevated temperature, which may trigger thermo-oxidative degradation. In the same sense, contact with air during long term application may lead to degradation. The degradation pathway of PP has been classified into primary and secondary reactions [33], where the latter are initiated from the primary reaction products. Primary degradation of PP proceeds via initiation, progression and termination. In the following, a brief overview on the various steps of PP degradation is given.

Primary Reactions

In the initiation step a hydrogen radical is abstracted from the chain, preferentially at the tertiary carbon atom (eq. 1).

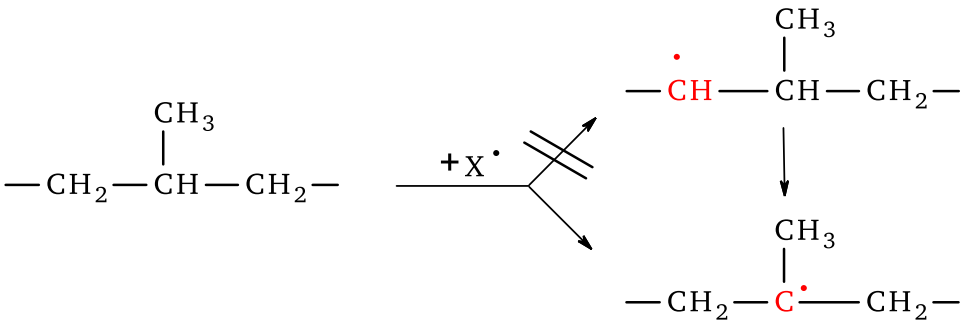

1

$X^{\bullet}$ = radical

The macroradical thus formed reacts in the propagation step with oxygen (eq. 2).

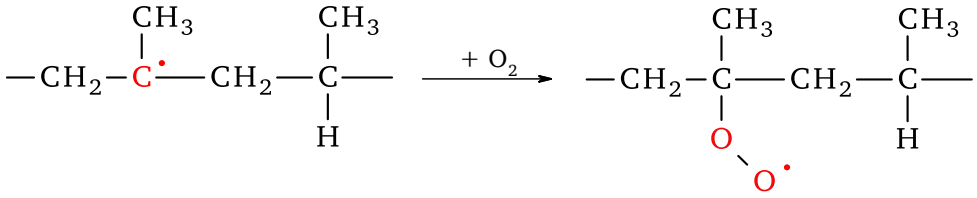

2

The peroxy radicals can undergo homolytic scission, leading to the formation of aldehydes and ketones, depending on the initial position of the radical (eq. 3 and 4).

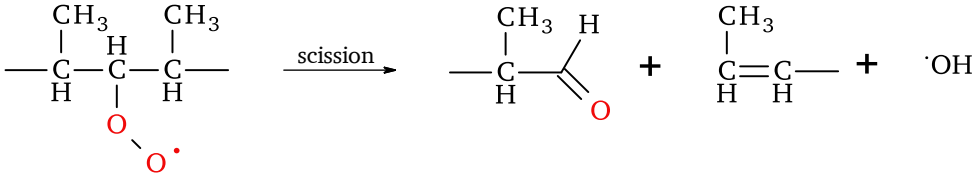

3

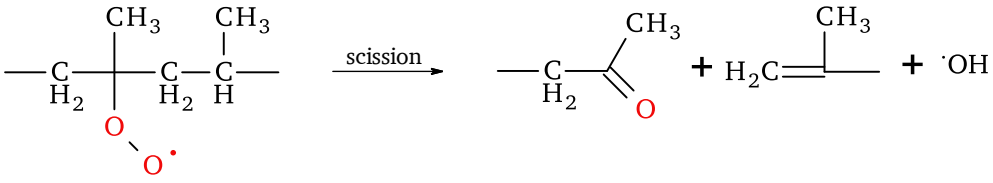

4

The reaction can also be terminated by disproportionation of alkyl radicals, which under oxygen deficient conditions leads to the formation of vinyl groups.

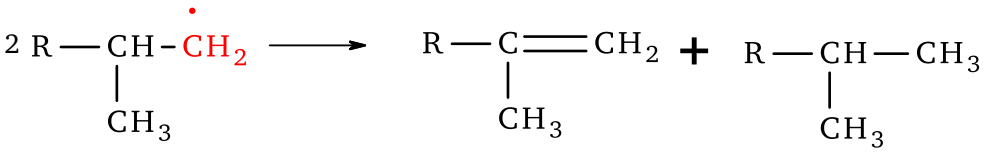

5

R = polymer

The primary degradation products (aldehydes and ketones) can undergo further reactions leading to the formation of peracids, carboxylic acids, esters and lactones [33].

3.4 Interaction of chlorine with polypropylene pipes

Disinfectants are widely used in water treatment. Depending on the final application of the transported water, various disinfection methods have been used, which can be classified as physical (UV radiation, solar disinfection, thermal etc.) and chemical (chlorine, chlorine dioxide, ozone etc.) [34]. Chlorine is a known disinfectant, widely used to treat both drinking water and waste water due to its strong oxidizing effect, widespread availability, and storability [35]. However, it has been widely evident that chlorinated water has the potential to initiate the degradation of polyolefins [36].

The oxidizing potential of chlorine in aqueous solution depends on the temperature and the pH value. The effect of chlorinated water on plastic pipes can either be physicochemical in nature, such as extraction of additives, or chemical by degrading the stabilizers and oxidizing the polymer. The oxidative action of chlorine is based on the formation of hypochloric acid (HOCl), which has a strong tendency to release oxygen. Chlorine gas dissolves in water and disproportionates according to eq. 6, and the resultant HOCl then dissociates according to eq. 7 [37].

$$Cl_2 + H_2O \Leftrightarrow HOCl + Cl^- + H^+ \quad (6)$$

$$HOCl \Leftrightarrow ClO^- + H^+ \quad (7)$$

At a pH of 6.8, both HOCl (95 %) and Cl_2 (5 %) are present in the water. It has been suggested that the chemical consumption reaching far from the surface of the pipe can be caused by Cl_2. Cl_2 can dissociate into chlorine radicals, which react with the chlorine ions and form a dichloride radical ($Cl_2^{-\bullet}$) [38].

$$Cl^\bullet + Cl^- \rightarrow Cl_2^{-\bullet} \quad (8)$$

$Cl_2^{-\bullet}$ is a strong one electron oxidant, which reacts with hydrocarbons [39, 40] as well as it can even dissociate water molecules leading to the formation of hydroxyl radicals.

$$Cl_2^{-\bullet} + H_2O \rightarrow {}^{\bullet}OH + H^+ + 2Cl^- \qquad 9$$

The degradation of AOs by HOCl and its dissociation products has been analyzed [41, 42]. Additionally, HOCl and its dissociation products in water are capable of inducing the degradation of the polymer by abstracting a proton from the tertiary carbon or by triggering oxidative degradation.

In summa, the deterioration of pipes due to contact with ageing media proceeds through the following steps (Figure 7).

- Loss of AOs by physical extraction and chemical consumption
- Oxidation of the polymer at the inner wall surface
- Formation of micro-cracks in the degraded area
- Increase in crack density and crack length
- Failure once a crack has reached the outer wall.

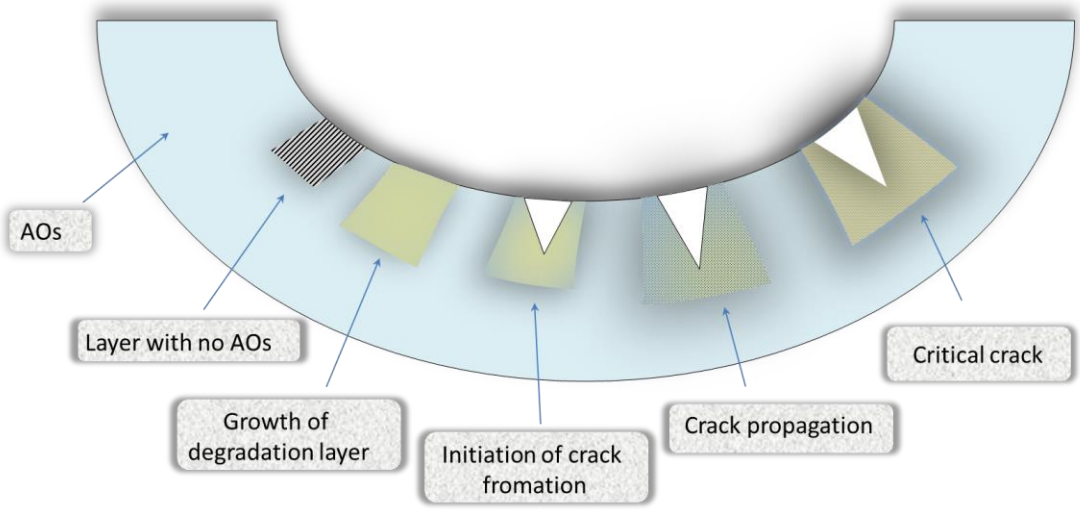

Figure 7: Schematic representation of the degradation of the inner surface of a pipe exposed to aggressive environments [43].

3.5 Stabilization

As a result on the macroscopic level, the oxidation of the polymer leads to a loss of the mechanical stability. To prevent this, PP and compounds of PP have to be stabilized

against thermo-oxidative degradation. For this purpose, hindered phenolic AOs are widely used as long term stabilizers (primary AOs), and regularly combined with organic phosphites (secondary AOs), which act as processing stabilizers [44].

Primary antioxidants

As discussed in 3.3, the degradation of PP is initiated by hydrogen abstraction from the chain, which leads to the formation of macroradicals (poly alkoxy and peroxy radicals). Primary AOs react with these macroradicals by donating a hydrogen atom, thereby quenching the macroradical and preventing the propagation eq. 10-11.

$$PPO^{\bullet} + AO-H \rightarrow PPOH + AO^{\bullet} \quad (10)$$

$$PPOO^{\bullet} + AO-H \rightarrow PPOOH + AO^{\bullet} \quad (11)$$

Sterically hindered phenols are widely used as primary AO, with AO-18 and AO-13 being the representatives dominating the market. Their structures are shown in Figure 8.

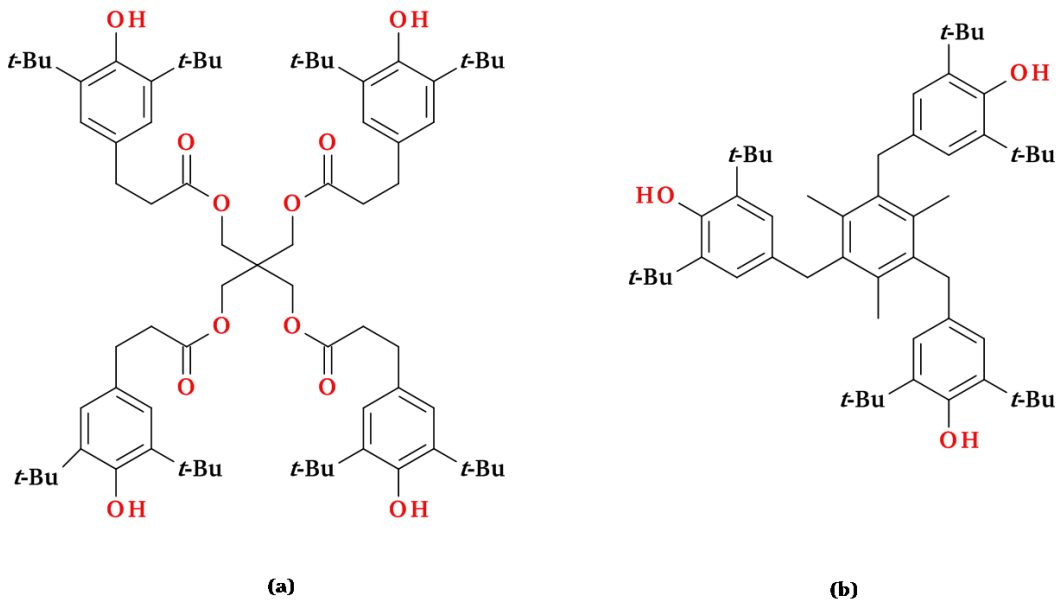

Figure 8: Structure of a) AO-18 and b) AO-13.

Secondary Antioxidants

Secondary AOs (processing stabilizers) are added to protect the polymer during processing by decomposing the initially formed hydroperoxides. Sterically hindered phosphites have been most commonly used for this purpose (Figure 9).

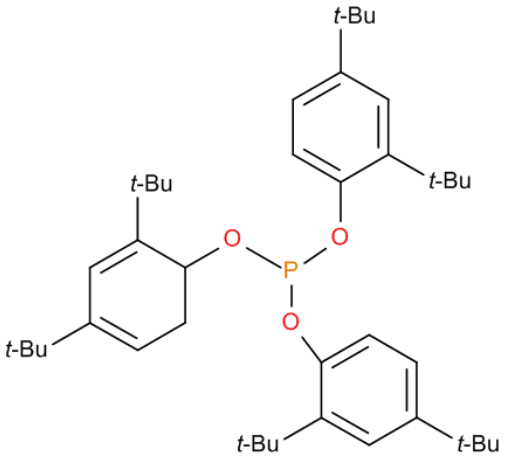

Figure 9: Structure of PS-2.

The reaction of a phosphitic stabilizer with hydroperoxides is shown in eq. 12.

$$P(OR)_3 + ROOH \rightarrow PO(OR)3 + ROH \qquad 12$$

The degradation cycle and the interception points of AOs are presented in Figure 10.

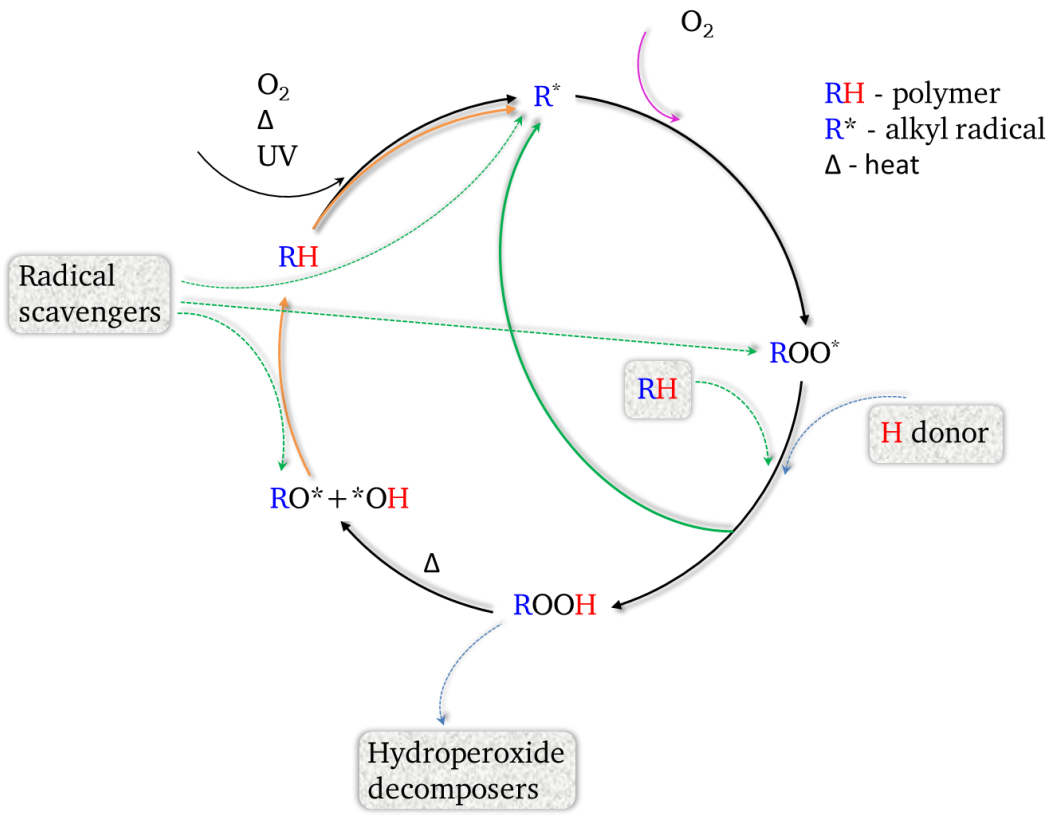

Figure 10: Degradation and stabilization cycle of polyolefins [45].

C- and O-centered macroradicals are generated along the polymer chain as a result of contact with oxygen. At this stage, primary AO (i.e., radical scavengers) donate hydrogen radicals, thus trapping the macroradicals from further reactions. In the absence of radical scavengers the macro-radical can form peroxy radicals, which can also be deactivated by abstracting a proton from the radical scavenger. In a second pathway, peroxy radicals react with the polymer chain itself, leading to the formation of hydroperoxides. These can be deactivated by hydroperoxide decomposers. The hydroperoxides can be converted to alkoxy and hydroxyl radicals upon heating, which themselves can also be deactivated by radical scavengers.

3.6 Goals of the study

The thesis focuses on two aspects, namely the quantitative analysis of processing (welding) on the morphology of PP-H and the influence of deteriorating environments, particularly chlorinated water and hot water, on PP-R pipes.

Processing techniques that are commonly used for polyolefins are known to generate a typical morphology in the product, which is a crucial parameter determining the mechanical properties of the material. In this work a new methodology to quantify

weld morphology has been introduced. It is well known that weld seams are characterized by a complex morphology, yet, quantitative data, which are essential to relate the welding parameters and the morphology thus formed are not available. Due to the interplay between heating and cooling rates and shear forces polymer chains at the welds will crystallize under highly variable conditions. A strong focus shall be set on developing μFT-IR for quantitative analysis of the morphology in welds, aiming at determining the orientation of polymer chains and the degree of crystallinity.

The second part of the thesis dedicates to the analysis of changes occurring in the wall of PP-R pipes when exposed to chlorinated and hot water at conditions reflecting the end use application. The main goals on this part are to determine the chemical changes occurring to the polymer itself and the AOs. Namely, experimental protocols shall be developed for μFT-IR to study the chemical consumption/physical extraction of AOs and the oxidation of the polymer. From the experimental data the kinetics of the physical loss via extraction and chemical oxidation of the AO shall be determined, and related to the conditions of testing. This requires to establish methods which can quantitatively determine an individual antioxidant in mixtures. The results from μFT-IR shall be confirmed by the classical approach of mechanically abrasing layers and analyzing their AO-content via measuring the oxidative induction time and Extraction →HPLC.

4 Permissions and rights from publishers

Figure 24, Figure 26, Figure 27, Figure 28, Figure 29, Figure 30, Figure 31, Figure 32, Figure 33, Figure 34, Figure 35 and Figure 36.

Figure 41, Figure 42, Figure 43, Figure 44, Figure 49, Figure 51 a and b, Figure 52, Figure 53, Figure 54 a and b, Figure 56, Figure 58, Figure 59, Figure 61, Figure 62, Figure 65 a, Figure 66, Figure 67, Figure 81, Figure 85, Table 8 and Table 10.

Figure 14 b

5 Theoretical Background

A variety of analytical techniques has been used to achieve the goals of this study. In order to understand the findings obtained and their interpretations the theoretical background of the applied methods shall be given in the following.

5.1 Polarized light microscopy

Polarized light microscopy (PLM) has been widely applied for investigating the morphology of semicrystalline polymers, where it has been used to determine the supramolecular structure with regard to spherulite size distribution and polymorph identification. In a polarized light microscope two polarization filters are orthogonally aligned to each other, thus letting no light pass through. By placing a birefringent sample between the two filters, the plane of vibration of the refracted light changes according to the structure of the material and a portion passes through the second filter (Figure 11).

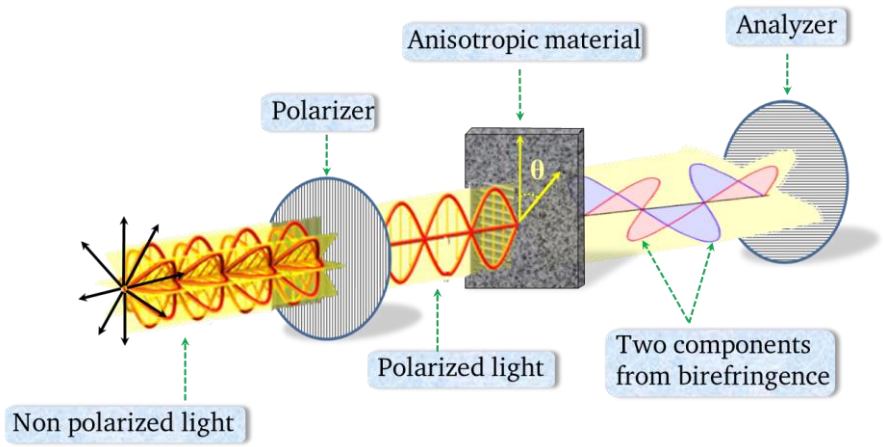

Figure 11: Schematic representation of the theory of PLM.

Birefringence (B) is a measure for the difference between the highest (n_e) and lowest (n_o) refractive index of an anisotropic crystal (eq. 13).

$$B = n_e - n_o \qquad 13$$

Based on the optical properties, anisotropy of a crystal system can be divided into uniaxial, with a single optical axis, and biaxial, with two optical axes. When non-polarized light passes through a birefringent material the beam is split into an ordinary and an extra ordinary ray (Figure 12).

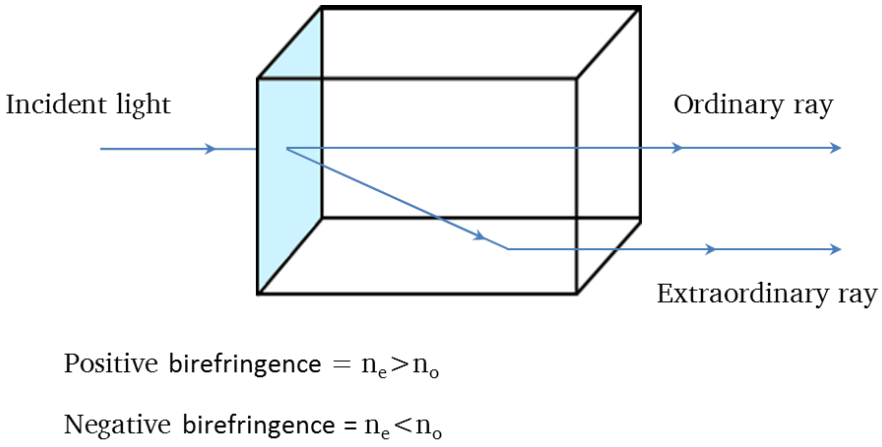

Figure 12: Schematic representation showing the birefringence.

An anisotropic material is referred to as positively birefringent when the refractive index experienced by the extra ordinary ray (n_e) is higher than that of the ordinary ray (n_o) and the vice versa is referred to as negatively birefringent.

5.2 Infrared spectroscopy

A molecule absorbs infrared radiation when its dipole moment changes. A variation in the dipole moment of a molecule can occur due to molecular motions, such as vibration and rotation. The change in dipole moment associated with these molecular motions creates an electric field. The absorption of IR radiation causes transitions between rotational and vibrational energy levels, and the difference in energy between the ground (E_0) and the excited (E_1) level is proportional to the frequency (ν) of the incident radiation (eq. 14).

$$\Delta E = E_1 - E_0 = h\nu \qquad 14$$

where h is Planck's constant. The frequency of IR absorption is directly proportional to the wavenumber, which is the number of waves per unit length.

$$\tilde{\nu} = \frac{\nu}{c_1} \qquad 15$$

where c_l is the velocity of light. A vibrating molecule absorbs an energy corresponding to ΔE, which is typically presented in the form of a spectrum with the wavenumber on the x-axis and the intensity of the absorption in the y-axis.

5.2.1 Quantification

For a quantitative analysis the experiment has to be carried out in transmission mode so that the incident beam passes through the sample. The initial intensity (I_0) of the beam and its intensity after passing the sample (I) are related to the absorbance (A) of the sample according to eq. 16.

$$A = -\ln \frac{I}{I_0} = \varepsilon \cdot c \cdot d \qquad 16$$

ε is the molar absorption coefficient, d the path length, and c is the content of the absorbing moiety.

A is a measure for the loss of energy from the incident radiation by the absorbing moiety. Samples are often reshaped to a defined geometry in order to keep d constant. Since ε and d are constants, A is directly proportional to c and thus can be used to quantify a specific moiety. For this purpose an absorption band specific for the component to be quantified should be identified. However, ε has to be determined by calibrating the absorbing moiety in the polymer matrix.

5.2.2 Orientation

Most of the techniques used for processing semicrystalline polymers induce an orientation of the macromolecules in the product. Consequently, a quantitative determination of the orientation has to be carried out to establish the correlation between the processing conditions and the macroscopic properties e.g., mechanics.

IR spectroscopy has been widely used to determine the extent of orientation in semicrystalline polymers. The basic model to calculate the orientation of polymer chains was developed by Fraser and Beer [46-48]. Fraser's model relies on the principle of dichroism (D), where D is defined as the ratio of the absorbance of a vibration when the electric vector of the incident linear polarized light is parallel (A_{II}) to the one with perpendicular direction ($A_{\perp}$) (Eq. 17).

$$D = \frac{A_{II}}{A_{\perp}} \qquad 17$$

The geometric parameters and the coordinate system used to calculate the average orientation of the chain axis are presented in Figure 13.

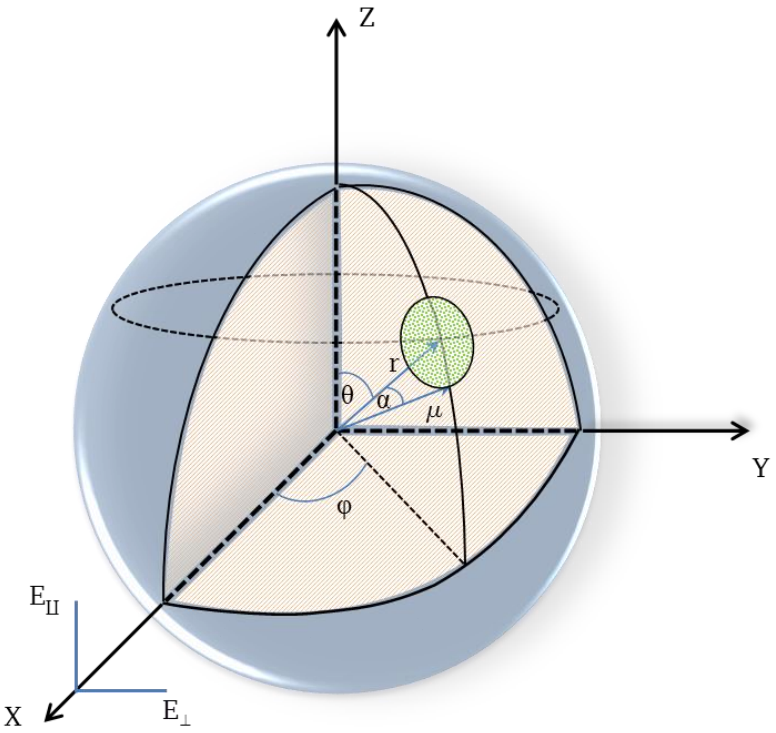

Figure 13: Schematic representation of geometric parameters [49].

The geometrical parameters in Figure 13 are

r = chain axis

μ = transition moment vector

φ = angle between the X axis and the projection of the chain axis on the XY plane

α_T = angle between the chain axis and the transition moment vector

θ = angle between the preferred direction (Z axis) and the chain axis

E_{II} = electric vector parallel to Z axis

$E_{\perp}$ = electric vector parallel to Y axis

Fraser's orientation function (f_F) is expressed as

$$f_F = \frac{D-1}{D+2} * \frac{D_0+2}{D_0-1} \qquad 18$$

where D is the ratio of the absorption coefficients (A_{II}) and ($A_{\perp}$). D_0 is related to α_T by eq. 19.

$$D_0 = 2 * \cot^2 \alpha_T \qquad 19$$

This approach can only be used if the chain orientation is symmetric with respect to the Z axis. As a result, the parallel and perpendicular directions of the sample have to be defined. However, most of the processing techniques induce an orientation of the polymer chains in semi-finished products, which is not known. To solve this, an extended Fraser's model, that permits the calculation of f with respect to the three coordinates, was introduced [49]. In this, the absorbance of linear polarized light along the three perpendicular axes of the sample is measured. Thus, f_F along the Z axis can be calculated according to eq. 20.

$$f_F = \frac{3 * \frac{A_z}{A_x + A_y + A_z} - 1}{2} * \frac{D_0+2}{D_0-1} \qquad 20$$

with A_x, A_y and A_z being the absorbances along the X, Y and Z axis, respectively.

To obtain the complete information about the average chain orientation in the three dimensions, the functions f_x and f_y have to be calculated by exchanging the numerator term "A_z" in eq. 20 to A_x and A_y respectively. The angle θ for the Z axis is calculated by equating the extended f_F with f as follows;

$$\frac{3 * \frac{A_z}{A_x + A_y + A_z} - 1}{2} * \frac{D_0+2}{D_0-1} = f_z = \frac{3 * \langle \cos^2 \theta_z \rangle - 1}{2} \qquad 21$$

To determine the values along the three directions, two microtome sections prepared orthogonally to each other are required, where the first of these can be chosen arbitrarily and the second one has to be prepared perpendicular to that (Figure 14). The three directions along the X, Y and Z axis are commonly designated as MD for machine direction, ND for normal direction and TD for transverse direction (Figure 14).

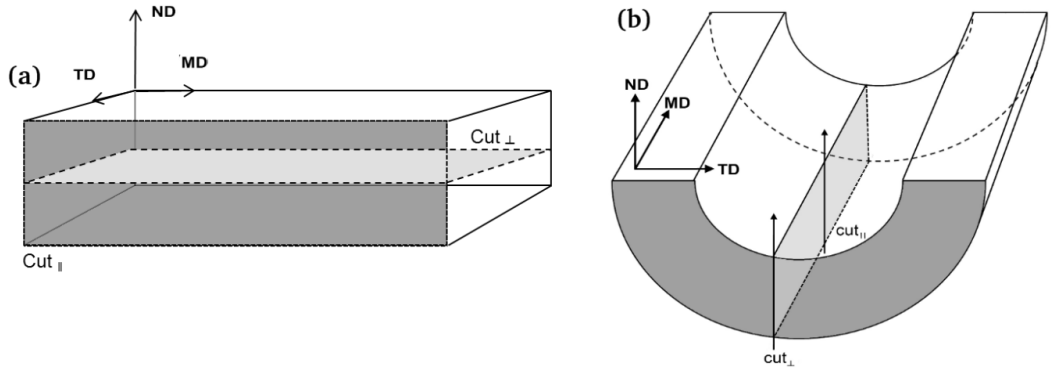

Figure 14: Schematic representation of the microtome cuts and the direction (a) injection molded plate (b) extruded pipe [50].

From Figure 14 a the first microtome cut is in the MD-ND plane and the second cut in the MD-TD plane. In the case of pipes the first cut is prepared along ND-TD i.e., perpendicular to the direction of extrusion, and the second cut along MD-ND.

5.2.3 Determination of the crystallinity of PP

IR-spectroscopy has been widely used to determine the X_c of PP [50]. The bands at 841 cm^{-1} (absorption from the crystalline phase) and 974 cm^{-1} (absorption from both crystalline and amorphous phase) have been used for this purpose. The absorbance of these bands from three mutually perpendicular directions (MD, ND and TD) is averaged since these bands are sensitive to dichroism. Consequently, A_0^{841} and A_0^{973} are the sum of the absorbances along MD, ND and TD (see axis settings in Figure 14) of the bands at 841 and 974 cm^{-1}, respectively. X_c can be calculated using eq. 22.

$$X_c^{IR} = \frac{\alpha_{974}}{\alpha_{841}} \cdot \frac{A_0^{841}}{A_0^{974}} \cdot 100 \qquad 22$$

where α_{974} and α_{841} are the absorption coefficients of the respective bands, and the ratio between these was reported to be 0.79 [51] in the case of PP.

5.3 Differential scanning calorimetry

Differential scanning calorimetry (DSC) is a popular analytical technique to measure the thermal properties of polymers. In DSC measurements the heat flow (dH/dt) between the sample and a reference material of identical temperature is recorded as a function of temperature. From the heat flow as a function of temperature, thermal parameters of the polymer like melting and crystallization temperature, glass transition and degradation temperature can be derived. The heat flow corresponds to enthalpy changes (eq. 23) since DSC experiments are typically carried out at constant pressure.

$$\left(\frac{dq}{dt}\right)_p = \frac{dH}{dt} \qquad 23$$

Integrating (dH/dt) a melting endotherm over a defined baseline yields the total enthalpy change. For illustration, the melting endotherm of *i*PP is shown in Figure 15.

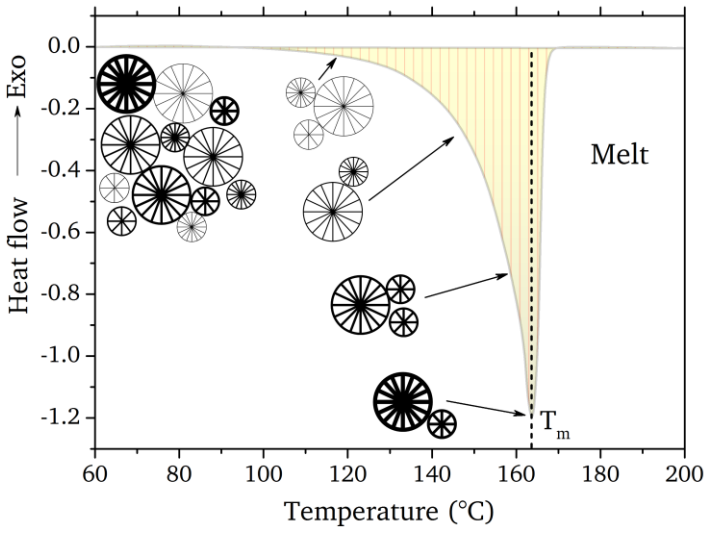

Figure 15: Melting endotherm of iPP showing the schematic representation of the distribution of spherulites with varying lamella thickness [52].

The area under a melting endotherm (Figure 15) represents the enthalpy of fusion (ΔH). The ratio between the enthalpy of fusion of a sample and that of the same material with 100 % crystallinity (ΔH^0) yields the fraction of crystalline phase, X_C^{DSC}, of the sample.

$$X_C^{DSC} = \frac{\Delta H}{\Delta H^0} x100 \qquad 24$$

The enthalpy of fusion may vary for individual polymorphs of a given material, and in the case of iPP the enthalpy of fusion for the α- and β-phase, ΔH_α^0 and ΔH_β^0, respectively, differs. Consequently, the contribution of both polymorphs has to be considered for samples containing α- and β-phase.

$$\Delta H^0 = K_\alpha * \Delta H_\alpha + K_\beta * \Delta H_\beta \qquad 25$$

where ΔH_α and ΔH_β are the enthalpy of fusion of the α- and β-phase, respectively. The fraction of α- (K_α) and β- (K_β) polymorph can be calculated individually using eq. 26 and eq. 27 [53].

$$K_\alpha = \frac{\frac{\Delta H_\alpha}{\Delta H_\alpha^0}}{\frac{\Delta H_\beta}{\Delta H_\beta^0} + \frac{\Delta H_\alpha}{\Delta H_\alpha^0}} = \frac{X_c^\alpha}{X_c^\beta + X_c^\alpha} \qquad 26$$

Analogously, K_β is given by

$$K_\beta = \frac{\frac{\Delta H_\beta}{\Delta H_\beta^0}}{\frac{\Delta H_\beta}{\Delta H_\beta^0} + \frac{\Delta H_\alpha}{\Delta H_\alpha^0}} = \frac{X_c^\beta}{X_c^\beta + X_c^\alpha} \qquad 27$$

Eq. 25 can be transformed into eq. 28 by substituting K_α and K_β.

$$\Delta H^0 = \frac{X_c^\alpha}{X_c^\beta + X_c^\alpha} * \Delta H_\alpha + \frac{X_c^\beta}{X_c^\beta + X_c^\alpha} * \Delta H_\beta \qquad 28$$

X_C^{DSC} of a PP sample containing α- and β-polymorph can now be calculated using eq. 29.

$$X_C^{DSC} = \left(\frac{\Delta H_\alpha + \Delta H_\beta}{\frac{X_c^\alpha}{X_c^\beta + X_c^\alpha} * \Delta H_\alpha + \frac{X_c^\beta}{X_c^\beta + X_c^\alpha} * \Delta H_\beta} \right) x100 \qquad 29$$

6 Experimental Part

6.1 Ageing Test

6.1.1 Ageing by chlorinated hot water

Pipes extruded from two grades of differently nucleated commercial PP, PP-R1 (α-nucleated) and PP-R2 (β-nucleated), stabilized with different content of hindered phenolic AO, were installed in a Wallace & Tiernan® chlorination system OSEC®, constructed by IPT Todtenweis, Germany (Figure 16).

Figure 16: Instrumental setup for the chlorinated water tests.

The flow rate of the inner liquid medium (chlorinated water/hot water) was set to 0.5 L/min. The chlorine concentration was set to 1.0, 4.0 and 10.0 mg/L, respectively, and the pH value was adjusted to 6.8. The resulting oxidation reduction potential (ORP) was in the range of 900 mV. These parameters were taken from ASTM F 2023 [54]. The protocolling and variation of different parameters during testing are representatively depicted in Figure 17.

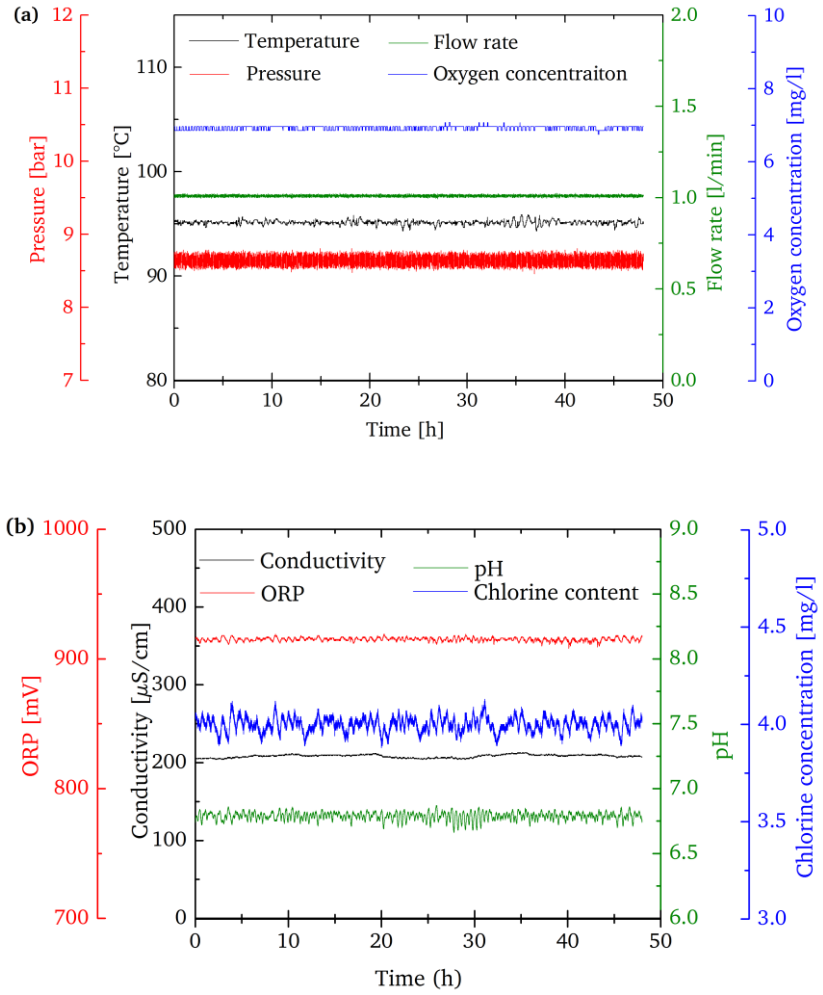

Figure 17: Variation of different ageing parameters with time.

The ageing parameters were found to be consistent with time.

6.1.2 Ageing by hot water

Hydrostatic pressure tests were carried out according to [55]. The experiments were performed in test baths and with pressure testers both manufactured by IPT (Todtenweis). Hot deionized water was applied to the pipe from both the inner and the outer surface.

6.2 Welding

Plates of two grades of PP homopolymer (PP-H1 and PP-H2) were joined by hot plate welding and obtained from SKZ, Germany. The plates were made by injection molding. The parameters used for the injection molding and welding of the plates are given in Table 1 and Table 2.

Table 1: Parameters used for injection molding of the plates.

Time(s)/Temperature (°C)	PP-H1	PP-H2
Injection time	1.64	1.86
Hold pressure time	25	25
Cooling time	25	25
Melt temperature	220	200

Table 2: Parameters used for welding

Time(s)/ Temperature (°C)	PP-H1	PP-H2
Hot plate temperature (°C)	220	220
Hold pressure time (s)	190	190
Cooling time (s)	180	180

6.3 Attenuated total reflectance infrared spectroscopy

The infrared spectra of the samples were recorded on a Nicolet 8700 spectrometer equipped with an MCT-A detector (mercury cadmium telluride, narrow band mid-IR: 4000-650 cm^{-1}). A background spectrum was recorded prior to the analysis of a sample. 16 scans were accumulated for both the background and sample spectrum at a spectral resolution of 4 cm^{-1}.

6.4 Infrared microscopy

Sections of 100 ± 5 μm thickness were prepared using a Reichert Jung rotary microtome. An IR microscope (Thermo Nicolet Continuum from Madison, WI), equipped with an MCT-A detector (narrow band mid-IR: 4000-650 cm^{-1}), was used for analysis. It was coupled to a Nicolet-Nexus 670 FT-IR spectrometer as a beam source (Figure 18). 100 scans at a spectral resolution of 4 cm^{-1} were accumulated per spectrum. A background spectrum using the same experimental parameters was recorded before each line scan/area map.

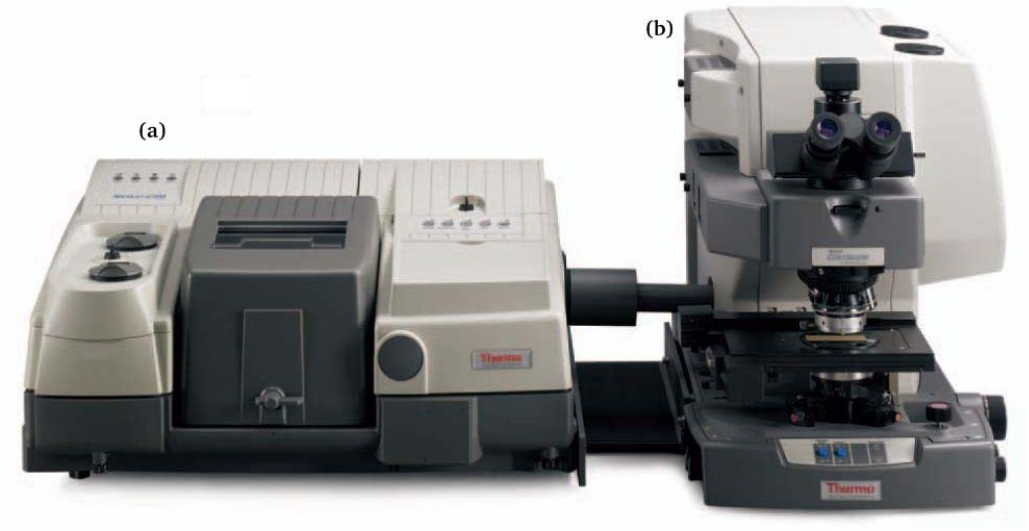

Figure 18: Instrumental set up of μFT-IR (a) FT-IR spectrometer and (b) microscope.

The aperture was set to 100 x 100 μm^2 and the step width of the line scans was 100 μm. A microvice sample holder was used to fix the sample. All measurements were carried out in transmission mode.

6.5 Polarized light microscopy

Sections of 10 μm thickness were prepared using a Reichert Jung rotary microtome. These cuts were fixed between a glass slide (of 1 mm thickness) and a cover slide (of 0.15 mm thickness) by using an acrylate resin. A microscope (BX50 F, Olympus), equipped with UPlan objectives, a rotatable polarizer (U-POT) and analyzer (U-AN360) was used.

6.6 Determination of additive content

The content of the AO was determined by extraction and subsequent HPLC analysis [56]. The additives were extracted from the cryomilled material of the pipe wall by refluxing with toluene as solvent and methanol as co-solvent. After filtration through a 0.45 μm polytetrafluoroethylene syringe filter the solutions were directly injected in the HPLC-UV system. The analyses were carried out on a Shimadzu LC20, equipped with two LC20AD pumps, an SIL-20A auto sampler, a CTO-20AC column oven and a SPD-M20A photodiode array detector. The stationary phase was Agilent Zorbax ODS (dimensions: 150 x 4.6 mm, L x I.D.) with an average particle size of 5 μm. The quantification was carried out at $\lambda = 270$ nm using the internal standard technique.

6.7 Calibration of antioxidant content

Plates of PP-R with defined content of AO-18 and AO-13 were prepared by cryomilling PP-R powder with the chosen contents of AO-18 and AO-13 followed by compression molding. Sections of 100 ± 5 μm thickness were prepared from the plates for μFT-IR using a Reichert Jung rotary microtome. The spectra of these microtome cuts were recorded in the same way as for the pipe samples. 10 points were measured for each sample and averaged to determine the standard deviation. 100 scans with a spectral resolution of 4 cm^{-1} were accumulated for each spectrum.

6.8 Differential scanning calorimetry

A DSC 220 from Seiko Instruments (Torrance, CA) was used to determine the oxidative induction time (OIT). The OIT was measured in isothermal mode under a nitrogen atmosphere at 200 °C. The OIT values were calculated according to [57].

6.9 Size exclusion chromatography

A high-temperature chromatograph PL 220 (Polymer Laboratories, Varian Inc, Church Stretton, England) was used to determine the MMD. The temperature of the injection sample block and of the column compartment was set at 150 °C. The flow rate of the mobile phase was 1 mL/min. Samples of ~20 μm thickness were taken from the inner surface of the pipe wall and dissolved for 2 h in 1,2,4-trichlorobenzene (containing 2 g/L butyl hydroxytoluene) at a concentration of 1 mg/mL at 150 °C. Polystyrene standards (Polymer Standards Service GmbH, Mainz, Germany) were used for calibration of a column set (3 PL gel Olexis columns Mixed B, 300 x 7.5 mm (L x I.D.), with an average particle size of 10 μm, Polymer Laboratories, Varian Inc, Church Stretton, England). An IR detector was used for detection.

7 Results and discussion

In order to evaluate the effects of welding and deteriorating environments on PP, various analytical methods were used as described in section 5. The effects of welding were studied for hot plate welded PP (PP-H1 and PP-H2), which gains importance to prepare complex structures from semi-finished goods. In welding a complex interplay between high heating and cooling rates as well as mechanical forces exists, which leads to a local extinction of the original morphology in the welding partners, and the rise to a new morphological structure in the weld.

7.1 Chemical and morphological analysis of the welded samples

7.1.1 Infrared spectroscopy

The infrared (IR) spectrum of the plate molded from PP-H1 is shown in Figure 19 and the characteristic absorptions of the polymer have been assigned and tabulated in Table 3.

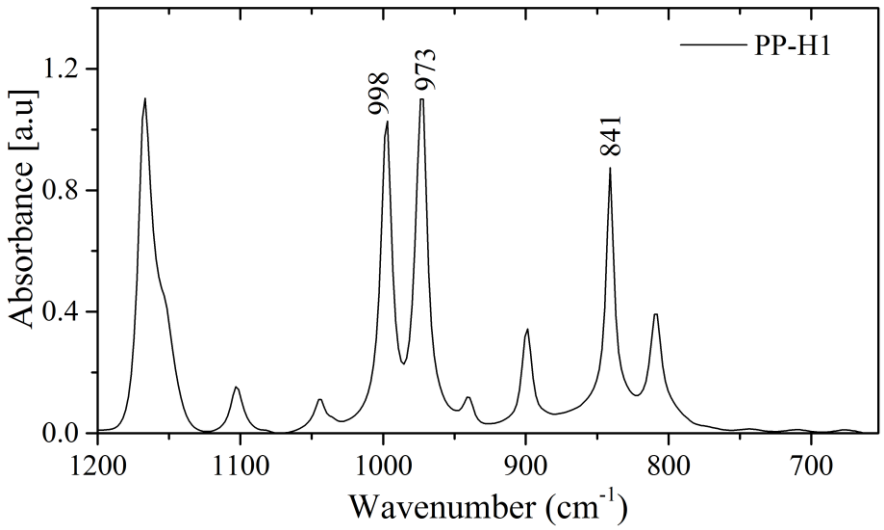

Figure 19: IR spectrum of the PP-H1 plate.

Table 3: Assignment of IR vibrational bands of PP-H [58-60].

Wavenumber [cm^{-1}]	Phase	α_T	Assignment	Integration limit [cm^{-1}]	
				Baseline	Region
841	Crystalline	0°	CH_2 rock + C-CH_3 stretch	862- 823	862- 841
974	Both	18°	CH_3 rock + C-C chain stretch	1018- 952	974- 952
998	Crystalline	18°	CH_3 rock + CH_3 wag + CH bend	1018- 952	1018- 998

In commercial polyolefins antioxidants (AOs) are regularly used in mixtures, containing various structurally or chemically different types. In order to identify absorptions which are specific for the additives IR spectra of the plates PP-H1 and PP-H2 were recorded. Enlargements from the carbonyl and hydroxyl region are presented in Figure 20.

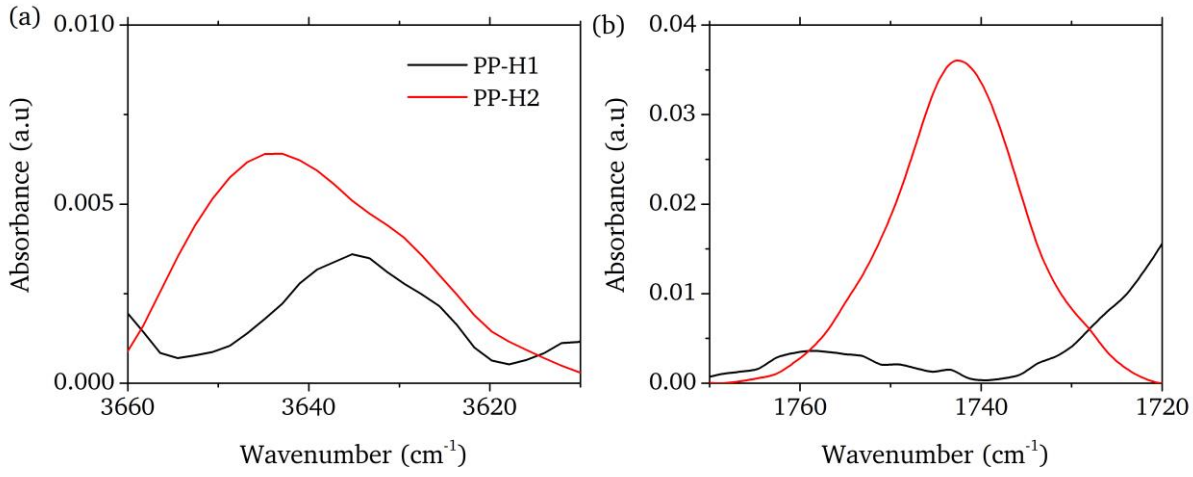

Figure 20: IR spectra of PP-H1 and PP-H2 displaying the vibrational bands characteristic for the AOs in the (a) hydroxyl and (b) carbonyl region.

The hydroxyl absorption centered at 3649 cm^{-1} and the carbonyl absorption at 1745 cm^{-1} can be assigned to the AO-18 present in the samples (see structure of AOs in Figure 8). The absence of these characteristic absorptions in PP-H1 clearly indicates the absence of AO-18. The X_c^{IR} calculated using eq. 22 is tabulated in Table 4.

Table 4: X_c^{IR} of PP-H1and PP-H2.

Sample	X_c^{IR} (%)
PP-H1	52 ± 1.2
PP-H2	54 ± 2.9

Both PP-H1 and PP-H2 showed almost the same percentage of crystallinity.

7.1.2 Size exclusion chromatography

The molar mass distributions (MMD) of the samples are presented in Figure 21 and the average molar masses of the corresponding samples are tabulated in Table 5.

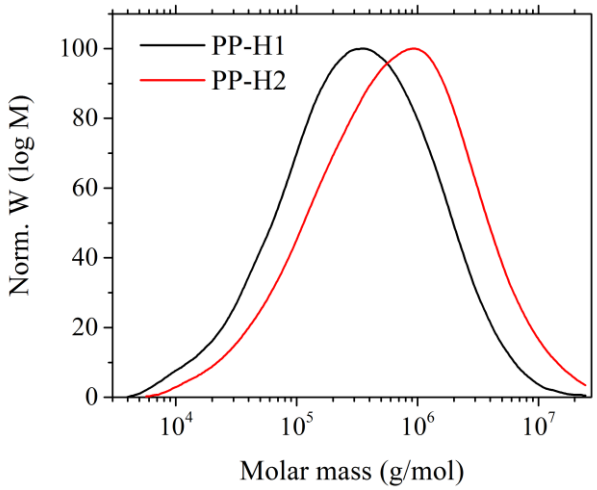

Figure 21: MMD of PP-H1 and PP-H2.

Table 5: Average molar masses determined for PP-H1 and PP-H2.

Sample	M_w (x 10^6 g/mol)	Dispersity index
PP-H1	0.89	8
PP-H2	1.73	9

Figure 21 shows that the MMD of PP-H1 and PP-H2 differ significantly with the average molar mass of PP-H2 being higher.

7.1.3 Differential scanning calorimetry

The thermograms of the first heating cycle of PP-H1 and PP-H2 are presented in Figure 22.

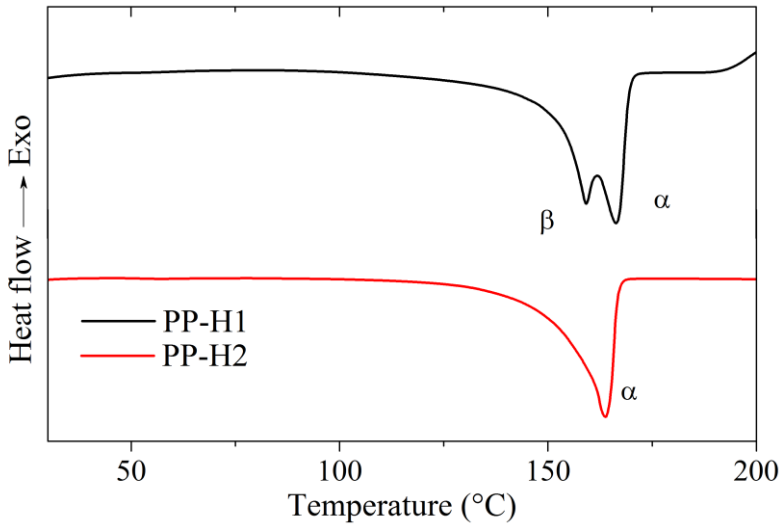

Figure 22: Melting endotherms of PP-H1and PP-H2.

Figure 22 reveals structural differences in the crystallographic phase of the samples. PP-H1 depicts two melting peaks with maxima (T_m) at 159 and 166 °C, which can be assigned to the β- and α-polymorph of PP, respectively [53]. PP-H2 shows only one melting peak at 164 °C that corresponds to the α-polymorph [26, 27]. The fraction of α- and β-polymorph (eqs. 26 and 27), T_m and the degree of crystallinity, X_c^{DSC} (eq. 24), of the samples were determined and are listed in Table 6.

Table 6: T_m, content of α- and β- polymorph and X_c^{DSC} of the samples.

Sample	T_m (°C)		K_α (%)	K_β (%)	X_c^{DSC} (%)
	α	β			
PP-H1	166	159	35	65	50
PP-H2	164	--	100	--	54

7.1.4 Polarized light microscopy

PLM analysis was performed to investigate the morphology of the injection molded plates. Samples were taken from the middle of the plate thickness of PP-H1 and PP-H2. The PLM images are presented in Figure 23.

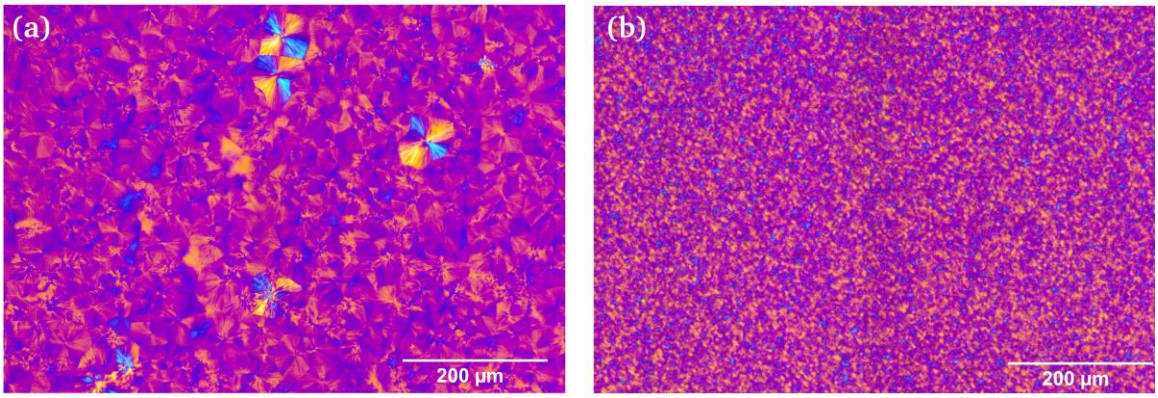

Figure 23: PLM images of (a) PP-H1 and (b) PP-H2.

PP-H1 has ideally grown well discernible α- and β-spherulites, while the spherulite size is very small in PP-H2, which is the result of fast crystallization caused by nucleation. The spherulitic structure of PP-H2 is difficult to differentiate by PLM and can be identified as predominantly α from DSC in section 7.1.3.

7.1.5 Measuring the orientation of polymer chains in welded plates of PP-H

This section discusses the quantitative determination of the distribution of AOs as well as the chain orientation in the welds of two grades of PP, which differ in their additive composition and nucleation using IR microscopy.

Figure 24 shows the PLM images of the welds joining the plates of PP-H1 and PP-H2, with two areas chosen for in depth analysis and visually distinguishable regions marked.

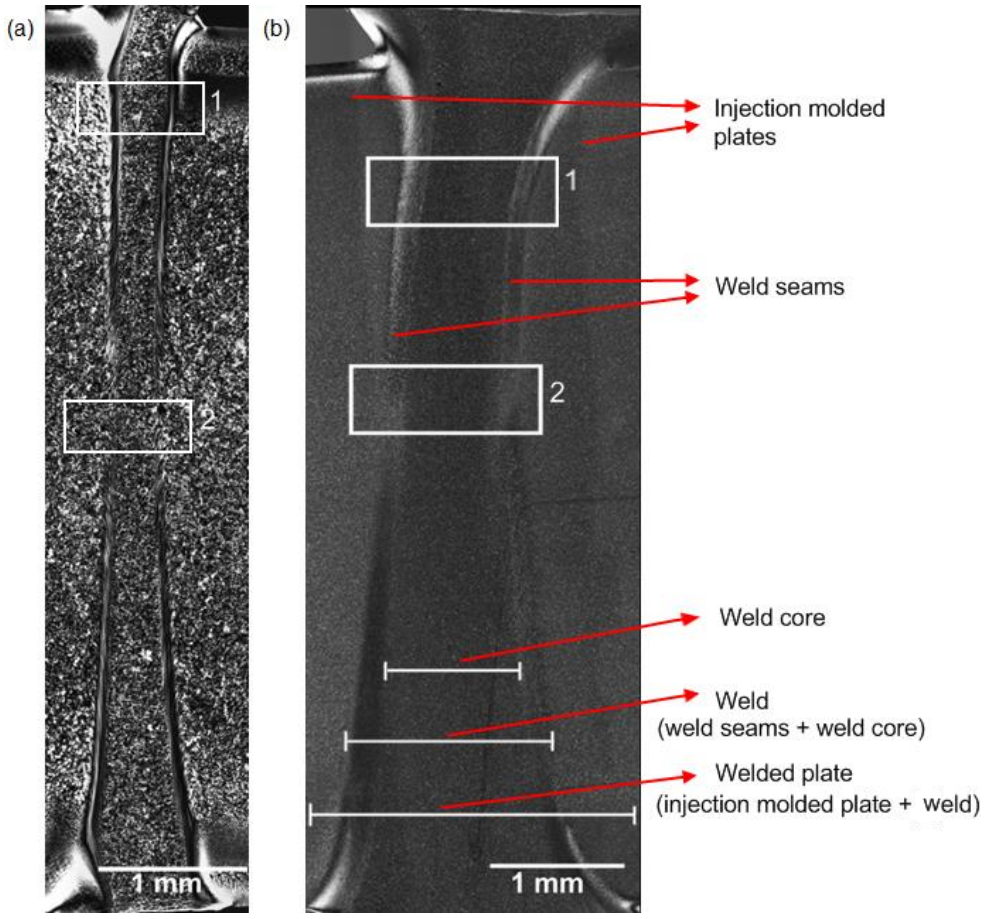

Figure 24: PLM image of the welds from MD-ND plane (a) PP-H1 (b) PP-H2.*

**MD= machine direction, ND= normal direction (see Figure 14 for details)*

It is clear from Figure 24 that two weld seams were formed at the boundary to the original plate morphology of each welded plate due to the outward melt flow, which is consistent with previous reports [61]. Two positions as denoted in Figure 24 were chosen in each weld to study the orientation of the macromolecules. In PP-H1position 1 displays two well defined weld seams that are almost absent at position 2, while in PP-H2 the weld seams are present at both positions. Furthermore, the weld seams in PP-H1 form a V-notch in the middle, whereas they are continuous in PP-H2. The formation of the V-notch depends on the depth of the molten polymer zone and the interpenetration of the polymer melt while shearing. Oliveira et al. showed how the V-notch is related to the melted zone depth and the ratio of melt displacement (RMD) [62]. According to this, a RMD value less than 0.5 resulted in the formation of a V-notch at the middle of the sample, whereas values > 0.5 lead to continuous weld seams. Since PLM fails to achieve the quantitative analysis of amorphous and

crystalline phase orientations in PP, infrared microscopy (μFT-IR) analysis was performed across the welds.

Figure 25 depicts IR spectra (with the light polarized along MD, TD and ND) recorded at one of the weld seams from position 1 and the PLM images from the two microtome cuts.

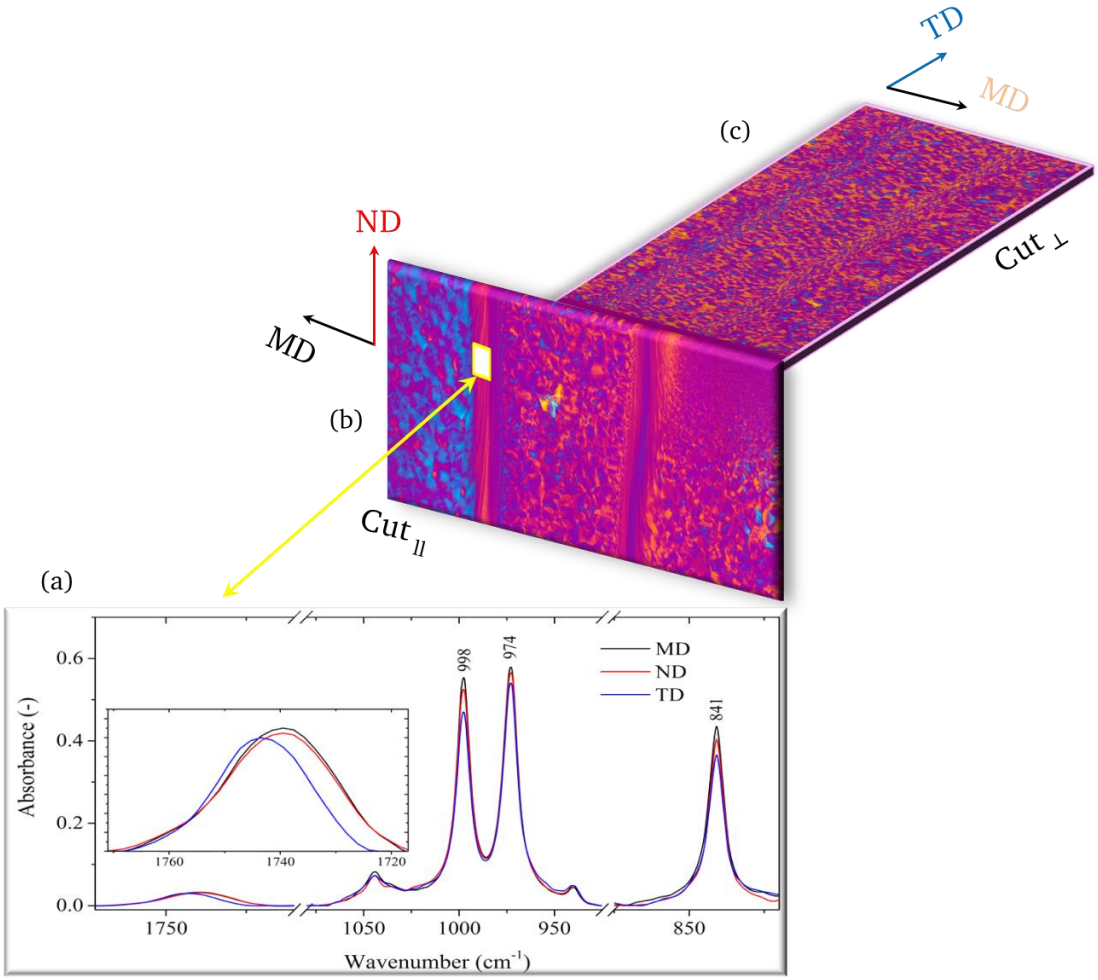

Figure 25: (a) IR spectra at one of the weld seams when the light is polarized along MD, ND and TD and PLM image of microtome cuts of (b) cut$_{ll}$ and (c) cut$_{\perp}$ of PP-H1.

The absorptions at 841, 974 and 998 cm^{-1} show significant differences in their intensity when the light is polarized along the three perpendicular directions. The direction of injection molding was taken as MD, and the dichroic ratio (D) was calculated for the band at 974 cm^{-1} with the two perpendicular directions ND and TD. The results along the line scan are plotted in Figure 26.

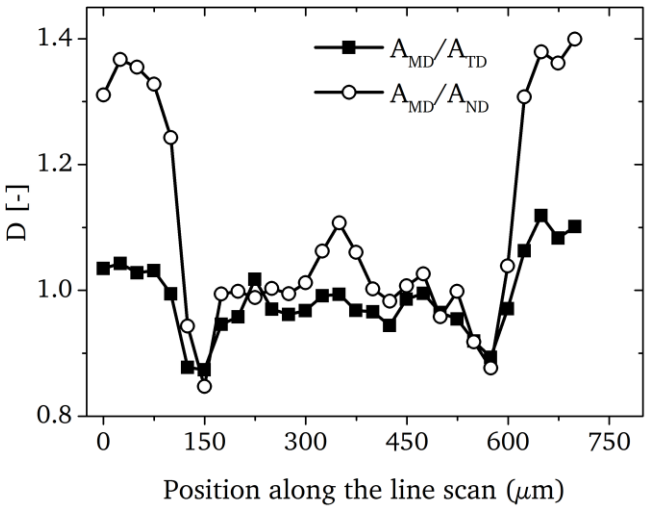

Figure 26: Profile of D for the band at 974 cm^{-1} in PP-H1.

A higher D value is obtained for MD/ND than for MD/TD in the injection molded plates, which proves that the polymer chains are oriented along MD and TD.

In order to obtain quantitative information about the chain orientation, which includes the both perpendicular directions, the values for Hermans orientation function (f) were calculated as described previously (section 5.2.2). Superstructures developed at the welds of position 1 were analyzed using PLM. Figure 27 shows the enlarged PLM image and the profile of f calculated from the absorption at 974 cm^{-1} at position 1 (f^{I}_{974}) of PPH-1 and PP-H2.

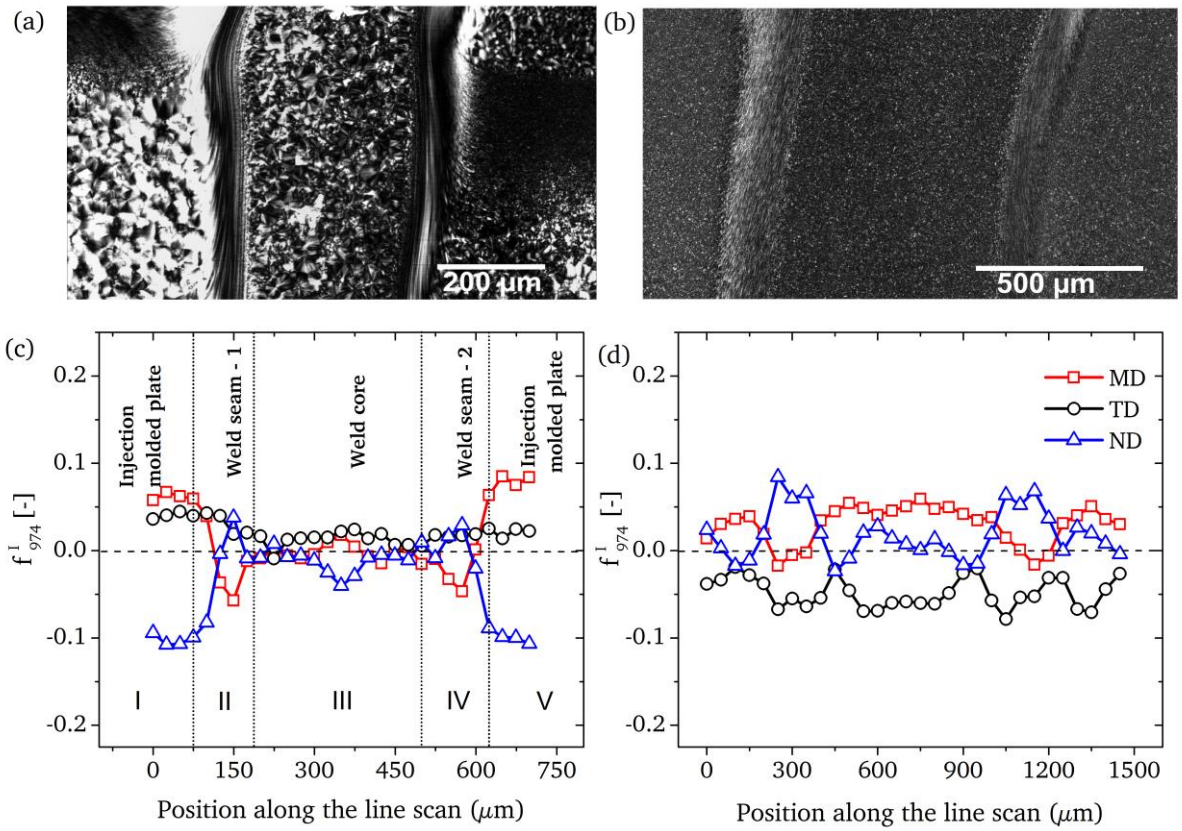

Figure 27: PLM images of (a) PP-H1 and (b) PP-H2 taken from the MD-ND plane and the profile of f^{I}_{974} *for (c) PP-H1 and (d) PP-H2.*

With regard to texture and spherulite size the superstructures of the welds differ significantly. The distinct regions developed accordingly in Figure 27 a and Figure 27 b are marked in Figure 27 c, which are in accordance with [63]. The temperature gradient in the welds ranges from equilibrium melting temperature at the seams to room temperature at positions remote from there. Consequently, the cooling rates experienced by the polymer molten to various degress were different, which in turn leads to the formation of distinct superstructures in the welds.

The orientation in the plates (zone I and V in Figure 27 c) along MD and TD reflects the parabolic filling of the polymer melt into the nest during injection molding. As a result of the melt flow during welding, the polymer chains experience a rearrangement from MD to ND (zone II and IV), which can be clearly recognized for both materials (Figure 27 c and d). At the core of the weld (zone III) of PP-H1 the chains are randomly oriented (f =0) (Figure 27 c), whereas at the weld core of PP-H2 (Figure 27 d) the orientation is along MD i.e., similar to the injection molded plates. When $f_x = f_y = f_z = 0$, the chain axis and the coordinates meet at an angle of 54. 7 ° ($\theta_x = \theta_y = \theta_z = 54.7$ °), which has been referred to as the magic angle [49]. For θ=

54.7 ° f converges to zero, which implies that the orientation of the polymer chain is isotropic. Due to the slow cooling experienced by the melt at the core ideal spherulites were formed in which the lamellae are orientated in all directions and, consequently, the tangentially aligned chains embedded in the radial lamellae are also oriented in all directions [17]. However, the orientation along MD in the injection molded plate and the weld core of PP-H2 can be explained as an effect of nucleation: due to nucleation, the crystallization rate increases, which ultimately results in the formation of fine spherulitic structures. The stress exerted on the polymer melt while injection molding is reflected in the chain orientation, which can be retained to a degree during crystallization, and lead to the formation of stretched spherulites. The orientation of such spherulites will then be along the direction of injection molding, with the extent of elongation depending on the crystallization rate.

The flow direction of the polymer melt in the nest and the resulting orientations of the polymer chains in the plates as well as those in the weld attained by injection molding and welding, respectively, are shown in Figure 28.

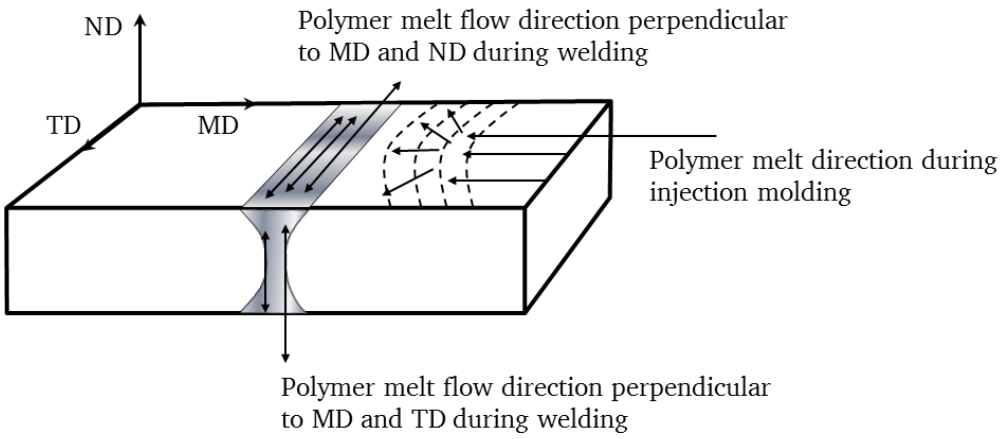

Figure 28: Flow directions of the polymer melt achieved in the plates and in the welding region during injection molding and welding.

Figure 29 shows the profile of f for the crystalline phase calculated from the absorption at 998 cm^{-1} (f^{I}_{998}) as well as the enlarged PLM images of zone II for PP-H1 and PP-H2.

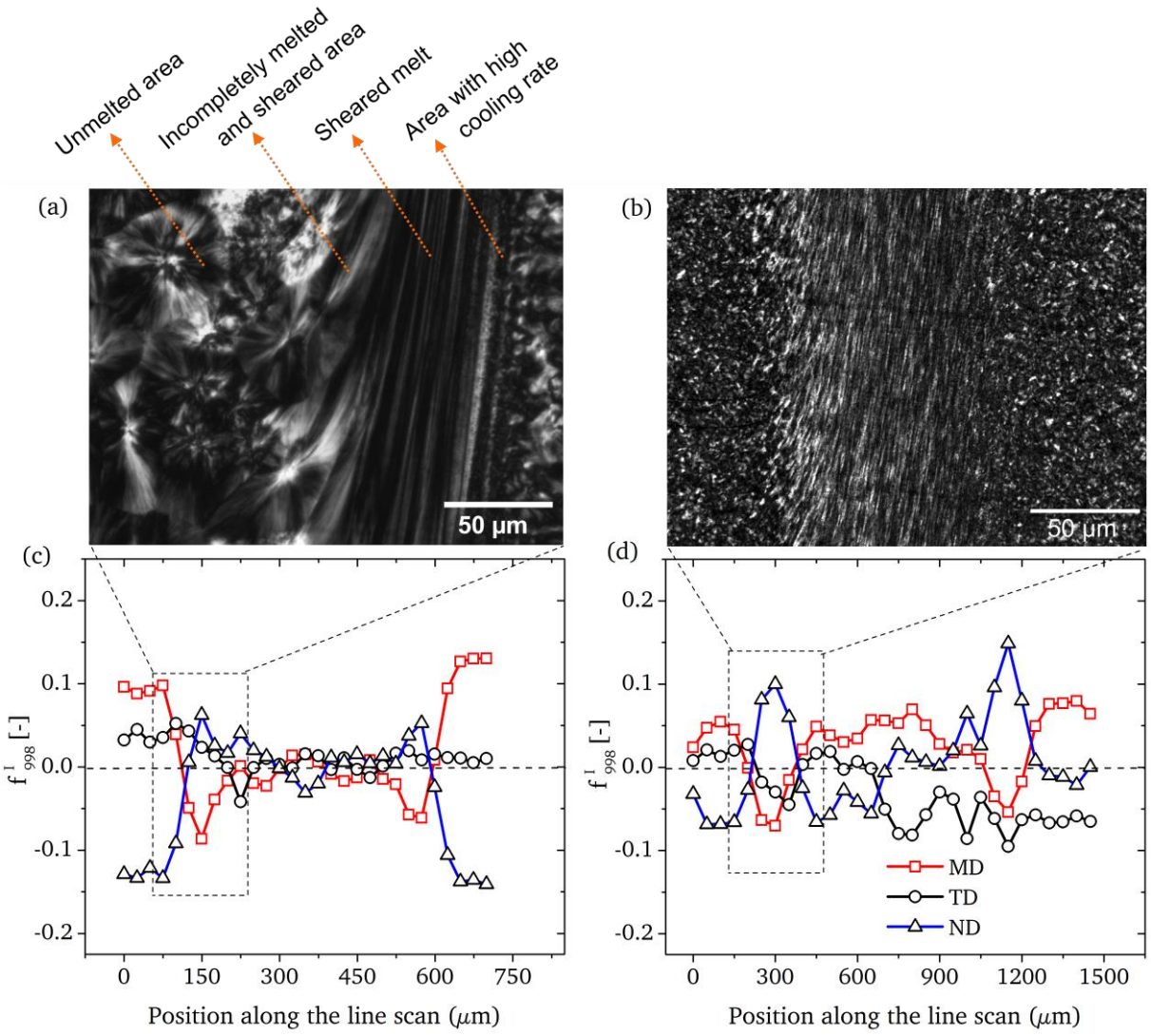

Figure 29: PLM images (MD-ND plane) from zone II of (a) PP-H1 and (b) PP-H2 and profile of f^{I}_{998} *for (c) PP-H1 and (d) PP-H2.*

The enlarged PLM image of zone II from PP-H1 and PP-H2 (Figure 29 a) clearly shows partly deformed spherulites close to the weld seams in PP-H1, whereas the small structures in PP-H2 (Figure 29 b) made it difficult to differentiate. Several layers of fine and distinct structures formed during welding have been marked in Figure 29 a, which are in agreement with the observations made by Tüchert et al. [63]. These areas are formed in the weld due to the differences in cooling rate experienced by the polymer at the weld during welding. When the samples are compressed, a shear force is exerted on the partly melted spherulites, and the completely melted PP starts to flow outwards. The rapid cooling under shear force then causes the formation of stretched spherulites in the completely melted region [63]. The completely melted PP of one plate interpenetrates with the same from the other plate due to the

compression during welding. The cooling rate of the polymer melt after removing the hot plates is highest in zone II and IV, leading to small spherulites in the vicinity of the weld seams.

The orientations of the macromolecules in the crystalline phase as well as the spherulite texture at position 1 were analyzed by μFT-IR and PLM, respectively. Figure 30 shows the orientation profile for the crystalline phase calculated from the absorption at 841 cm^{-1} (f^{I}_{841}) and the PLM images from zone IV and the middle of zone III.

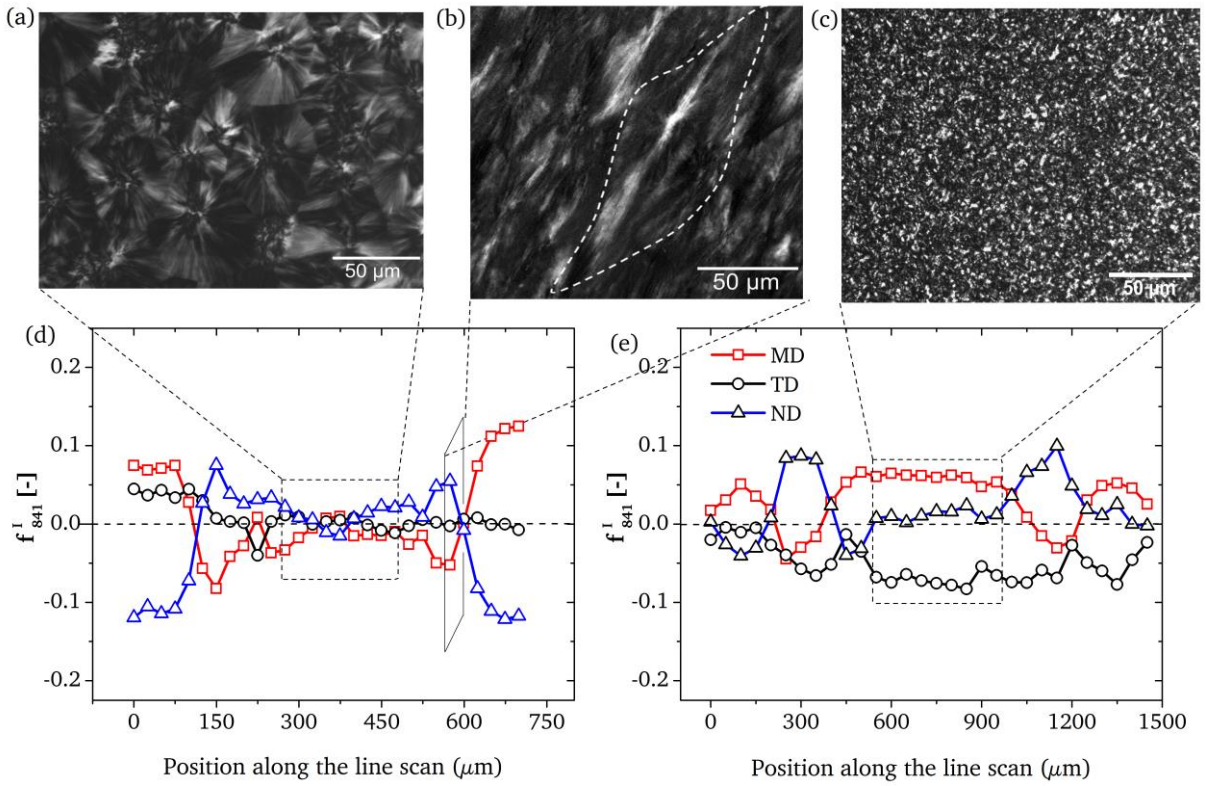

Figure 30: PLM image of PP-H1 (a) zone III (MD-ND plane) and (b) zone IV (TD-ND plane) and PLM image of PP-H2 (c) zone III (MD-ND plane) and profile of f^{I}_{841} for (d) PP-H1 and (e) PP-H2.

The texture of the polymer structures in zone III is retained when compared to the plates. Due to the difference in structure between the weld seams and the plates observed by the PLM images on MD-ND plane (Figure 29 a and b) the structure at zone II (Figure 30 a) was imaged from the TD-ND plane, which passes through the weld seam (Figure 30 b). Elongated spherulites [17] were found at the weld seam, which were formed as a result of sheared melt flow. The structure of the elongated spherulites is in accordance with the observations made by Way and Atkinson [64].

The shape of the profile of f^{I}_{841} is similar to that obtained from f^{I}_{998}. A remarkable difference between the orientation profiles of PP-H1 and PP-H2 is found at the middle of zone III: In the case of PP-H1, the chains at zone III are randomly oriented, while in PP-H2 the orientation is along MD. A schematic representation of the deformation of spherulites as shown by Samuels [17] is presented in Figure 31.

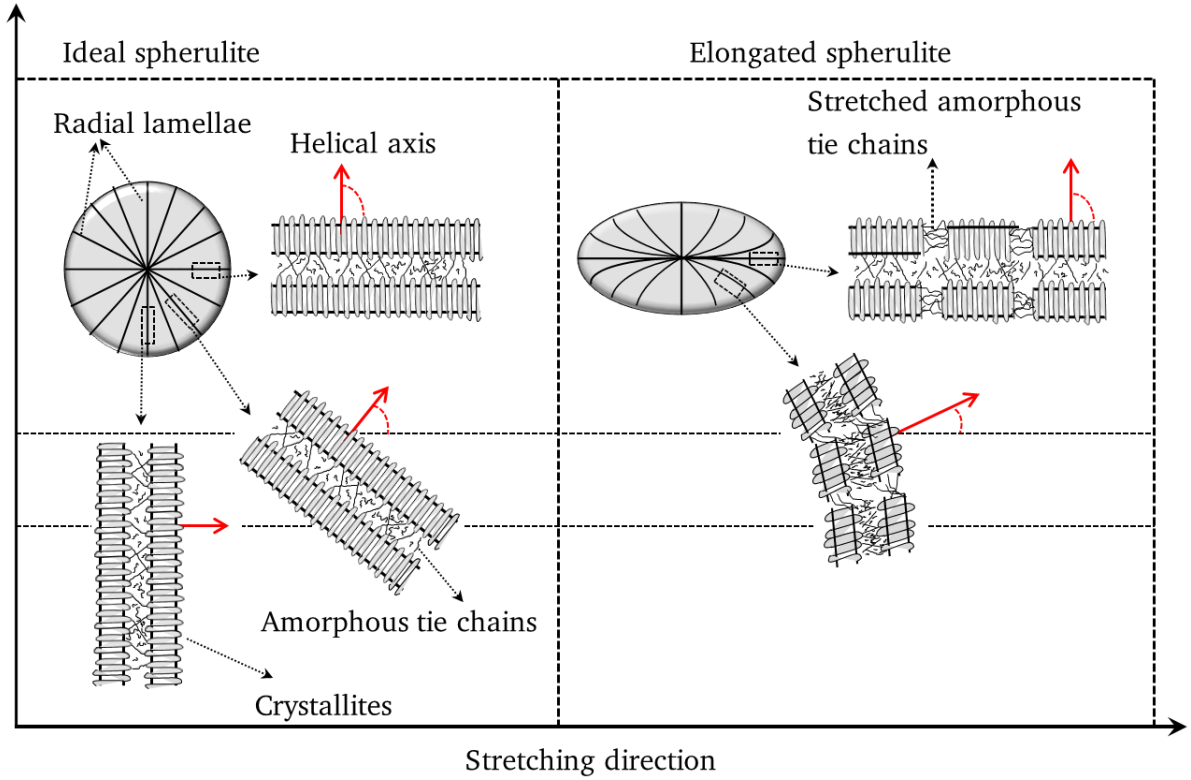

Figure 31: (a) Schematic representation of a spherulite showing the radial lamella and the perpendicular arrangement of the polymer chains (b) deformed spherulites showing the change in crystal c- axis with respect to the stretching direction.

A spherulite consists of radial lamellae in which crystalline and amorphous phases are present [65]. The crystalline domains of a spherulite constitute the crystallites in which the helical chains of PP are folded forth and back along the helical axis [66] i.e., vertical to the radial lamellae [6]. These crystallites are linked by tie chains, regarded as amorphous phases of a spherulite. The lamellae in a spherulite extend radially from the nucleation center to all directions. In the case of an ideal (non-deformed) spherulite, the crystalline and amorphous phase are isotropic i.e., no preferential orientation exists. Upon deformation, the amorphous tie chains are elongated first, and at higher deformation rates elongation of the polymer chains of

crystallites occurs, ultimately leading to a distortion of the crystal structure and, thereby, causing a reduction in X_c.

DSC analysis was performed on samples microtomed along the TD-ND plane of the welds of PP-H1 to monitor the polymorphic changes at the welds caused by melting and recrystallization. Figure 32 shows the melting endotherms of samples taken from the injection molded plate, the weld seam and the weld core of PP-H1 and the corresponding PLM images.

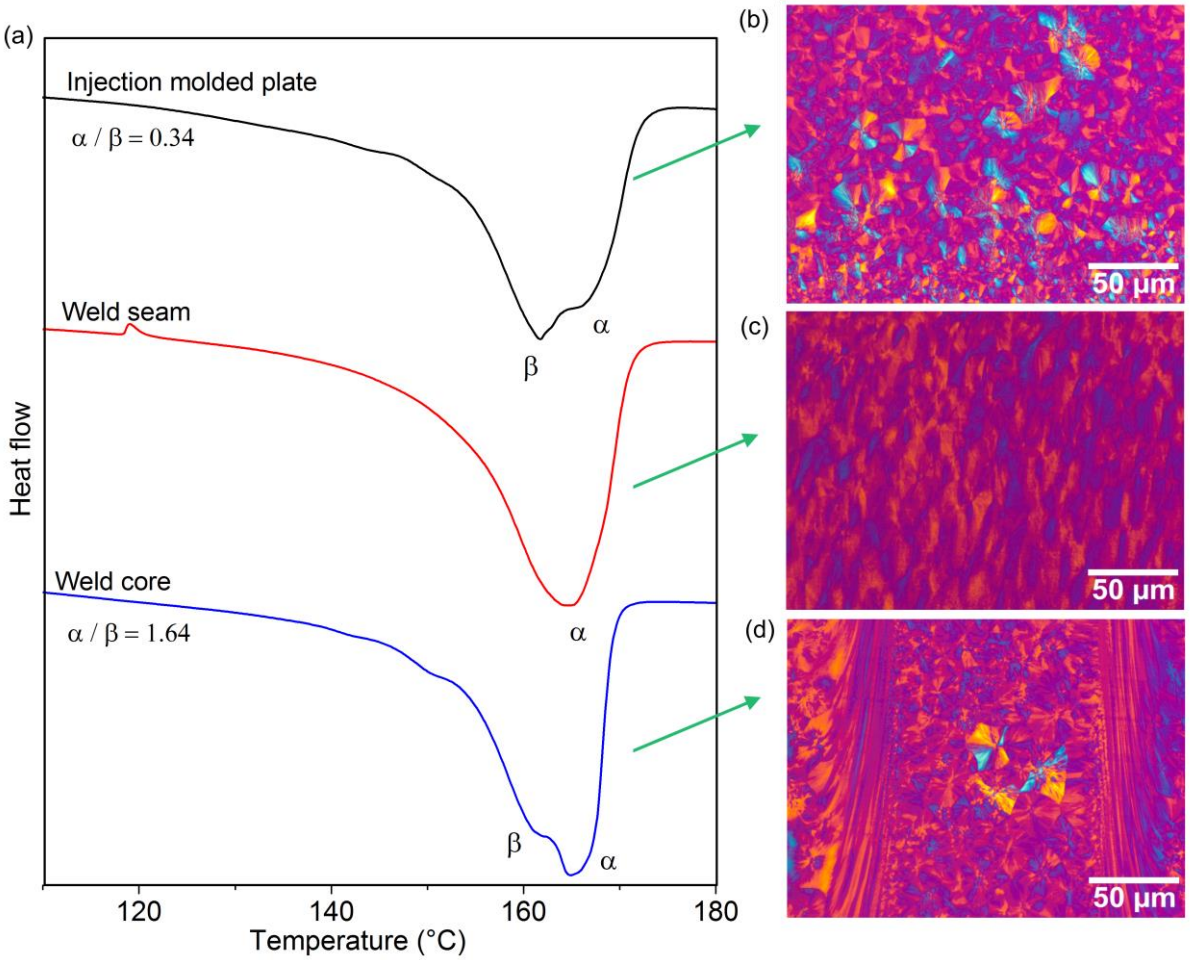

Figure 32: (a) Melting endotherms of samples taken from injection molded plate, weld seam and weld core of PP-H1 and (b) PLM images of injection molded plate (MD-ND plane), (c) weld seam (TD-ND plane) and (d) weld core (MD-ND plane).

It can be recognized that the injection molded plates, the weld seams and the weld core differ in their polymorphic composition (Figure 32 a). While the weld core shows the presence of α- and β-polymorph, the latter cannot be found in the weld seam. A quantitative analysis of the ratio between α- and β-polymorph from the DSC measurements substantiates the observations from PLM analysis with a good correlation. The formation of β-spherulites is favored within a narrow range of

crystallization temperature and, hence, a low cooling rate and a longer crystallization time lead to the formation of β-spherulites [67]. On the contrary, fast cooling of iPP favors the formation of α-spherulites [68, 69] and, therefore, it can be concluded that the high cooling rates at the weld seams caused the formation of α-spherulites, while the lower cooling rates at the weld core met the crystallization conditions of α- and β-spherulites.

X_c across the welds of PP-H1 and PP-H2 was calculated from μFT-IR and DSC of mechanically prepared sections and Figure 33 shows the profiles of X_c^{IR} and X_c^{DSC} across the welds.

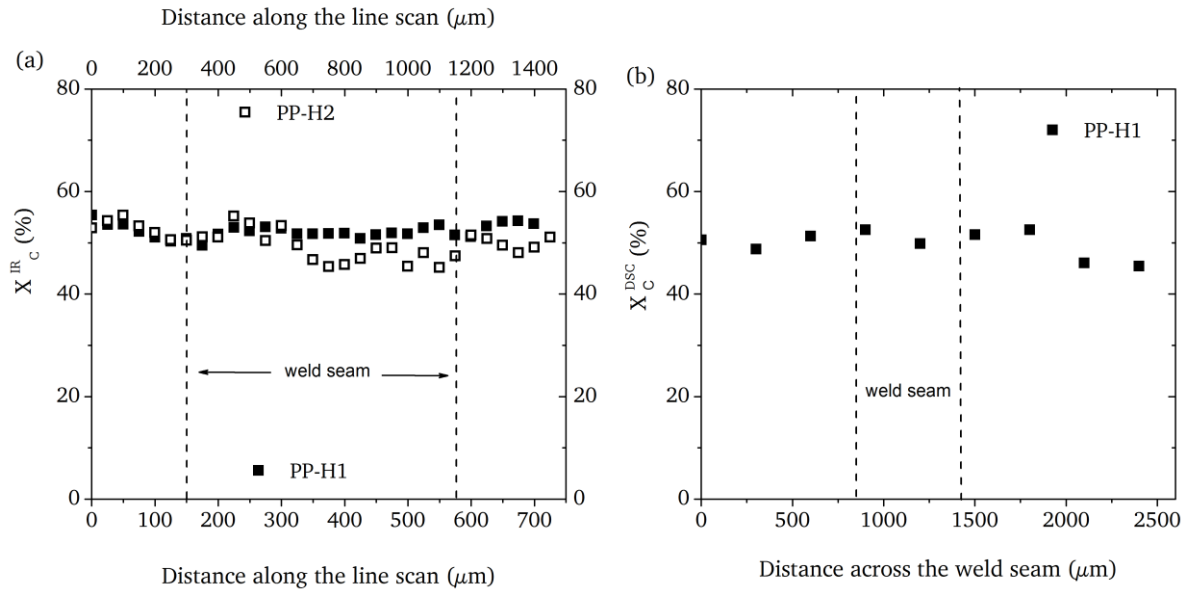

Figure 33: X_c across the welds of PP-H1 and PP-H2 (a) X_c^{IR} and (b) X_c^{DSC} .

The profile of X_c^{IR} for PP-H1 corresponds well with that of X_c^{DSC} (Figure 33). X_c is almost constant across the welds at position 1 for PP-H1 and PP-H2 (Figure 33). The observed constancy of X_c across the welds indicates that the crystal structure of the spherulites was retained after welding, and that the shear force was not sufficient to distort the crystallites. Although leading to similar results, a crucial advantage of the μFT-IR approach over that with DSC-analysis of mechanically prepared cross-sections is the high spatial resolution of the first (down to 10 μm). In the latter case the mechanical preparation of the samples sets a limit, which, depending on practical skills and instrumentation, is around 300 μm. Yet, this clearly underlines the potential of μFT-IR to retrieve quantitative information about the polymer morphology in welds.

Crystallization under shear force occurred in the weld seam, which is a well known mechanism in the case of semicrystalline polymers [70]. Consequently, stretched or elongated spherulites were formed, as can be recognized from Figure 30 b. In the case of elongated spherulites the crystalline structures were not distorted, whereas the amorphous tie chains undergo elongation. As a result, the overall X_c of the spherulite remains unchanged. The consistency in X_c even at the weld seam can, therefore, be a result of the elongated spherulites identified at zone II by PLM.

Position 2 marked in Figure 24 was found interesting for the orientation measurements due to the presence and absence of a V-notch in the welds of PP-H1 and PP-H2, respectively. Figure 34 shows the enlargement of the PLM image from position 2.

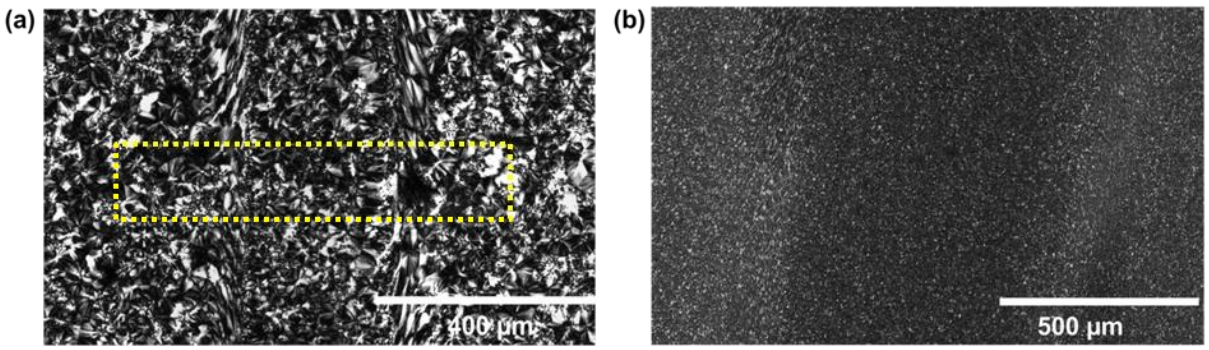

Figure 34: PLM image (MD-ND plane) from position 2 of (a) PP-H1 (b) PP-H2.

From Figure 34 the weld seams are completely absent in PP-H1 at position 2 as marked in Figure 34 a, whereas they are visible in PP-H2. The chain orientation at position 2 was calculated from the reference band as described previously. Additionally, the orientation of the chains in the crystalline phase was calculated. Figure 35 represents the profiles of f calculated from the absorptions at 974 (f^{II}_{974}) and 998 cm^{-1} (f^{II}_{998}), respectively.

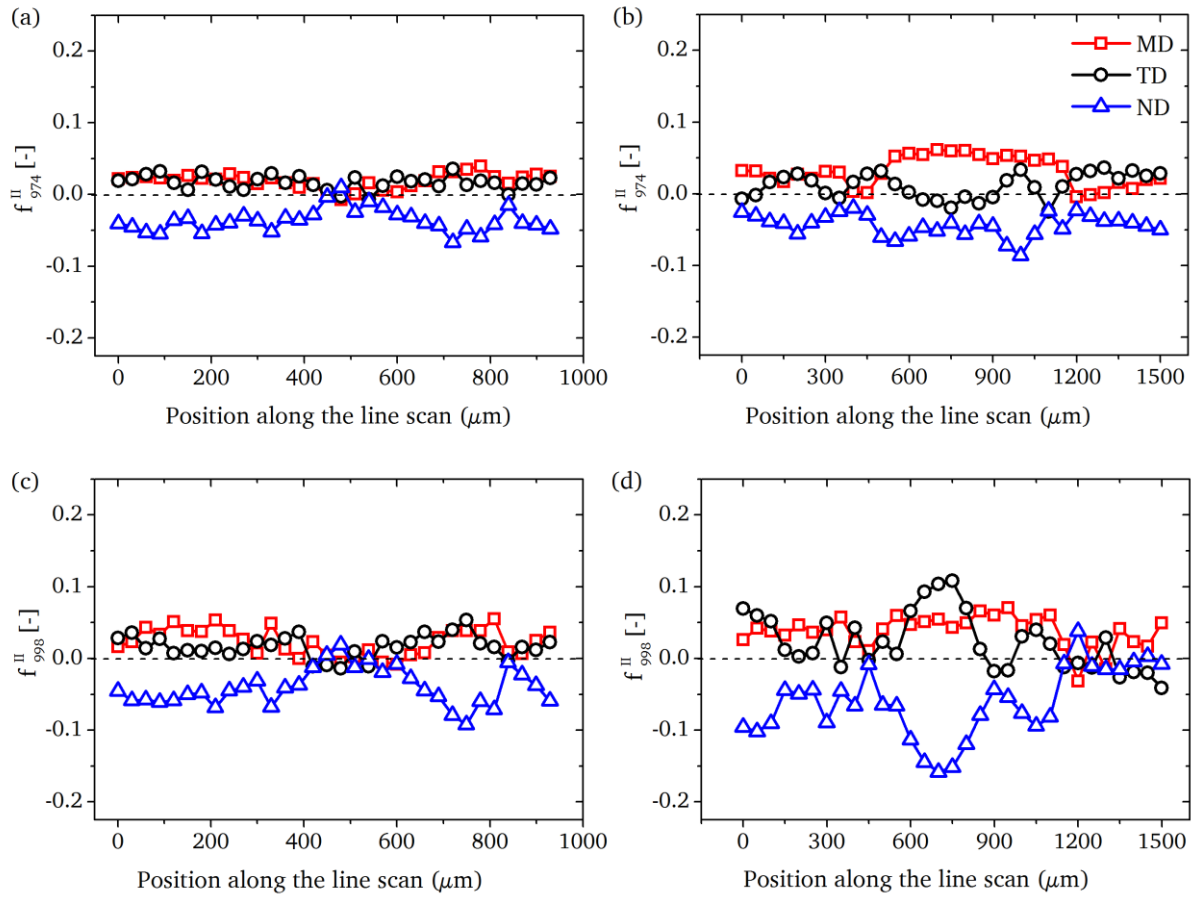

Figure 35: Profile of f calculated from the absorption at 974 cm^{-1} (a) PP-H1 and (b) PP-H2 and the absorption at 998 cm^{-1} (c) PP-H1 and (d) PP-H2.

The absence of the visual weld seam in PP-H1 is reflected in Figure 35 a and c, as the orientation is not changing its direction towards ND. However, at the halfway of the line scan f attains a value of zero, which indicates the presence of ideal spherulites i.e., the chain orientation is isotropic. This region can be considered as the center of the V-notch where the polymer melt experiences the lowest cooling rate as well as the highest degree of interpenetration. The orientation, except from the V-notch, is distributed almost equally in MD and TD. During injection molding, the melt at the middle of the MD-ND plane (position 2) experienced the longest cooling time, giving the chains maximum time for reorientation, which results in an f value close to zero. Orientations determined at position 2 of PP-H2 (Figure 35 b and d) show considerable differences compared to their counterpart in PP-H1. These differences are observed at the weld seams and the weld core. Unlike in the case of PP-H1, the orientation of the chains changes its direction from MD (as found in the plates) to ND upon welding. This confirms the presence of continuous weld seams along ND in PP-H2 and an interruption in the weld seams along ND at the middle in the case of PP-H1. From

Figure 35 d, the orientation at the weld core changes its direction to TD, which is a possible melt flow direction as shown in Figure 28.

An important question with respect to the long term behavior of welds is the distribution of stabilizers. The absorptions at 3649 and 1744 cm^{-1} in the IR-spectrum of PP-H2 (Figure 20) correspond to the aromatic hydroxyl and the ester carbonyl group of AO-18, respectively, and the vibration at 1082 cm^{-1} can be assigned to the P-O-C absorption of the processing stabilizer PS-2 [71]. Figure 36 shows the intensity distribution of the ester carbonyl-, hydroxyl- and P-O-C-absorptions in the weld and the injection molded plate of PP-H2.

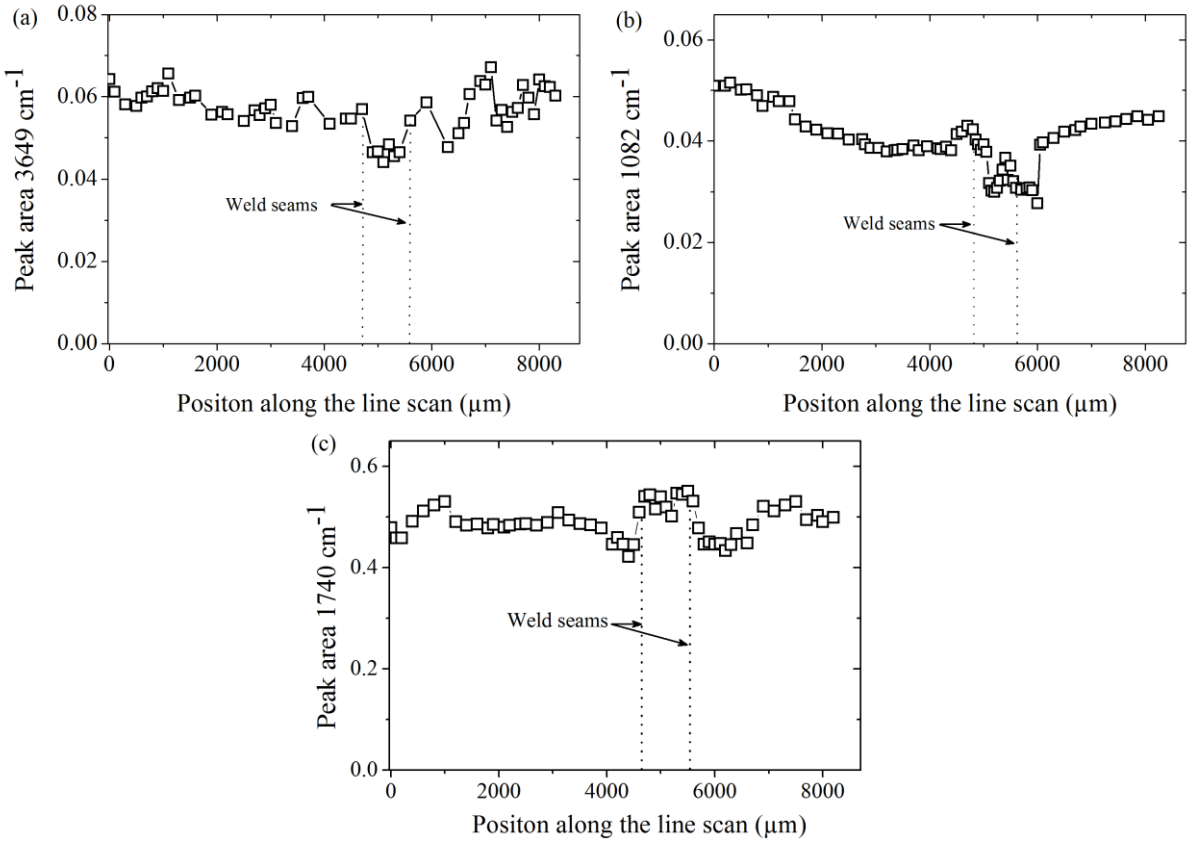

Figure 36: Distribution of peak areas of the absorptions corresponding to the AOs at the weld and injection molded plate of PP-H2 (a) hydroxyl area of AO-18 carbonyl area of AO-18 (b) P-O-C vibration of PS-2 (c) carbonyl area.

It can be recognized that the absorption of the phenolic hydroxyl group in the weld region is slightly lower than in the injection molded plate, which gives evidence of oxidative consumption of AO-18 during the welding (Figure 36 a). In the same sense, the minimum of the absorption at 1082 cm^{-1} reveals consumption of PS-2 (Figure 36 b). Interestingly, the intensity distribution of the carbonyl absorption shows a maximum at the weld core after passing local minima in proximity to the weld. The

minimum proves physical loss of AO-18 as a result of heating during welding. Yet, the maximum in the very weld core can be explained by the overlapping of the carbonyl absorption of polymer degradation products with that of AO-18 (Figure 36 c). Previous studies have shown that the ester carbonyl absorption of AO-18 is non-dichroic [50], while the carbonyl absorption in Figure 25 displayed significant dichroism, in which a higher intensity was observed when the electric vector of the IR light was polarized along MD. Compiled with the orientation of the polymer chains (also along MD) (Figure 27), this proves the presence of polymer degradation products in the weld core. A notable conclusion is that thermo-oxidative degradation of the polymer chains occurred even in the presence of AO-18 and PS-2.

7.1.6 Summary

Welds of non-nucleated and α-nucleated PP (PP-H1 and PP-H2 respectively) were analyzed by polarized light microscopy (PLM), IR microscopy (μFT-IR) and differential scanning calorimetry (DSC). From the experimental results the following conclusions can be made:

- Discrete zones of polymer structures formed in PP-H1 during welding were identified by PLM as unmelted area, incompletely and sheared area, sheared melt and area with high cooling rate.
- Deformation of the spherulites occurred at the weld seams
- Two positions in the welds, which differ in the continuity of the weld seams, were chosen for determination of polymer chain orientation. At position 1, both PP-H1 and PP-H2 display two well-defined weld seams, while at position 2 they were only observable for PP-H2.
- The polymer chains at position 1 of PP-H1 were oriented along MD at the injection molded plates, ND at the weld seams and random at the weld core. However, the orientation of polymer chains in PP-H2 differs from PP-H1 at the weld core, where the chains of PP-H2 were oriented similar to injection molded plates.
- At position 2, random orientation of polymer chains at the V-notch of PP-H1 was found due to the presence of clearly grown spherulites while in PP-H2 the effect of the nucleating agent prevents the chains to form ideal spherulites.
- The effect of melting and recrystallization on polymorphism was monitored by DSC and PLM at three distinct positions (injection molded plate, weld seam and weld core). In the case of PP-H1 showed the injection molded plate and the weld

core were enriched with α- and β-polymorph, while the weld seams consists of solely α-spherulites. The α-nucleation in PP-H2 caused the formation of only α-spherulites at injection molded plate, weld seams and weld core.

- The distribution of AO-18 and PS-2 showed that depletion of AOs during welding occurred due to physical loss and chemical consumption. Using the concept of dichroism it could be demonstrated that thermo-oxidative degradation of iPP occurred during welding, even in the presence of AOs.

7.2 Development of imaging techniques to analyze the impact of chlorine on PP-R pipes

Testing of pipes was carried out according to the methods described in section 6.1. The samples were subjected to a detailed analysis by analytical techniques and methods as described in section 5. This section includes four sub chapters (7.2.1 to 7.2.4) followed by a conclusion.

7.2.1 Chemical and morphological characterization of unaged pipes

7.2.1.1 Polarized light microscopy

PLM analysis was performed on specimen taken from the middle of the wall of PP-R1 and PP-R2 to investigate the morphology of the unaged samples. The PLM images are presented in Figure 37.

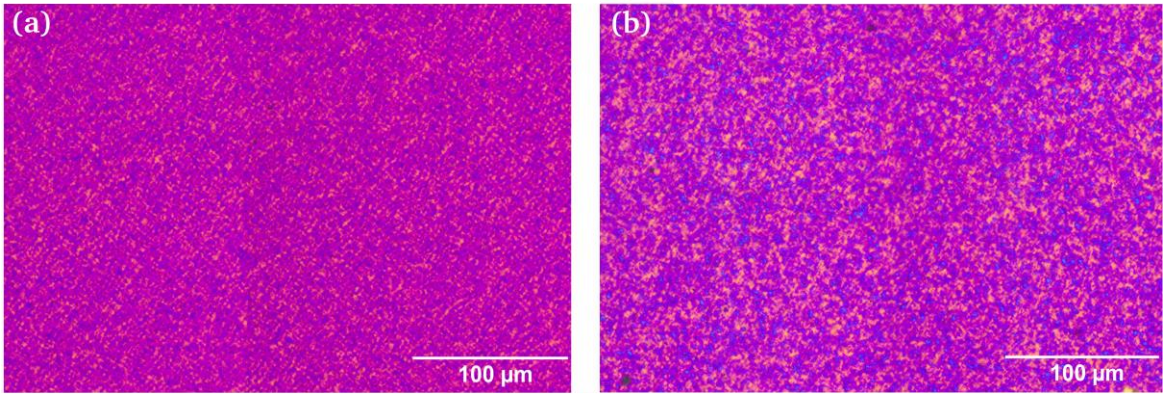

Figure 37: PLM images of (a) PP-R1 and (b) PP-R2.

The fine structures observed in the PLM images (Figure 37) prove that both PP-R1 and PP-R2 were nucleated.

As explained previously, PP-R1 and PP-R2 were prepared by extrusion and the morphology developed across the pipe wall was analyzed by PLM. Figure 38 shows the PLM images over the entire pipe wall as well as an enlargement from the inner and the outer surface of the pipe wall.

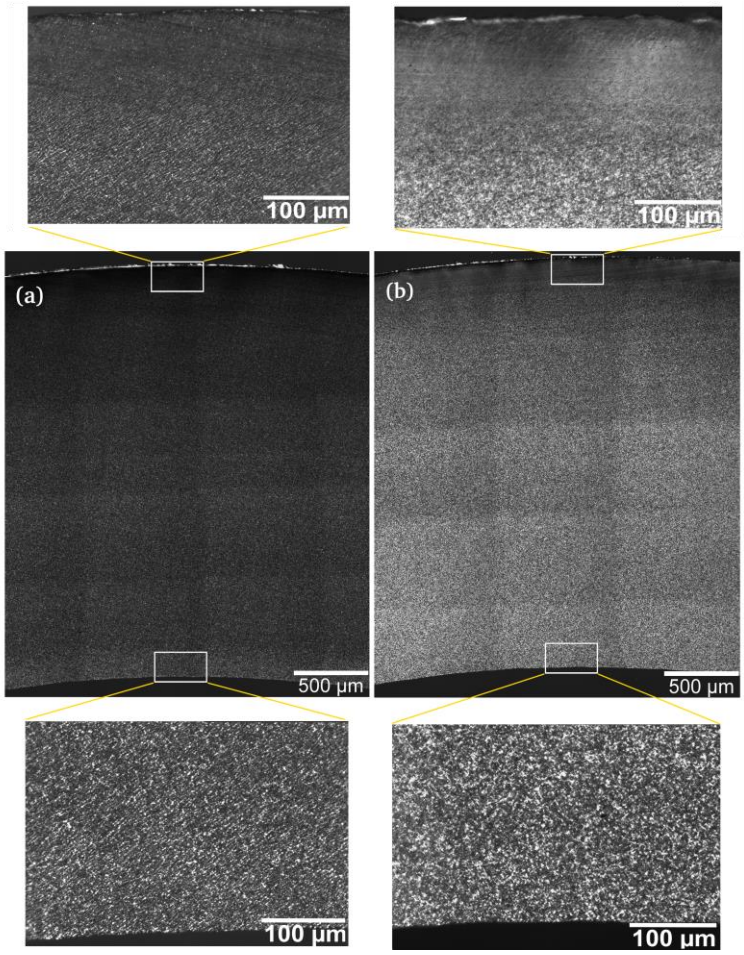

Figure 38: PLM images obtained from the microtome sections along the wall of the pipes (a) PP-R1 and (b) PP-R2.

The size of the spherulites decreases from the inner to the outer surface. During the extrusion of pipes, the inner surface was exposed to air and the outer surface was quenched with cold water. This characteristic temperature pattern leads to the difference in spherulite size between the inner and outer surface.

7.2.1.2 Differential scanning calorimetry

The endotherms of the first heating cycle of PP-R1 and PP-R2 are presented in Figure 39.

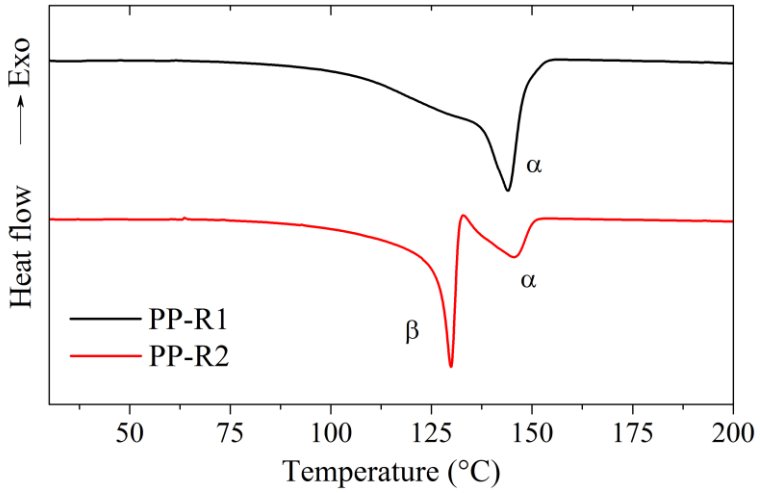

Figure 39: Melting endotherms of the samples taken over the wall of PP-R1 and PP-R2.

PP-R1 depicts a single melting peak with a maximum (T_m) at 144 °C, which can be assigned to the α-polymorph of PP, whereas PP-R2 depicts two melting peaks with T_m at 130 and 145 °C, which can be assigned to the β- and α-polymorph of PP, respectively (the incorporation of ethylene units lowers the T_m of β- and α-polymorph [72]). In the case of a β-nucleated iPP sample at non-isothermal crystallization conditions, simultaneous crystallization of both β- and α-polymorph can occur due to the narrow crystallization temperature range of the β-polymorph [73, 74]. The fraction of α- and β-polymorph (eq. 26 and 27) and the degree of crystallinity, X_c^{DSC} (eq. 24), were determined and are tabulated in Table 7.

Table 7: T_m, content of α- and β- polymorph and X_c^{DSC} of unprocessed/ unaged samples.

Sample	T_m (°C)		K_α (%)	K_β (%)	X_c^{DSC} (%)
	α	β			
PP-R1	144	--	100	--	34
PP-R2	145	130	39	61	33

The pipes chosen for this study were produced by extrusion, which generates a morphology gradient across the wall of the pipe with respect to spherulite size: After the nascent, still solidifying pipe leaves the dies, the outer layer was quenched by cold water and the inner surface was in contact with hot air. Consequently, crystallization started from the inner surface leading to the formation of spherulites there and the

size of these decreases towards the outer surface. Due to the complexity of the extrusion process and the temperature sensitivity of the formation of polymorphs, gradients with regard to the morphological parameters such as ratio of polymorphs, orientation of polymer chains and the compositional parameters such as distribution of additives or their degradation products can be expected. Therefore, a quantitative analysis with high spatial resolution along the sample thickness has to be performed to retrieve detailed information in this regard. The content of α- and β-polymorph was determined from DSC of samples prepared at different depths of the pipe (PP-R2) wall, and the respective profiles are presented in Figure 40.

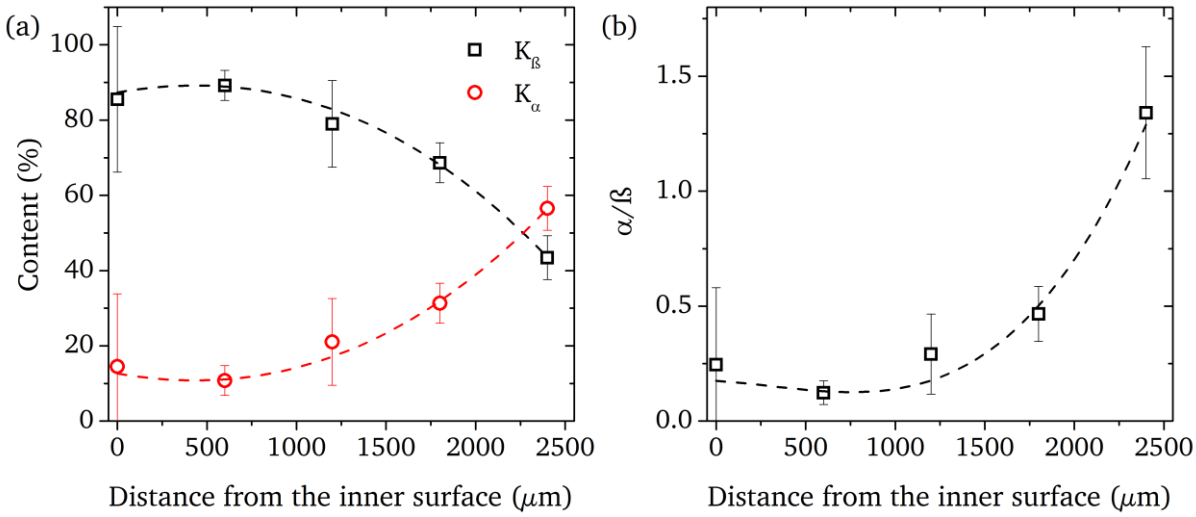

Figure 40: (a) Distribution of K_β and K_α (b) and ratio of the content of α- and β- from PP-R2.

The distribution of K_β and K_α is inversely proportional to each other. At the inner surface of the pipe, crystallization relevant parameters such as cooling rate and the presence of β-nucleating agent favor the formation of β-polymorph, however, with a concomitant amount of α-polymorph. Due to the gradient of temperature from the inner to the outer surface of the pipe wall, crystallization conditions increasingly disfavor the formation of β-polymorph, while at the same time fostering the formation of α-polymorph.

7.2.1.3 Quantification of additives

IR-spectra of PP-R compounds with varying content of AO-18 were recorded and the area of the carbonyl absorption plotted as a function of the nominal antioxidant (AO) content, which then was used to quantify AO-18 (Figure 41).

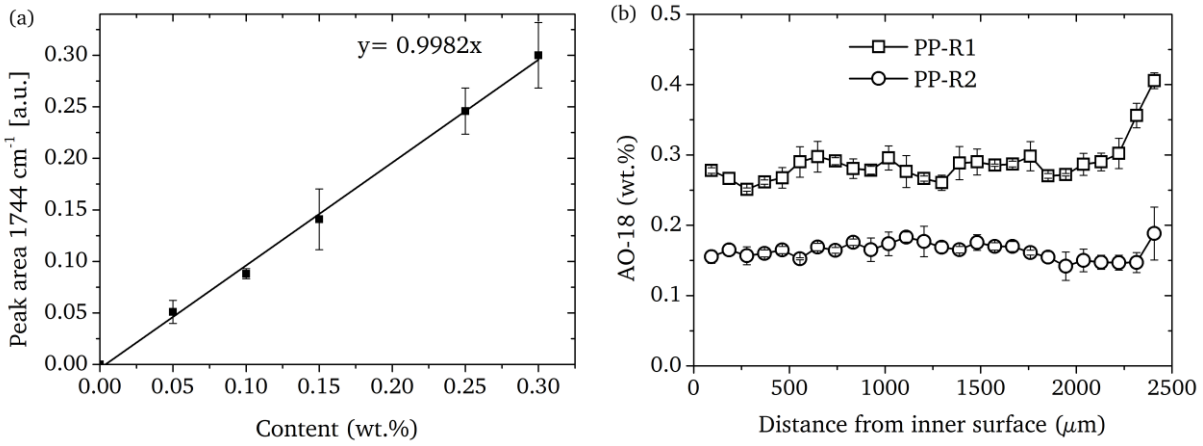

Figure 41: (a) Calibration curve of AO-18 using the IR band at 1744 cm^{-1} and (b) distribution of AO-18 in PP-R1 and PP-R2 across the pipe wall.

The slope (m) of the calibration curve in Figure 41 corresponds to the product of path length and absorption coefficient for the ester carbonyl band in eq. 16. Figure 41 b reveals that the AO-18 is inhomogeneously distributed across the wall of PP-R1, with a higher content in the outer 200 μm. On the contrary, the distribution is almost homogeneous in PP-R2. Also the content differs significantly between PP-R1 and PP-R2, where PP-R2 has a lower content than PP-R1 at each point across the pipe wall. This variation in AO-18 content results from the different content of AOs in the resin. IR bands, which can potentially be used to quantify AO-13 in PP-R are the hydroxyl absorption at 3649 cm^{-1} and the out of plane vibration of the aromatic ring at 768 cm^{-1} [75]. However, the simultaneous presence of AO-18 and PS-2 in the compound makes it impossible to quantify AO-13 since those absorptions, which could potentially be used for quantification, overlap. Figure 42 shows the resemblances in the hydroxyl and aromatic absorptions when AO-18, AO-13 and PS-2 are blended individually and as mixture with PP-R.

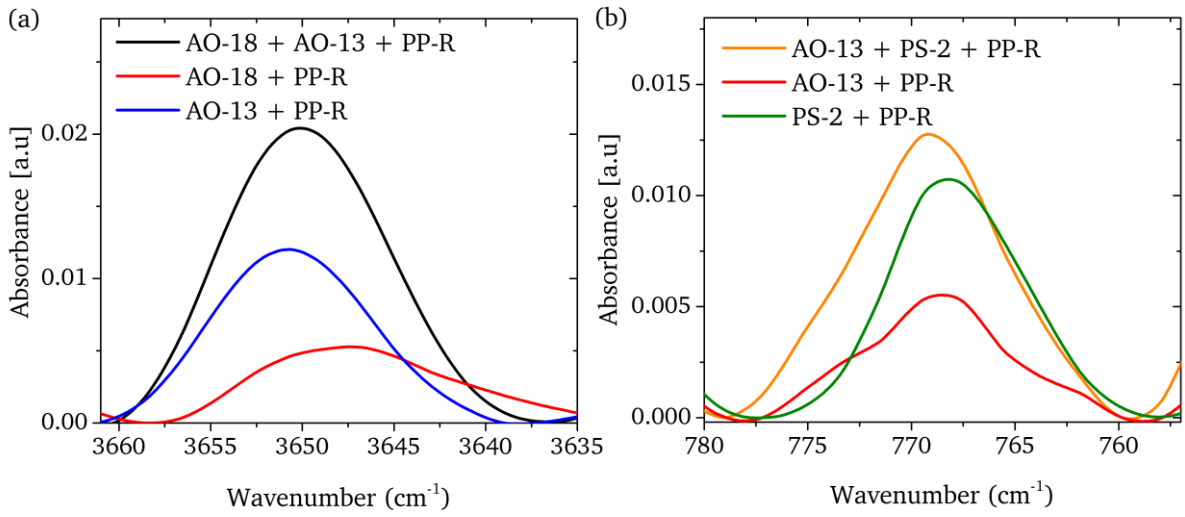

Figure 42: IR spectra showing the absorption of (a) hydroxyl groups in AO-18 and AO-13 at ~3649 cm^{-1} and (b) the aromatic absorption in PS-2 and AO-13 at 768 cm^{-1}.

Hence, a new method to quantify AO-13 has to be developed.

The total absorbance of the band at 3649 cm^{-1} (A_{OH}^{Total}) represents the sum of the hydroxyl absorptions from both AO-18 and AO-13 (eq. 30).

$$A_{OH}^{Total} = A_{OH}^{AO-18} + A_{OH}^{AO-13} \qquad 30$$

Where A_{OH}^{AO-18} and A_{OH}^{AO-13} are the contributions of AO-13 and AO-18 respectively.

To single out the contribution of A_{OH}^{AO-18} to the total absorbance, a set of AO-18 standards with varying AO content in PP-R was studied. The intensity ratio of hydroxyl vs. carbonyl absorption ($A_{OH}^{AO-18}/A_{CO}^{AO-18}$) is a constant given the fact that the number of carbonyl and hydroxyl units in a single molecule of AO-18 is equal (Figure 5). In order to prove the concept, $A_{OH}^{AO-18}/A_{CO}^{AO-18}$ was calculated from standards with varying content of AO-18 in PP-R. The results are presented in Figure 43 and the constant was found as 0.4.

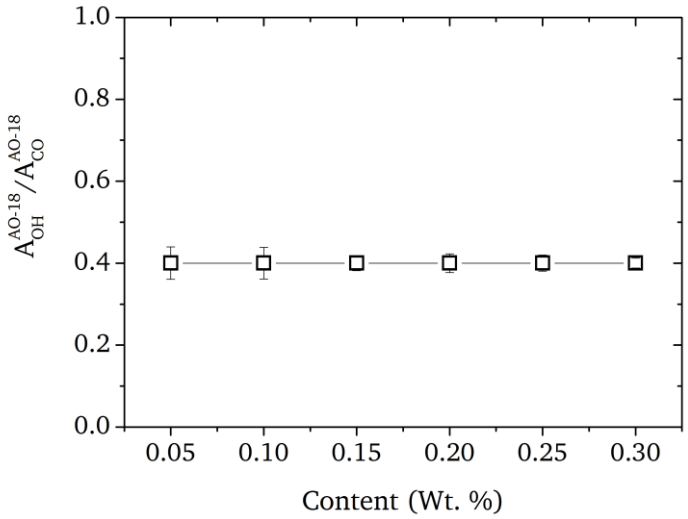

Figure 43: Ratio of carbonyl to hydroxyl absorption at various contents of AO-18 in PP-R.

The final relation connecting A_{OH}^{Total}, the carbonyl absorbance from AO-18, the hydroxyl absorbance from AO-13 and the constant is stated in eq. 31.

$$A_{OH}^{Total} = \text{constant} \times A_{CO}^{AO\text{-}18} + A_{OH}^{AO\text{-}13} \qquad 31$$

A_{OH}^{AO-13} can be calculated from eq. 31, and AO-13 can now be quantified via dividing the hydroxyl absorbance by the product of absorption coefficient (ε) and path length (d). ε of AO-13 is obtained from the calibration curve of AO-13 in PP-R. Figure 44 shows the calibration curve obtained for AO-13 and the distribution of the AO-13 content across the pipe wall.

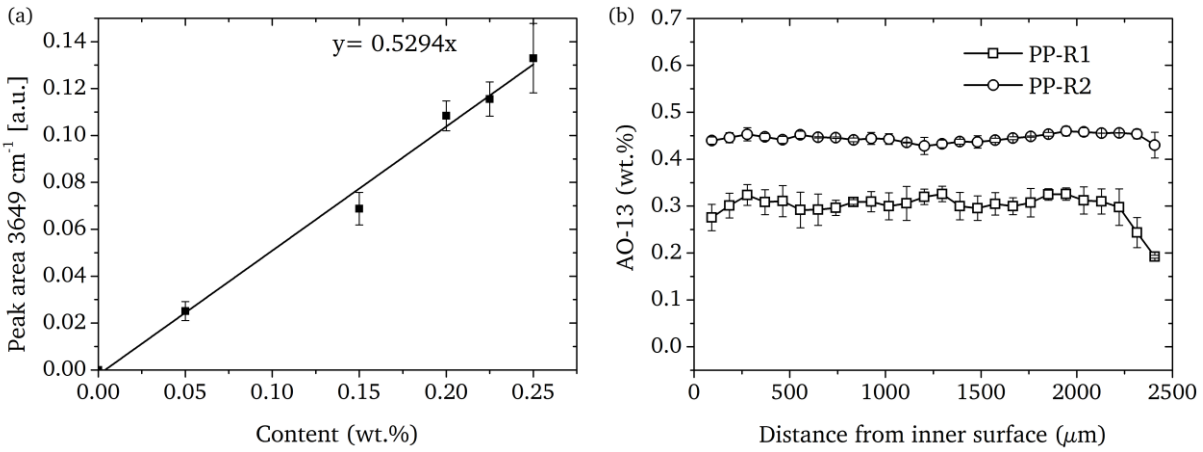

Figure 44: (a) Calibration curve of AO-13 in PP-R using the IR band at 3649 cm^{-1} and (b) distribution of AO-13 in PP-R1 and PP-R2 across the pipe wall.

Generally, the content of AO-13 is higher in PP-R2, which correlates with the results from the HPLC analysis (Table 8). A drop in content towards the outer surface is observed in PP-R1, whereas the AO is homogeneously distributed in the case of PP-R2. These differences in the AO distribution can be attributed to the compounding and processing of pipes. The content of AO-18 and AO-13 in the pipe wall as obtained from averaging the results of μFT-IR across the wall and the results from Extraction→HPLC is summarized in Table 8.

Table 8: AO content obtained by averaging the results from μFT-IR and from Extraction→HPLC across the pipe wall.

Sample	μFT-IR		Extraction→HPLC	
	AO-18 (wt. %)	AO-13 (wt. %)	AO-18 (wt. %)	AO-13 (wt. %)
PP-R1	0.26 ± 0.03	0.31 ± 0.03	0.23 ± 0.01	0.25 ± 0.01
PP-R2	0.16 ± 0.01	0.44 ± 0.01	0.17 ± 0.01	0.43 ± 0.03

PP-R1 and PP-R2 are compounded with AO-18 and AO-13. The quantification results obtained from μFT-IR correlate well with those of Extraction→HPLC. The content of AOs obtained from Extraction→HPLC is slightly lower than that obtained from μFT-IR. A possible explanation might be that the extraction was incomplete or that the AOs degraded to some extent during the extraction step.

7.2.1.4 Orientation of polymer chains in PP-R1 and PP-R2

The orientation of the polymer chains was calculated according to the model described in section 5.2.2. The characteristic IR absorptions of PP at 974 and 998 cm^{-1} were used for this purpose. Out of the two bands, the one at 974 cm^{-1} is a combined absorption from both the amorphous and crystalline phase and the latter one gives the information of the chain orientation in the crystalline phase. The profile of Hermans orientation function (f) across the wall of PP-R1 and PP-R2 as calculated from the band at 974 cm^{-1} is presented in Figure 45.

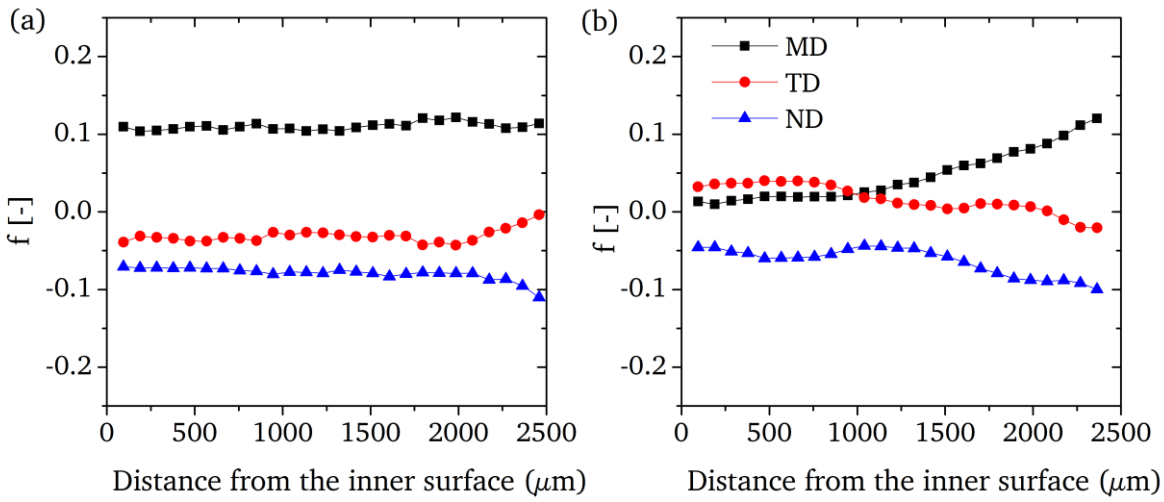

Figure 45: f calculated from the absorption at 974 cm^{-1} for (a) PP-R1 and (b) PP-R2.

The polymer chains across the pipe wall of PP-R1 are oriented along MD with an f value of 0.1, which is almost constant across the pipe wall. However, in the case of PP-R2 the polymer chains at the inner surface are oriented along TD with a lower f value compared to PP-R1. The orientation of the chains in PP-R2 gradually increases along MD towards the outer surface, caused by the quenching experienced during extrusion. This anomalous pattern of chain orientation in the presence of β-nucleating agent has been reported [50, 76]. Schuster et al. [50] found that under the flow of the melt during the extrusion β-nucleating agents (N,N′-dicyclohexyl-2,6-naphthalenedicarboxamide) can crystallize in form of needles with a particular aspect ratio. These needles will orient along the flow direction. This peculiar crystallization behavior of a β-nucleating agent could not be experimentally verified here as the material was coloured, which prevented the necessary PLM analysis. Nevertheless this may help to explain the findings: Instead of a spherical nucleation center from which the polymer chains can grow along all directions, in this case the polymer chains crystallize epitaxially on the lateral planes of the needle of the nucleating agent [26]. The volume of polymer chains growing perpendicular to the nucleating agent is now highly dependent on the aspect ratio of the nucleating agent. A needle of nucleating agent with high aspect ratio leads to a higher fraction of polymer chains perpendicular to it and hence, a higher f value along TD. A schematic representation of the epitaxial formation of polymer chains perpendicular to the needle and the influence of aspect ratio of the needle on the f value of polymer chains is depicted in Figure 46.

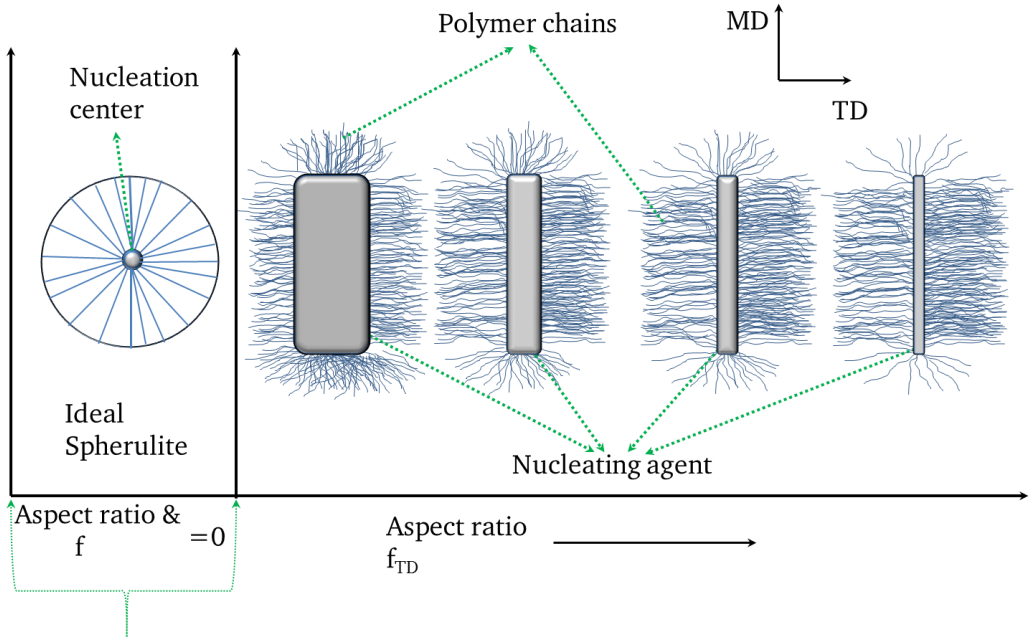

Figure 46: schematic representation of the influence of the aspect ratio of the needle on the orientation of the polymer chains

Analogously, the orientation of PP chains as calculated from the absorption at 998 cm^{-1} is presented in Figure 47.

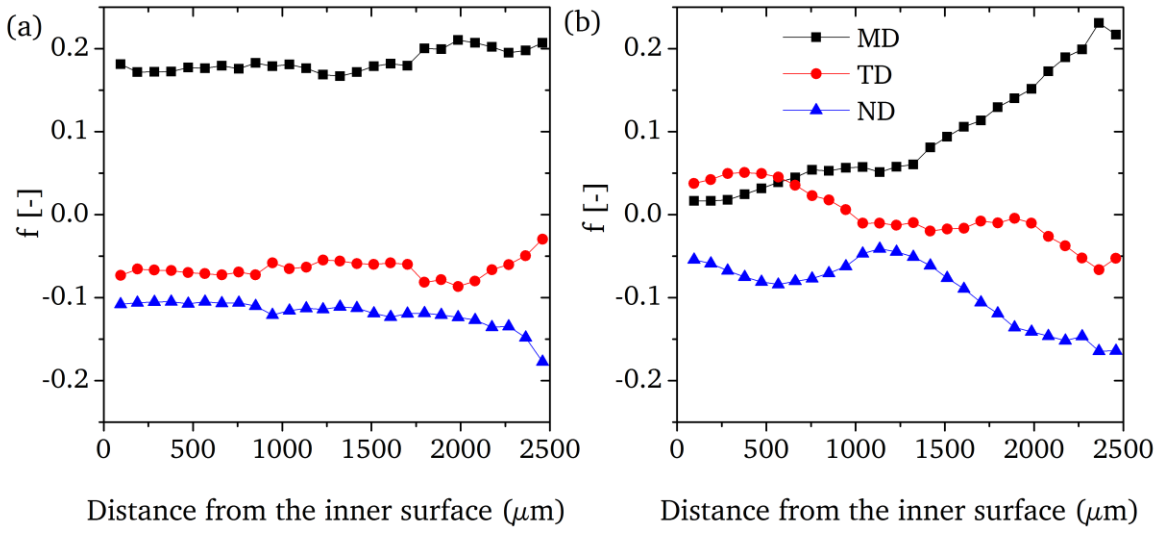

Figure 47: f calculated from the absorption at 998 cm^{-1} for (a) PP-R1 and (b) PP-R2.

The chains are consistently oriented along MD across the pipe wall of PP-R1 (Figure 47 a). Since crystallization is the only mechanism of arranging the polymer chains in pipes in the absence of any mechanical forces after extrusion, the observed result (Figure 47 a) indicates that the crystallization rate along the wall thickness was constant. However, in the case of PP-R2 the orientation of polymer chains at the inner surface is slightly along TD which, then, changed to MD towards the outer surface

(Figure 47 b). Moreover, at low crystallization rates β-nucleation will takes place effectively which, however, highly depends on the crystallization temperature as well. Consequently, the polymer chains will be oriented along TD, whereas high crystallization rates result in the freezing of the incurred chain alignment and thus the chain orientation along MD.

7.2.1.5 Size exclusion chromatography

The MMD of the samples PP-R1 and PP-R2 is presented in Figure 48 and the corresponding average molar masses are listed in Table 5.

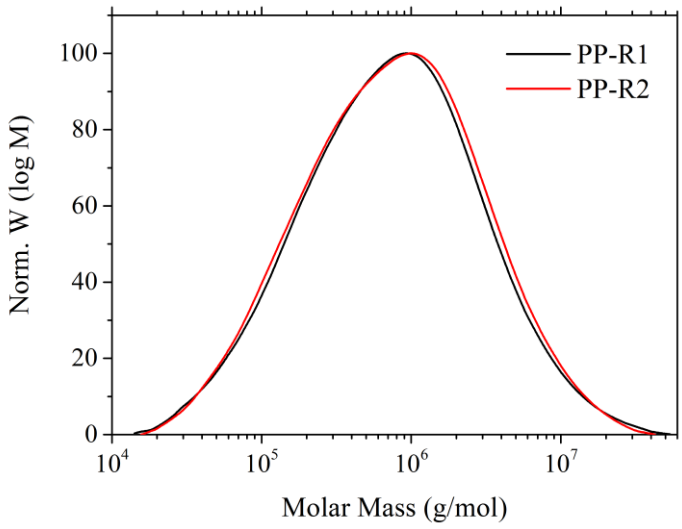

Figure 48: MMD of PP-R1 and PP-R2.

Table 9: Average molar masses determined for PP-R1 and PP-R2.

Sample	M_w (x 10^6 g/mol)	Dispersity index
PP-R1	1.2	6
PP-R2	1.2	6

The average molar masses of PP-R1 and PP-R2 can be found the same.

7.2.2 Ageing of pipes with chlorinated hot water as inner medium

The influence of chlorinated water on the degradation of PP and AOs was first elucidated for the samples aged at 95 °C and a chlorine concentration of 4 mg/L. The mechanism of AO loss, determination of AO loss coefficients, and reduction in average molar mass will be explained in this chapter.

7.2.2.1 Infrared microscopy

PP-R1 and PP-R2 were exposed to chlorinated water as explained in the experimental section, yielding the samples PP-R1$_{Cl}$ and PP-R2$_{Cl}$. μFT-IR analysis was performed across the wall of samples taken after varied ageing times. Functional groups that consist of carbonyl moieties are the principle degradation products when PP is in contact with oxidatively deteriorating environments (section 3.3). Hence, IR spectra in the carbonyl region formed at the inner wall section of 100 μm of PP-R1$_{Cl}$ and PP-R2$_{Cl}$ are shown in Figure 49.

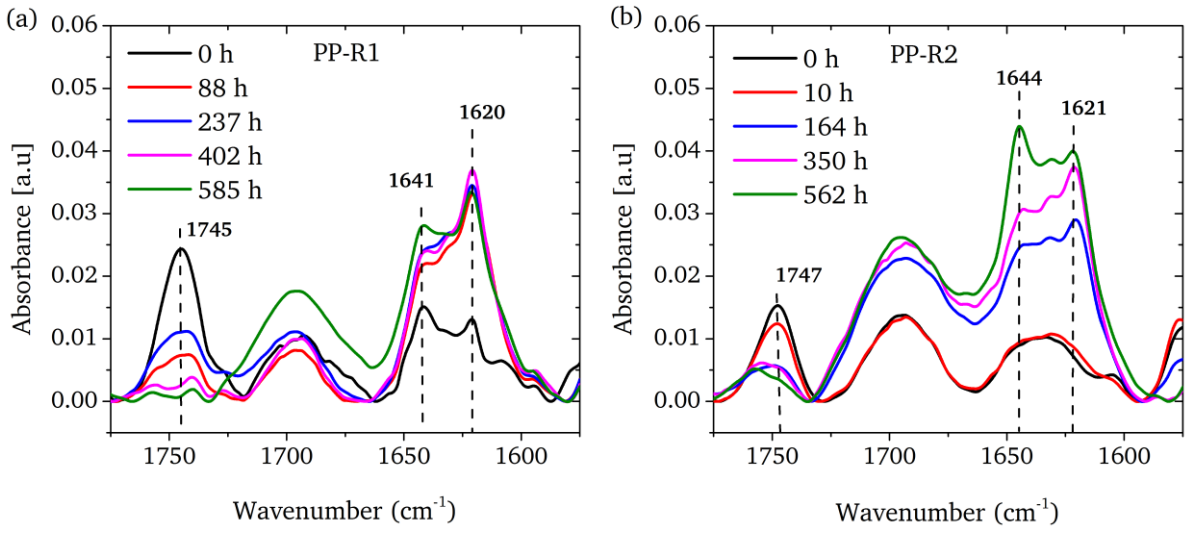

Figure 49: IR spectra of (a) PP-R1$_{Cl}$ and (b) PP-R2$_{Cl}$ taken 100 µm from the inside of the pipe.

It can be recognized that the bands at 1745, 1641 and 1620 cm^{-1} vary in intensity with ageing time. The bands at 1641 and 1620 cm^{-1} increase their intensity with time, which can be explained by the formation of an additional absorbing moiety. The band at 1745 cm^{-1} decreases in intensity with ageing time, which reflects the loss of AO-18 for pipes made from both grades of PP. The content of AO-18 calculated as described in section 7.2.1.2 across the pipe wall for PP-R1$_{Cl}$ and PP-R2$_{Cl}$ aged for different times is presented in Figure 50.

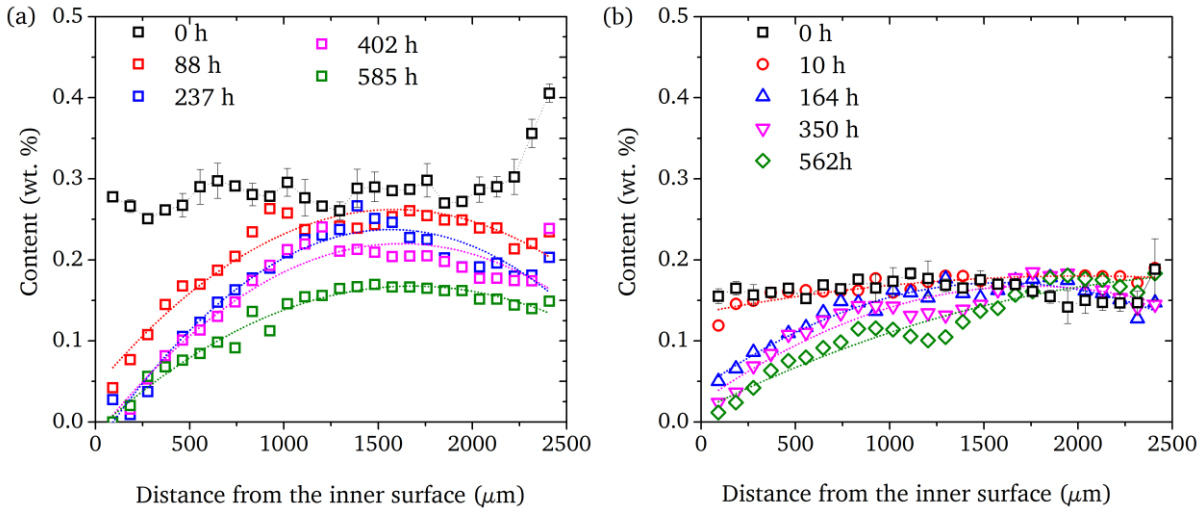

Figure 50: Distribution of AO-18 across the pipe wall of (a) PP-R1$_{Cl}$ (b) PP-R2$_{Cl}$.

In general, a loss of AO is observed at the inner surface of both pipes. However, the AO-18 loss at the outer surface differs significantly between PP-R1$_{Cl}$ and PP-R2$_{Cl}$. PP-R1$_{Cl}$ depicts an accelerated drop in AO-18 content at the outer surface, which is considerably less in PP-R2$_{Cl}$. To compare the rate of AO loss it is necessary to normalize their contents because PP-R1 and PP-R2 differ in their initial content. Consequently, the variation of the AOs relative content (C/C_0) across the pipe wall with ageing time as determined from the carbonyl band is presented as color coded contour plot in Figure 51 for PP-R1$_{Cl}$ and PP-R2$_{Cl}$, where C_0 was taken as the average across the wall of the respective unaged specimen.

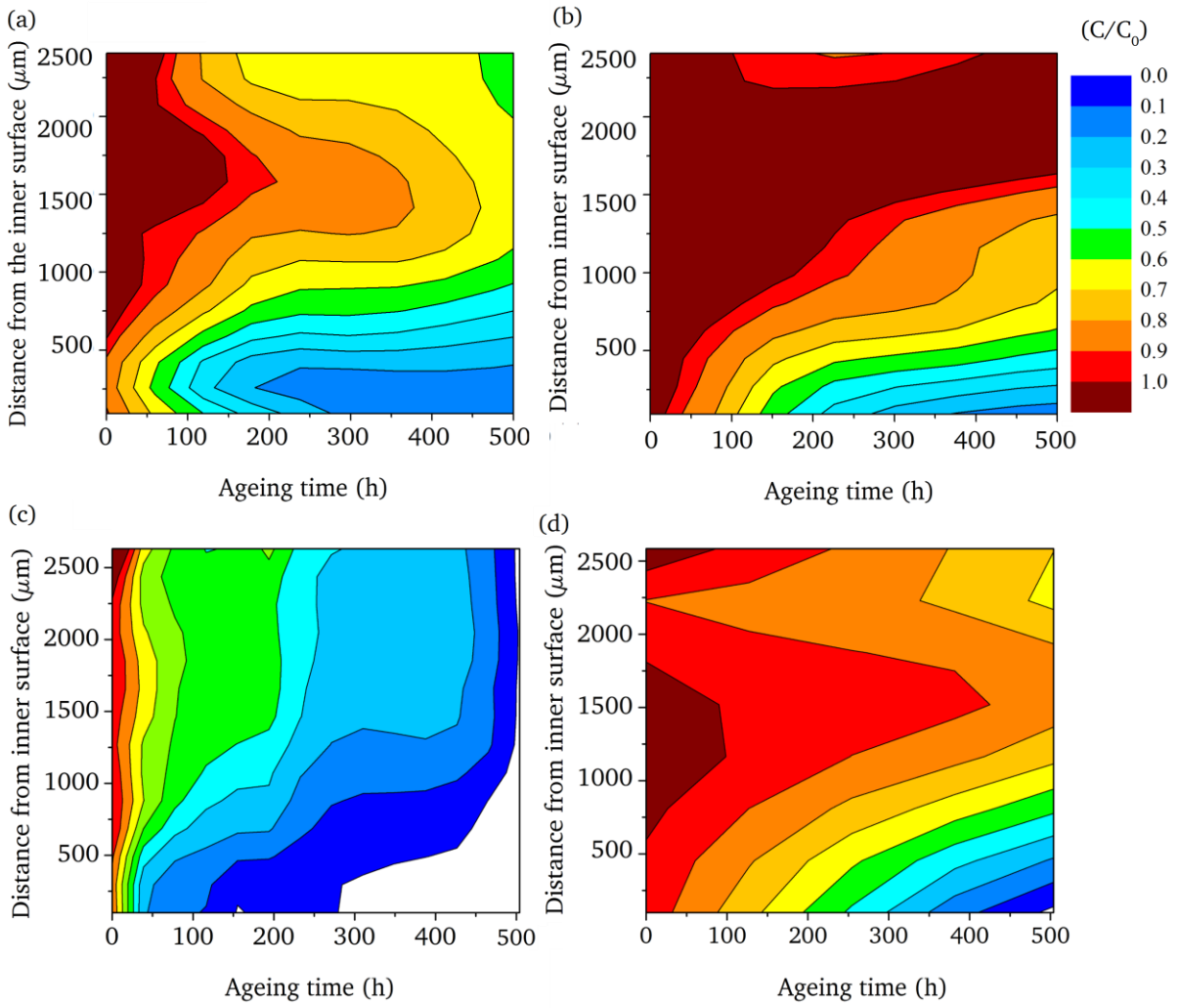

Figure 51: Time and space resolved contour plots for C/C_0 of AO-18 for (a) PP-R1$_{Cl}$ (b) PP-R2$_{Cl}$ aged at 95 °C and (c) PP-R1$_{Cl}$ (d) PP-R2$_{Cl}$ aged at 110 °C.

The loss of AO-18 in PP-R1$_{Cl}$ and PP-R2$_{Cl}$ occurs mainly from the inner surface during the early phase of ageing (Figure 51), while with progressing time the loss in PP-R1$_{Cl}$ from the outer surface becomes significantly higher (at both 95 °C and 110 °C) than in PP-R2$_{Cl}$. Comparing the AO-18 content remaining in the pipes after 500 h (at 110 °C, Figure 51 c and d) it can be seen that AO-18 from the inner surface of PP-R1$_{Cl}$ (until ~1000 μm) is completely dissipated, while PP-R2$_{Cl}$ is still satisfactorily stabilized with AO-18. Three different mechanisms of AO loss have to be considered for pipes in contact with water [77].

1. Functioning as stabilizer by capturing radicals in the polymer
2. Extraction to the surrounding media
3. Direct reaction with oxygen

The bilateral nature of the AO-18 loss in PP-R1$_{Cl}$ is the result of the chemical consumption or extraction from the inner surface and the sublimation or chemical consumption from the outer surface [78, 79]. Hydrolysis is a well known degradation mechanism (Scheme 1) for AO-18 where the reaction proceeds through successive nucleophilic attack of a water molecule at the carbonyl carbon atom of the ester groups, ultimately leading to the formation of 3-(3,5-ditert-butyl-4-hydroxy-phenyl) propanoic acid and pentaerythritol [80].

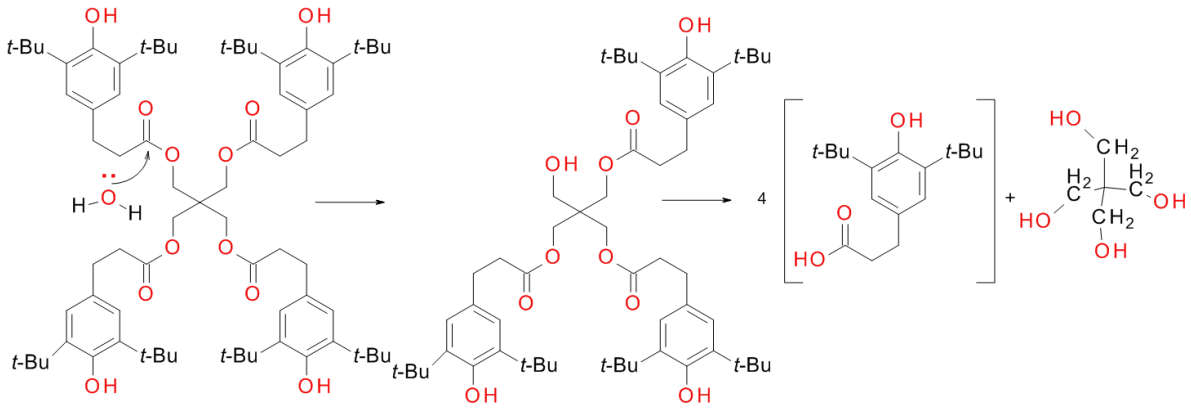

Scheme 1: Degradation mechanism of AO-18 by hydrolysis [80].

A band centered at 3632 cm^{-1} in the IR spectra can be assigned to the absorption of carboxylic hydroxyl groups [81] from 3-(3,5-ditert-butyl-4-hydroxy-phenyl) propanoic acid. The IR spectra of PP-R1$_{Cl}$ in the hydroxyl region at a depth of 100 μm from the inner surface of the pipe are presented in Figure 52, where the inset shows the formation of the band at 3632 cm^{-1} with ageing time.

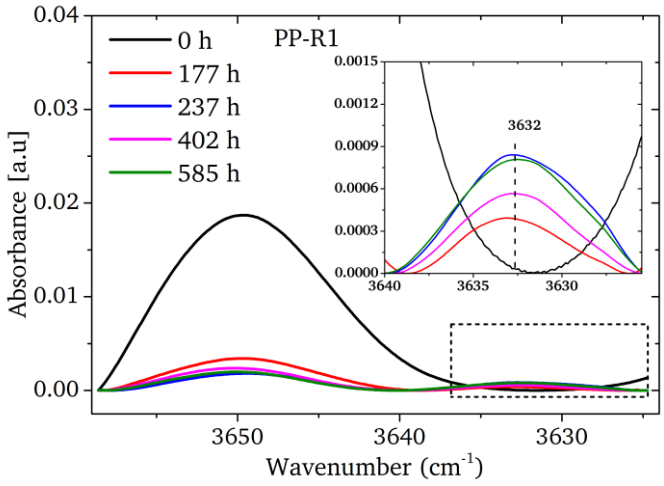

Figure 52: Hydroxyl region of the IR-spectra of PP-R1$_{Cl}$.

The band intensity does not linearly increase with ageing time, which suggests that the carboxylic group containing species undergo further reactions or are extracted from the pipe [82]. The distribution of the intensity of the band across the pipe wall is shown as contour plot in Figure 53.

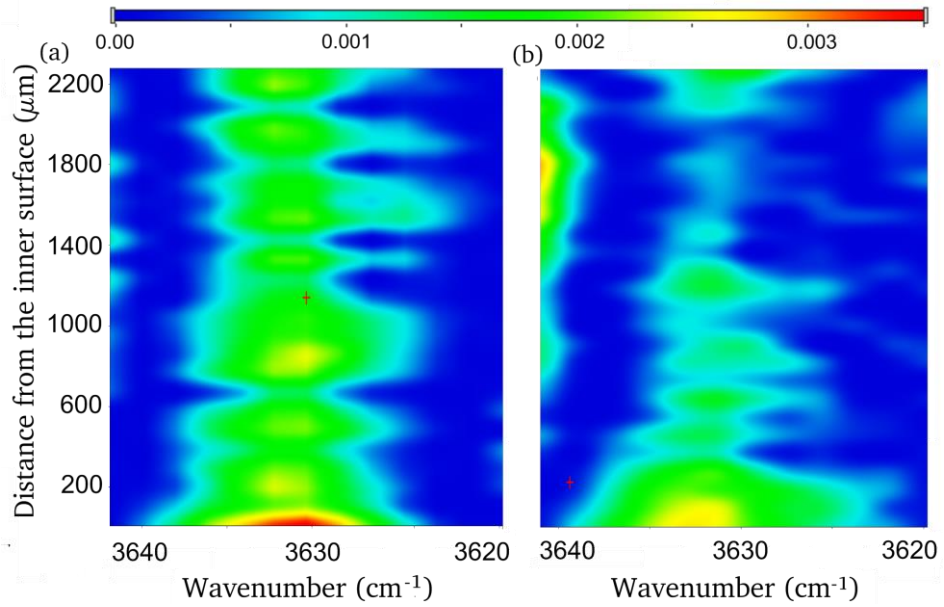

Figure 53: Contour plots obtained from μFT-IR for the vibration at 3632 cm^{-1} (a) PP-$R1_{Cl}$ (585 h) and (b) PP-$R2_{Cl}$ (562 h).

The contour plots (Figure 53) show that the IR absorption of AO-18 degradation products in PP-$R1_{Cl}$ is comparatively intense across the pipe wall, whereas in the case of PP-$R2_{Cl}$ the absorption is strong mainly at the inner surface. This clearly proves that the hydrolysis of AO-18 is locally heterogeneous in nature.

The C/C_0 of AO-13 with ageing time was calculated using the method described in section 7.2.1.2 and is presented as color coded contour plot in Figure 54 for PP-$R1_{Cl}$ and PP-$R2_{Cl}$.

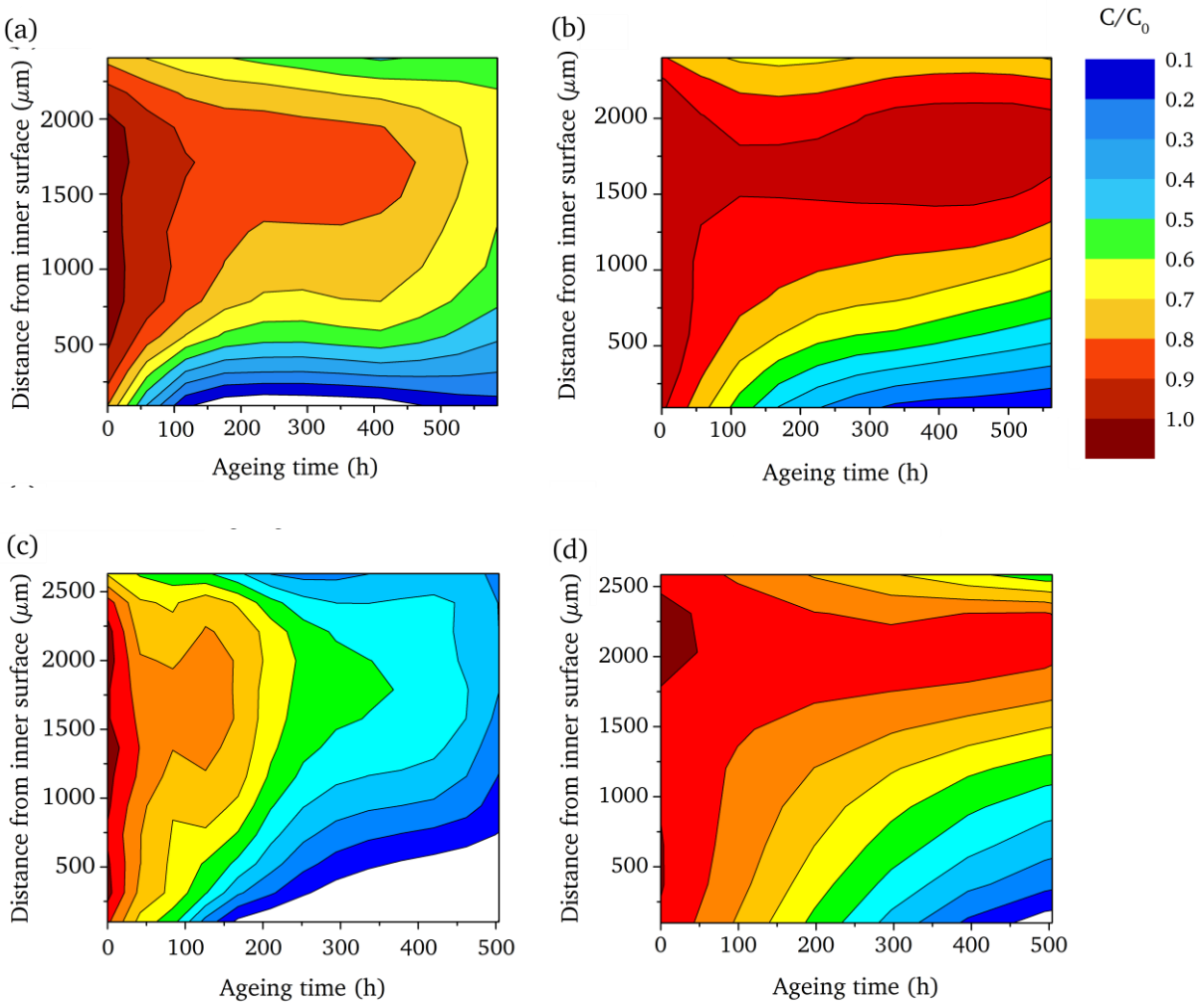

Figure 54: Time and space resolved contour plots showing the variation in C/C_0 of AO-13 with ageing time (a) PP-R1$_{Cl}$ and (b) PP-R2$_{Cl}$ at 95 °C (c) PP-R1$_{Cl}$ and (b) PP-R2$_{Cl}$ at110 °C.

The C/C_0 of AO-13 in PP-R1$_{Cl}$ (Figure 54 a) decreases with ageing time from both surfaces of the pipe wall at a higher rate compared to PP-R2$_{Cl}$. However, unlike in the case of AO-18, the loss of AO-13 occurs in both samples even during the initial hours of ageing from the outside, where the pipes are in contact with air. The degradation of AO-13 proceeds stepwise via quinones [83, 84], which can be well recognized from the bands at 1644 cm^{-1} and 1620 cm^{-1} (Figure 49) being characteristic for conjugated C=C [85, 86] and ketone [87] groups, respectively. The reported mechanism for the oxidation of phenolic groups to quinones is presented in scheme 2.

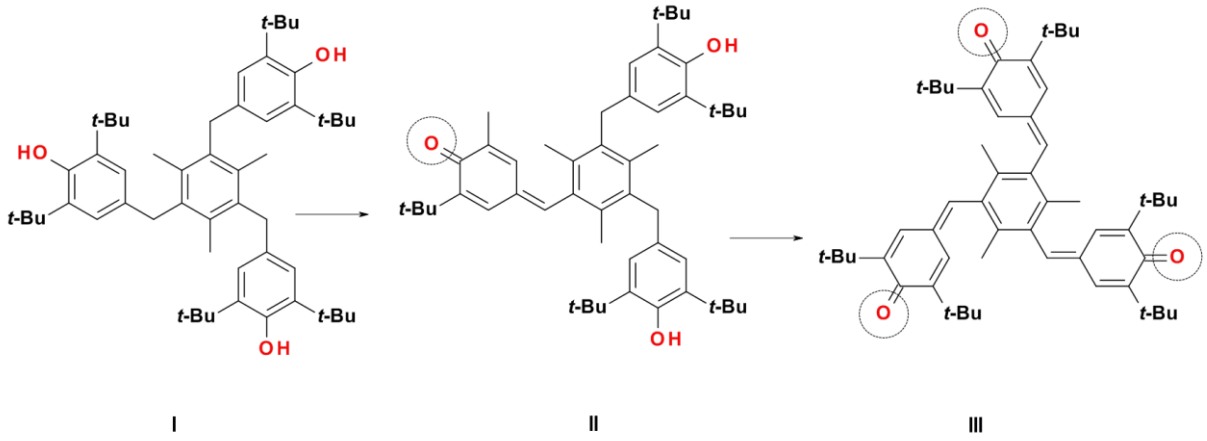

Scheme 2: Formation of quinones during the oxidation of AO-13.

The degradation of AO-13 proceeds via donating the phenolic hydrogen to peroxide radicals formed as a result of the attack of oxygen on the polymer chain, thereby forming the mono quinone (Scheme 2.II). Subsequently, the other hydroxyl groups of AO-13 are oxidized in the same manner to form the fully conjugated trisquinone (Scheme 2.III). The content of quinones formed was quantitatively determined by Extraction→HPLC as described in section 6.6 for specimen mechanically prepared from the pipe wall. The results obtained for the mono, di, and tri quinone and the AO-13 remaining in the pipe wall of PP-R1$_{Cl}$ after 585 h of ageing are presented in Figure 55.

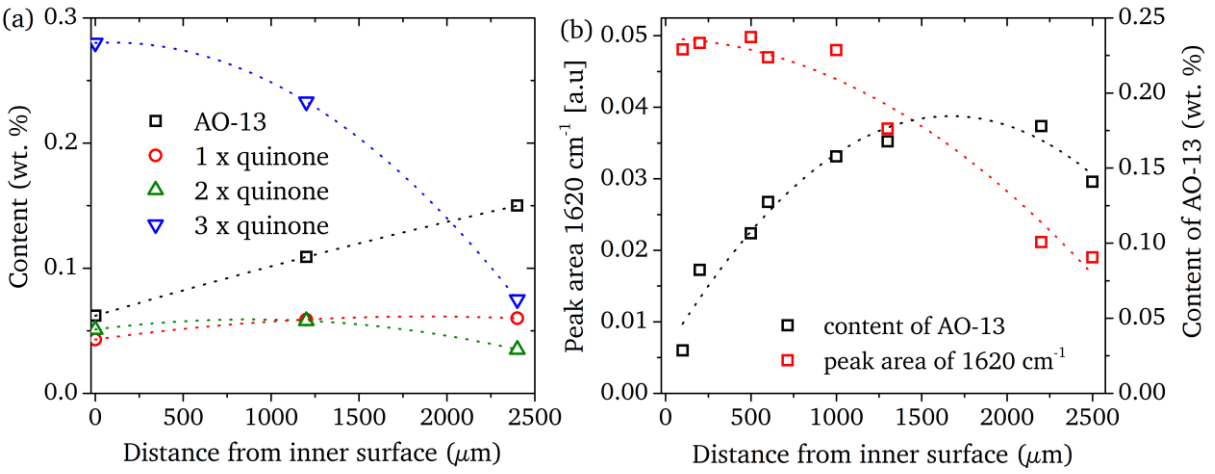

Figure 55: PP-R1$_{Cl}$ (585 h) (a) Distribution of quinones and the remaining AO-13 as determined by Extraction→HPLC and (b) Distribution of AO-13 and the area of the band at 1620 cm^{-1} obtained from μFT-IR.

From Figure 55 a it can be concluded that the content of quinones is higher at the inner surface of the pipe wall and that the content of AO-13 remaining in the wall displays a gradient from the inner to the outer surface. Figure 55 b shows the distribution of the area of the band at 1620 cm^{-1} and the absolute content of AO-13 remaining in the pipe wall. The absorption coefficient of the band at 1620 cm^{-1} is required to determine the absolute content of quinone which, however, cannot be derived from μFT-IR. Additionally, the precise position of the band characteristic for the mono, di and tri quinone in the IR spectrum is unknown. However, if μFT-IR analysis is performed in transmission mode with a constant sample thickness, then the absorbance of the band at 1620 cm^{-1} will be proportional to the content of all quinones. The distribution of the intensity of the bands at 1640 and 1620 cm^{-1} is presented as contour plot in Figure 56.

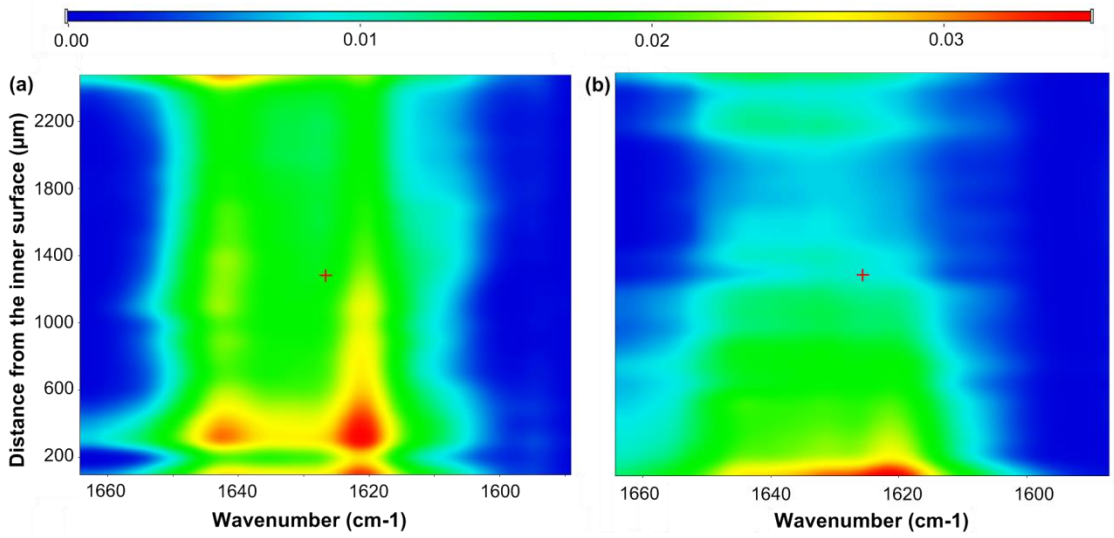

Figure 56: Distribution of the intensity of the absorptions C=C (at 1640 cm^{-1}) and C=O (at 1620 cm^{-1}) from quinones across the wall of (a) PP-R1$_{Cl}$ (585 h) and (b) PP-R2$_{Cl}$ (562 h).

The intensity of the absorptions at 1640 and 1620 cm^{-1} from quinones shows an increase from the inner surface of PP-R1$_{Cl}$ and PP-R2$_{Cl}$, which validates the results from Extraction→HPLC (Figure 55 a). From the comparison of an ageing time above 500 h (Figure 54 - Figure 56) it can be concluded that the formation of quinones coincides with the loss of AO-13. It has been reported that the conjugated quinone structures formed upon oxidation of AO-13 are highly susceptible to further degradation in the presence of chlorinated water [88]. In order to investigate this fact, the area of the band at 1620 cm^{-1} taken at 100 μm from the inner surface is presented as a function of ageing time in Figure 57.

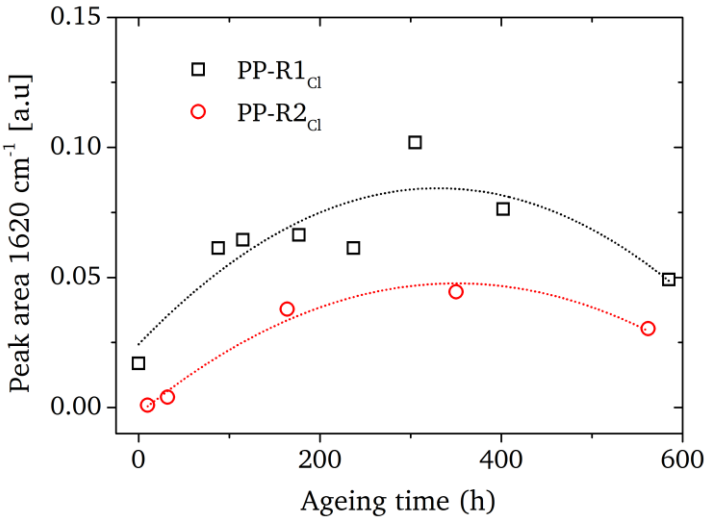

Figure 57: Variation of the peak area at 1620 cm^{-1} (at 100 µm from the inner surface) with ageing time.

Figure 57 shows that with lower ageing time the area of the peak at 1620 cm^{-1} increases and then decreases after passing a maximum. This indicates that the quinones, formed by the oxidation of AO-13, either undergo further reactions or are extracted from the pipe wall into the inner and outer medium.

The diffusion of small molecules, such as AOs or their degradation products, from polyolefin pipes to the inner medium has been investigated [89-91]. A method has been previously described to determine the diffusion coefficient of AO-18 from PP-R pipes by using μFT-IR, which relies on the presence or absence of an absorption specific for AO-18 at 1744 cm^{-1} [75]. The diffusion of small molecules in semicrystalline polymers occurs through the amorphous phase and can be described by Fick's first law (eq. 32) under the assumption that the diffusion coefficient through the pipe wall is constant [92].

$$F = -D' \frac{\partial c}{\partial x} \qquad 32$$

where F is the diffusion flux, D′ is the diffusion constant, c the concentration of diffusant and x is the position.

In the case of a hollow cylinder, Crank [93] formulated a mathematical expression for calculating the diffusion with an initial concentration C_0 and a zero concentration of diffusant in the medium at the inner and outer surface as eq. 33 [94].

$$\frac{c_t}{c_0} = \frac{4}{b^2 - a^2} \sum_{n=1}^{\infty} \frac{J_0(a\alpha_n) - J_0(b\alpha_n)}{\alpha_n^2 \{J_0(a\alpha_n) + (J_0(b\alpha_n)\}} e^{-D'\alpha_n^2 t} \quad 33$$

Where c_t -concentration at time t, a- inner radius, b- outer radius,

J_0 -Bessel functions of first kind and zero order [95]

$$J_0(x) = \sum_{m=0}^{\infty} \frac{(-1)^m}{\Gamma(m+1)m!} \left(\frac{x}{2}\right)^{2m} \quad 34$$

Where m – integer, $\Gamma(z)$ - gamma function, α_n in eq. 33- n^{th} positive root of $J_0(x)$

The least square fitting of eq. 33 to the measured contents of AO averaged across the pipe wall yields the value for D′. According to eq. 33, D′ is the diffusion constant of the diffusant of initial concentration C_0. However, the presence or absence of AO bands or a variation in band intensity cannot be considered solely as the consequence of diffusion. The decrease in the intensity of AO bands is the cumulative result of the pathways degradation and diffusion and therefore, D′ determined using eq. 33 can be regarded as the coefficient of AO loss.

In order to compare the rate of AO loss, D′ was calculated for AO-18 and AO-13 as described previously [75] in which C/C_0 is the theoretically calculated for a D′ value being fitted with the C/C_0 averaged across the pipe wall ($\overline{C/C_0}$) as obtained from μFT-IR with respect to ageing time. The variations in $\overline{C/C_0}$ of AO-18 and AO-13 in PP-$R1_{Cl}$ and PP-$R2_{Cl}$ with ageing time calculated from μFT-IR and via the theoretical approach are presented in Figure 58.

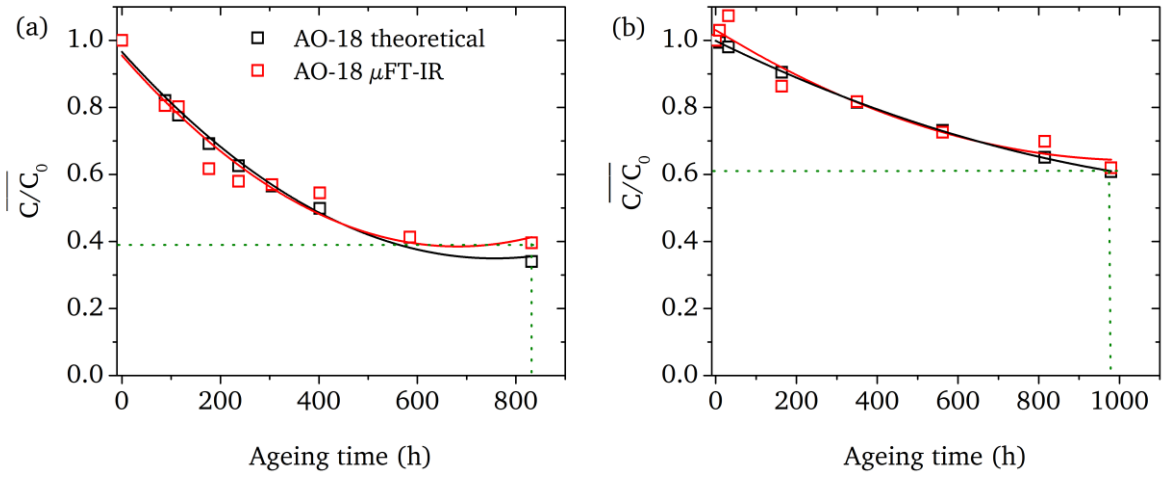

Figure 58: Correlation between $\overline{C/C_0}$ of AO-18 and ageing time obtained by μFT-IR and theoretical calculations for (a) PP-$R1_{Cl}$ and (b) PP-$R2_{Cl}$.

Figure 58 shows that the content of AO-18 in both PP-R1$_{Cl}$ and PP-R2$_{Cl}$ calculated from μFT-IR analysis decreases with ageing time. However, the $\overline{C/C_0}$ value for the highest ageing time of 850 h for PP-R1$_{Cl}$ and 1000 h for PP-R2$_{Cl}$ explains that the depletion of AO-18 in PP-R2$_{Cl}$ progresses slower compared to PP-R1$_{Cl}$. Analogously, the variation of the $\overline{C/C_0}$ of AO-13 present in PP-R1$_{Cl}$ and PP-R2$_{Cl}$ with ageing time is depicted in Figure 59.

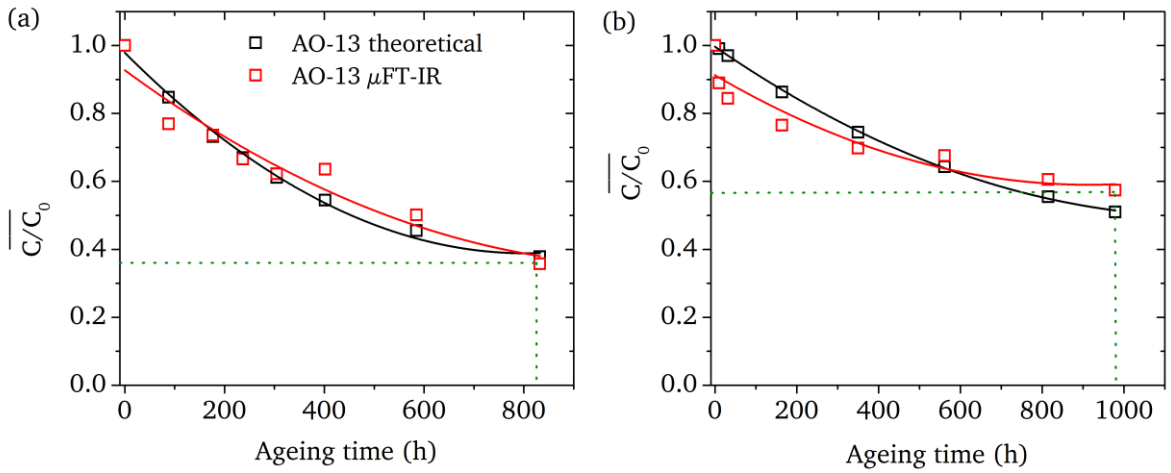

Figure 59: Correlation between $\overline{C/C_0}$ of AO-13 with ageing time and theoretical calculations for (a) PP-R1$_{Cl}$ and (b) PP-R2$_{Cl}$.

The variation in $\overline{C/C_0}$ of AO-13 in Figure 59 shows a similar trend as obtained for AO-18. From the $\overline{C/C_0}$ of AO-13 at the highest ageing time one can clearly interpret that the loss of AO-13 from PP-R2 is slower than that of AO-18. The D′ values calculated by fitting the $\overline{C/C_0}$ (Figure 58 and Figure 59) with ageing time obtained from the theoretical calculations and the μFT-IR results are listed in Table 10.

Table 10: D′ values for AO-18 and AO-13 calculated by fitting the theoretical C/C_0 values with the values obtained from μFT-IR.

Sample	Loss coefficient (D′) x 10^{-9} cm^2/s			
	95 °C		110 °C	
	AO-18	AO-13	AO-18	AO-13
PP-R1$_{Cl}$	2.2	1.9	8	6
PP-R2$_{Cl}$	0.6	0.9	2	1.5

The loss of AO-18 is higher than that of AO-13 at both 95 and 110 °C. During the hydrolysis of AO-18, degradation products of low molar mass and higher polarity than AO-18 are formed [91]. These factors lead to a higher extractability from the pipe wall into the water [80]. The absence of ester groups in AO-13 makes it more adequate for stabilizing PP in water transport applications.

7.2.2.2 Oxidative Induction Time measurements

It has been reported that the OIT of PP stabilized with AO-18 is linearly related to its content [75]. However, the compounds under investigation here make it is necessary to establish the relation between the OIT and the AO content for PP, which is stabilized with more than one AO. Consequently, the OIT values of the standard samples used to calibrate AO-13 for μFT-IR were measured and plotted against the content of AO-13 only and the sum of AO-18 and AO-13 (Figure 60).

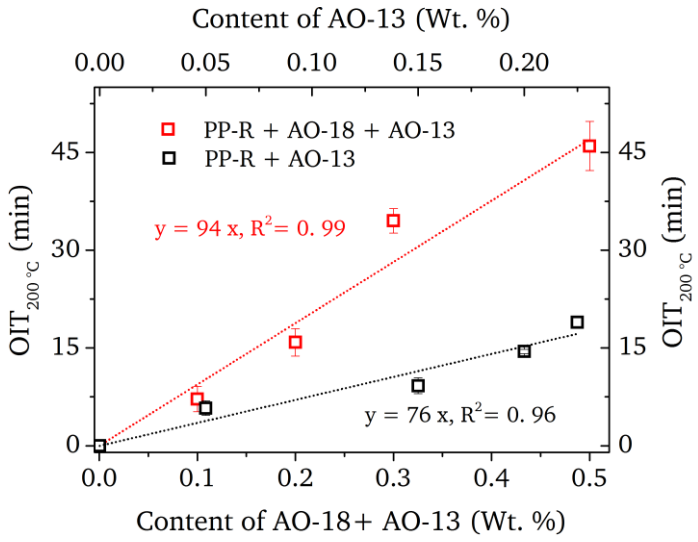

Figure 60: Relation between OIT and the content of AOs.

A linear fitting of the OIT values with their corresponding AO contents in Figure 60 shows that the best result with a correlation coefficient (R^2) of 0.99 is obtained for the relation between the OIT vs. the sum of AO-18 and AO-13. Therefore, it can be concluded that the OIT is a function of the sum of the content of phenolic AOs in the material.

To confirm the results obtained from μFT-IR with a reference technique, OIT measurements were performed on specimen mechanically prepared at different positions across the pipe wall (Figure 61).

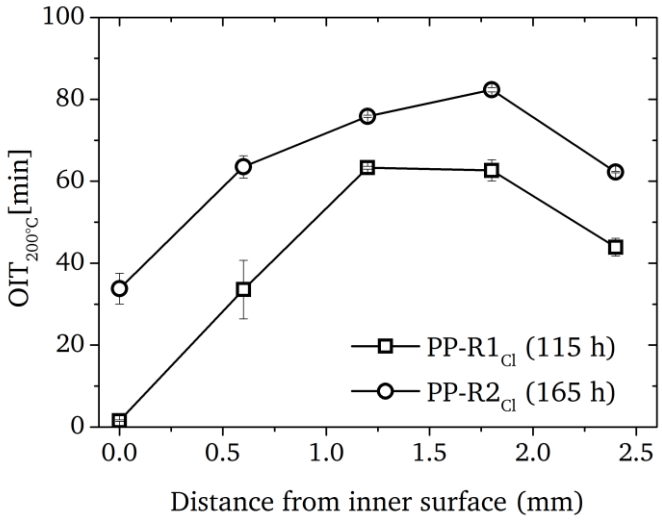

Figure 61: OIT values across the wall of (a) PP-R1$_{Cl}$ (b) PP-R2$_{Cl}$.

The OIT values of PP-R1$_{Cl}$ and PP-R2$_{Cl}$ drop from both surfaces of the pipe wall, being more pronounced towards the inner surface. Moreover, it is evident that the OIT values obtained at equivalent positions of the pipe differ remarkably between PP-R1$_{Cl}$ and PP-R2$_{Cl}$ due to the difference in the initial AO content (Table 8). The variation of OIT values in a layer of 200 μm thickness from the inner surface and the average across the pipe wall of PP-R1$_{Cl}$ and PP-R2$_{Cl}$ were calculated for different ageing times (Figure 62). Due to the difference in the OIT values of the unaged samples, the values presented in Figure 62 were normalized to 100 for comparison.

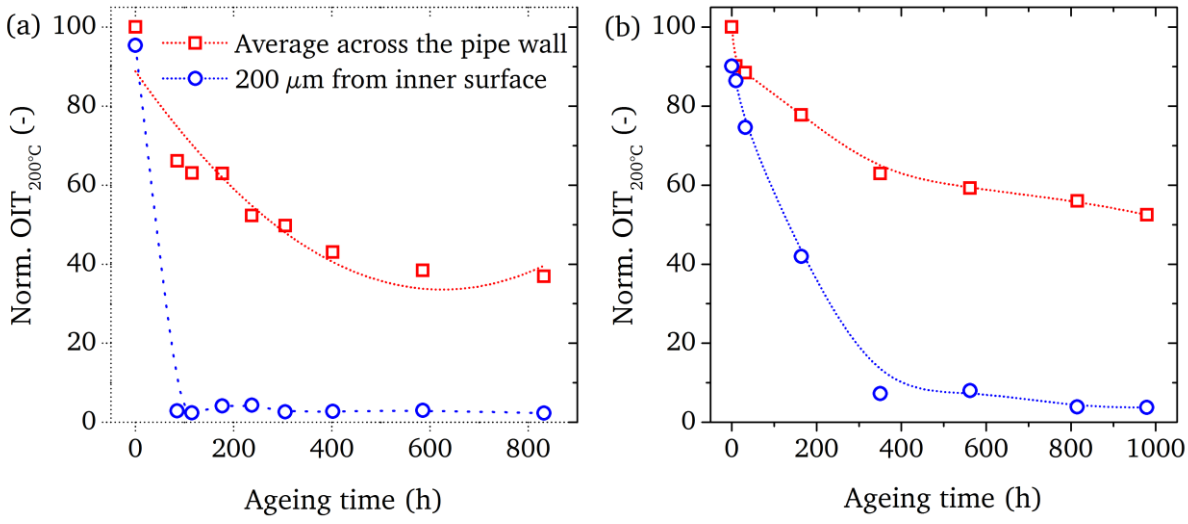

Figure 62: Effect of ageing time on OIT values of (a) PP-R1$_{Cl}$ and (b) PP-R2$_{Cl}$.

A sharp decrease in the OIT values of PP-R1$_{Cl}$ (Figure 62) close to the inner surface, even at short ageing times, is clearly noticeable, and with longer ageing time the OIT

values of PP-R1$_{Cl}$ remain at low values. On the contrary, the OIT values at the inner surface of PP-R2$_{Cl}$ decrease significantly slower with ageing.

OIT measurements were performed on PP-R1$_{Cl}$ and PP-R2$_{Cl}$ aged at 110 °C. Figure 63 compares the OIT profiles of the specimen aged at 95 and 110 °C.

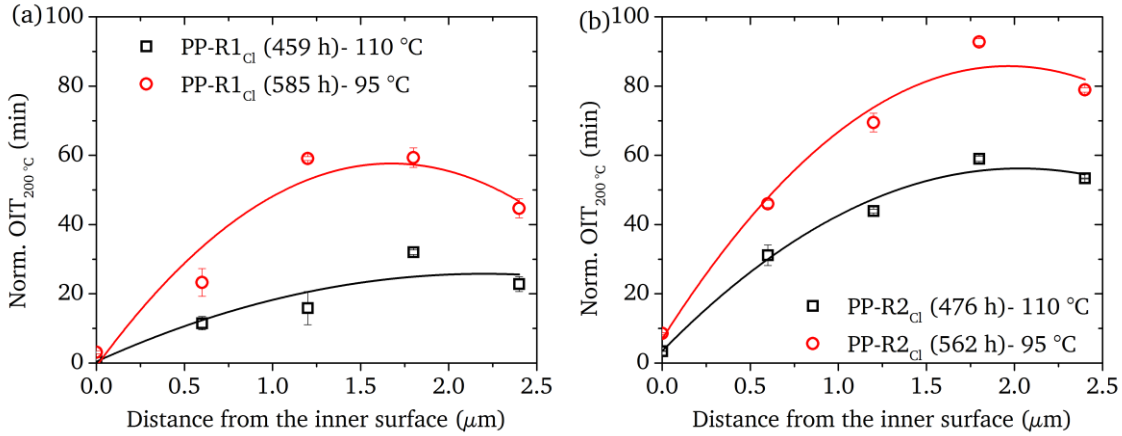

Figure 63: OIT values across the wall of (a) PP-R1$_{Cl}$ and (b) PP-R2$_{Cl}$.

The OIT values of PP-R1$_{Cl}$ and PP-R2$_{Cl}$ aged at 110 °C display an accelerated drop compared to the respective pipes aged at 95 °C. Comparing the OIT values between the pipes it can be seen that at both temperatures PP-R1$_{Cl}$ displays lower values. Correlating the OIT profiles with the AO loss characteristics it can be concluded that the loss of AOs from PP-R1$_{Cl}$ is much more significant than that of PP-R2$_{Cl}$. Time and space resolved OIT values for the pipes aged at different temperatures are presented as contour plots in Figure 64.

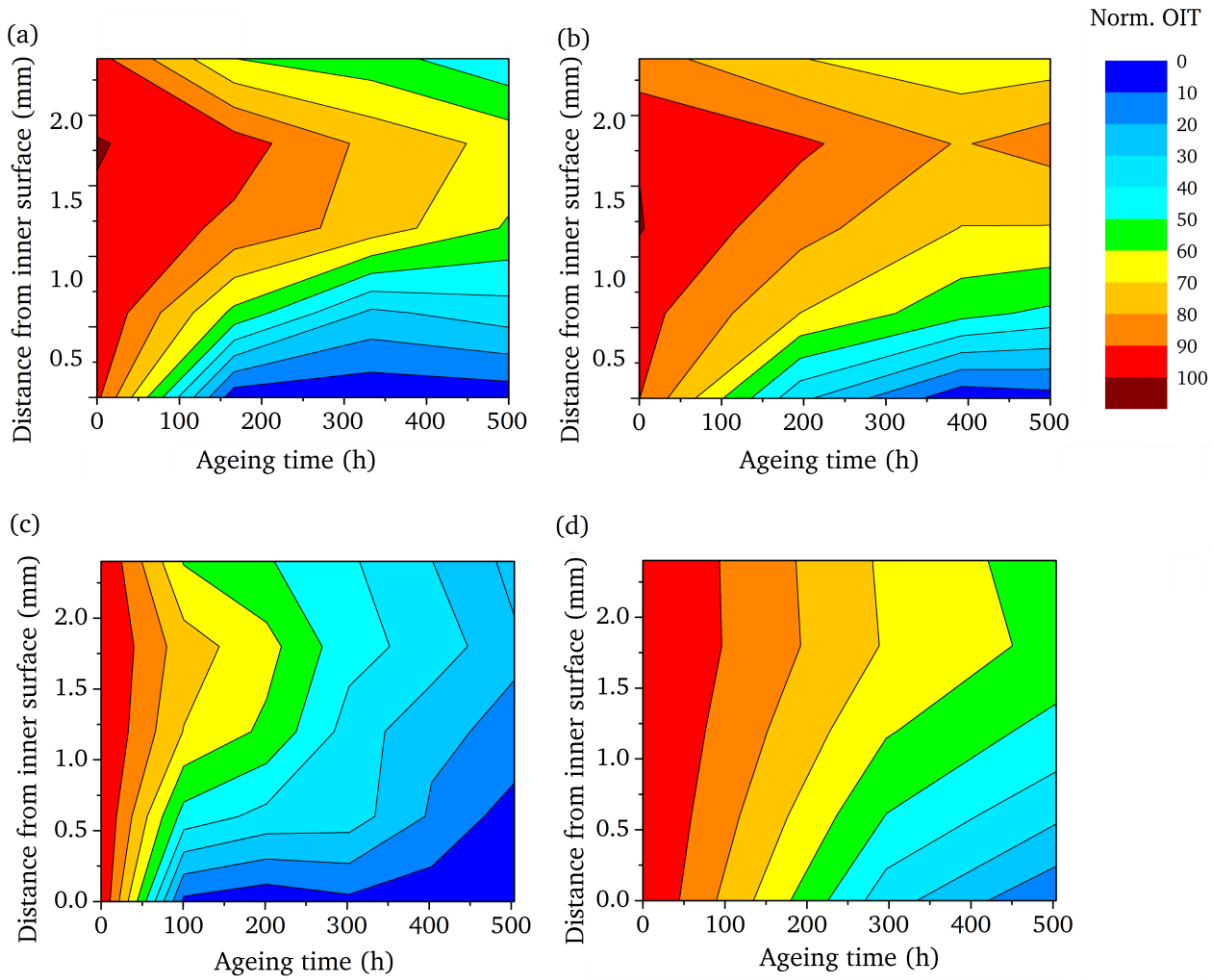

Figure 64: Time and space resolved OIT values of (a) PP-R1Cl and (b) PP-R2Cl at 95 °C (C) PP-R1Cl and (b) PP-R2Cl at 110 °C.

Figure 64 shows that the OIT values decrease from both surfaces, but with a higher rate at the inner surface. However, a comparison of OIT values between the two pipes shows that the bilateral loss rate is lower in PP-R2$_{Cl}$. Additionally, a comparison of the OIT values at 110 °C and 95 °C reveals that the OIT is shorter for the samples aged at 110 °C. These crucial differences in the OIT values between PP-R1 and PP-R2 can be attributed to the differences in AO content in these pipes observed by μFT-IR. The OIT profile presented in Figure 64 is similar to the AO content profiles in Figure 51 and Figure 54.

7.2.2.3 Size exclusion chromatography

The MMD of the polymer at the inner surface (20 μm) of PP-R1$_{Cl}$ and PP-R2$_{Cl}$ was determined by SEC. The MMD as a function of ageing time is depicted in Figure 65.

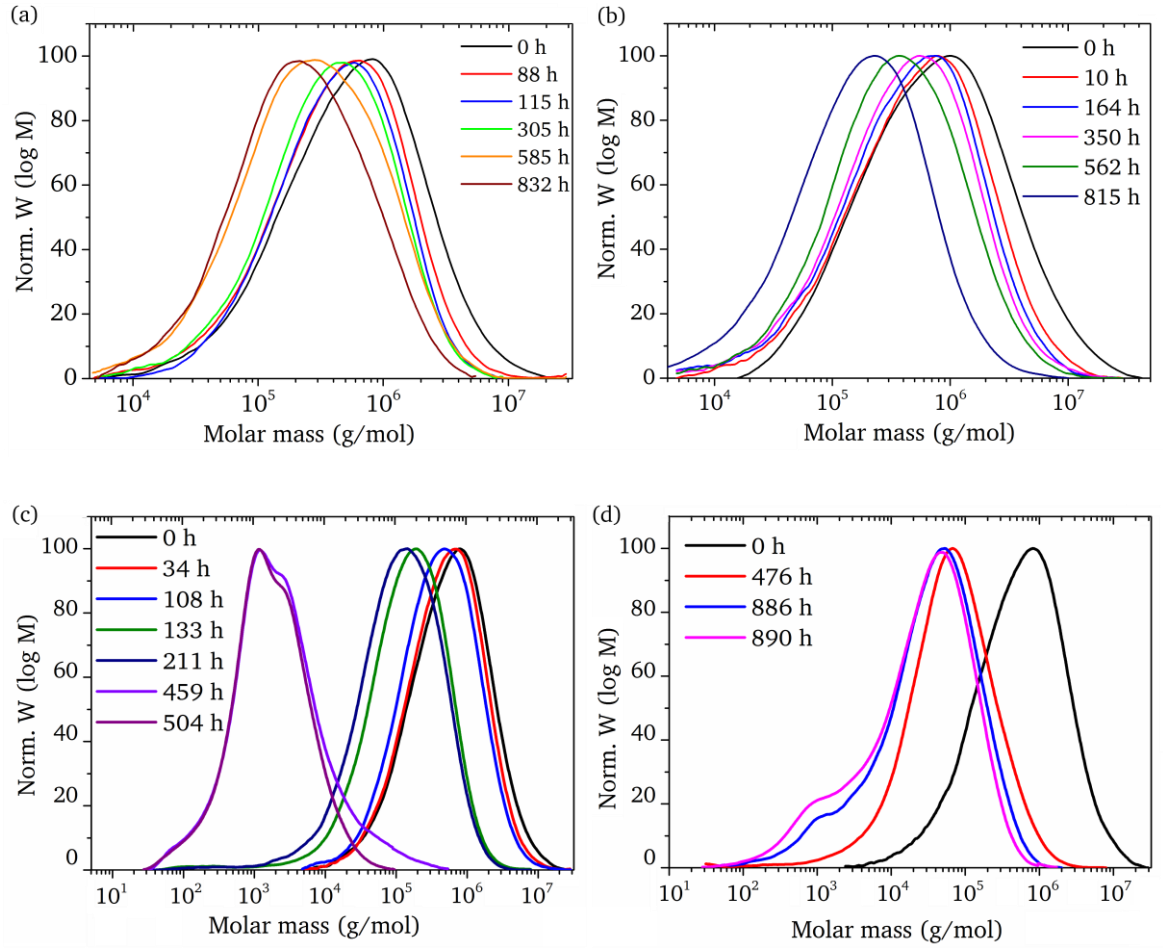

Figure 65: MMD of PP-R1$_{Cl}$ for different ageing times (~20 µm from inside).(a) PP-R1$_{Cl}$, (b) PP-R2$_{Cl}$ at 95 °C and (c) PP-R1$_{Cl}$, PP-R2$_{Cl}$ at 110 °C.

Figure 65 shows a continuous shift of the MMD with time towards the low molar mass region. The calculated values of M_w are plotted as a function of ageing time in Figure 66.

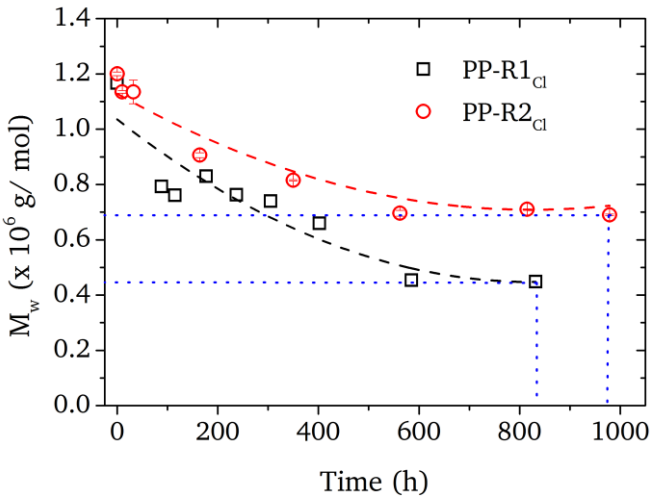

Figure 66: Variation of M_w with ageing time at 95 °C.

The material at the inner surface of both pipes shows significant changes in M_w with ageing time. A similar relation between M_w and ageing time was reported when PP was subjected to thermo-oxidative degradation [96]. However, the rate for the decrease of M_w differs significantly between PP-R1$_{Cl}$ and PP-R2$_{Cl}$, namely M_w of PP-R1$_{Cl}$ decreases faster than that of PP-R2$_{Cl}$. Considering the fact that the degradation of the polymer is the consequence of the loss of protection by AOs, it is important to deduce a relation between the M_w of the polymer and the content of AOs present in the polymer. The variation of M_w as a function of C/C_0 of AO-18 and AO-13 at the inner surface of the pipes was plotted (Figure 67).

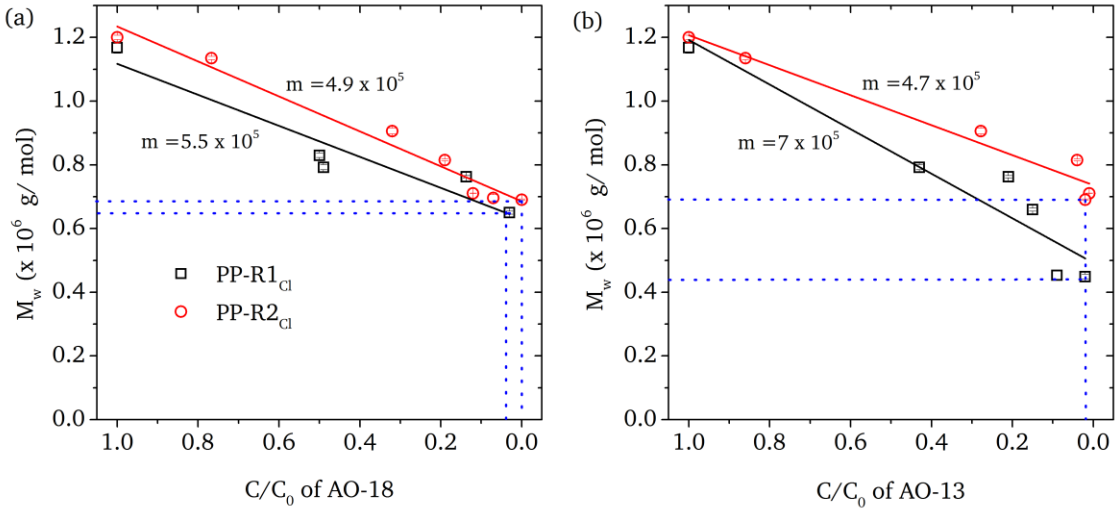

Figure 67: Relation between C/C_0 of AO and M_w at the inner surface (~20 µm) for (a) AO-18 and (b) AO-13 in chlorinated water ageing.

The decrease in M_w depends in a linear way on the content of both AOs, and the sharp decrease in C/C_0 can be recognized for both pipes. However, it can be noticed that the drop in M_w is less steep for PP-R2$_{Cl}$ than for PP-R1$_{Cl}$. In Figure 67 (a) and (b), PP-R2$_{Cl}$ with the lowest content of AO has a higher M_w than PP-R1$_{Cl}$ with the lowest content of AO. Since the degradation rate of AOs depends on the concentration of radicals formed along the polymer chain, these results explain that the amount of radicals formed at the polymer backbone of PP-R1 is greater than PP-R2 and, hence, a faster loss of AOs from PP-R1 is observed. This difference in the rate of AO degradation clearly suggests that the pathway of the degradation differs between PP-R1 and PP-R2. Combining the information that PP-R1 and PP-R2 contain the same AOs with the difference in the degradation kinetics, it can be concluded that the stabilization of the polymer against chlorinated water is not only the consequence of the AOs.

In order to compare the effects of chlorinated water on the M_w the best approach is to compare the slope of the relation between M_w and the C/C_0 of AOs as tabulated in Table 11.

Table 11: Slope of the linear relations in Figure 67.

Sample	Slope of the relation between M_w and	
	AO-18 (x 10^5 g/mol)	AO-13 (x 10^5 g/mol)
PP-$R1_{Cl}$	5.5	7
PP-$R2_{Cl}$	4.9	4.7

The differences in the slope of the trend line (Figure 67) show that the deterioration of PP is more prominent in PP-$R1_{Cl}$ compared to PP-$R2_{Cl}$. Even though the AOs in PP-$R1_{Cl}$ and PP-$R2_{Cl}$ are identical, the rate of degradation differs for both materials under the same ageing condition. Hence, an explanation for the ageing behavior of PP-R1 and PP-R2 needs to include the morphology of the material.

In the case of semicrystalline polymers the diffusion of small molecules depends on the size and shape of the crystallites, X_c, and the orientation of the crystals and polymer chains [97]. AOs in PP are embedded in the amorphous phase [98] due to the rejection of AOs at the growing front during crystallization [99], which prevents the degradation of the amorphous region. The characteristics of the AOs, which control its diffusion are mainly their size, shape and concentration [100, 101]. Previous studies have shown that the diffusivity of AO-18 is very low in polyolefins due to its high molecular weight [102, 103]. Hence, further discussion on the loss of AO activity termed as degradation is carried out.

The degradation of AOs can be either due to the direct reaction of the AO with the chlorinated water or due to reaction with the radicals formed along the polymer chains as a result of contact with chlorinated water. From Figure 67, the M_w of the polymer decreases even in the presence of AOs, which indicates that the consumption of AOs is the result of the stabilizing function i.e., the donation of hydrogen atoms to the macroradicals. However, if the consumption of AO is due to the reaction with only the radicals of the polymer, a similar AO content profile for PP-$R1_{Cl}$ and PP-$R2_{Cl}$ can be expected after a particular ageing time. The ageing conditions were set constant for

both PP-R1 and PP-R2. Additionally, the total wt. % of the AOs (0.6 wt. %) was also a constant for both PP-R1 and PP-R2. Therefore, if the degradation pathways are similar, PP-R1 and PP-R2 have to depict similar rates of AO degradation and molar mass reduction. From Figure 51 and Figure 54, considerable differences in the residence behaviour of AOs were observed between PP-$R1_{Cl}$ and PP-$R2_{Cl}$. Hence, the possibility of alternative pathways for AO loss at places remote from the surface has to be considered, which includes the chain transfer reactions of polymer radicals and the penetration of ageing media through the polymer. In these, chain transfer reactions are independent of the orientation of polymer chains since they can proceed via both intra and intermolecular reactions, while the penetration of the ageing media is influenced by the morphological parameters, such as crystal and chain orientation. All experimental parameters used in ageing (temperature, chlorine concentration, flow rate, oxygen concentration, pH etc.) are constant for both materials. The only difference in the entire ageing process in terms of the ageing parameters and the polymer being the morphology of the material. The amount of radicals formed along the polymer via chain transfer reactions during the contact with chlorinated water should therefore be identical, since the formation of radicals via this mechanism is independent of the morphology of the polymer. Therefore, the amount of AOs degraded by donating hydrogen atoms to these radicals should be same in both pipes. Hence, the difference in the rate of the degradation of AOs and the polymer can be attributed to the second pathway of the formation of radicals i.e., the penetration of the ageing media through the polymer. A detailed discussion on the influence of the penetration of the media with the morphology of the polymer is given below.

The diffusion of small molecules through a spherulite proceeds through the lamellae, which consist of both crystalline and amorphous phases in which the amorphous phase is permeable while the crystalline phase is impermeable due to the dense packing of the chains [97]. Moreover, diffusion is directly proportional to the lamellae thickness due to the higher surface area of the lamellae boundaries [104]. Previous studies on the diffusion of small molecules in PE drawn at different ratios have shown that the diffusion of ethane perpendicular to the chain orientation increased with higher drawing ratios [105-107]. Moreover, the diffusion of small molecules through oriented networks is faster than through randomly oriented ones [108]. Consequently, the penetration of the chlorinated water depends on the morphology of PP, particularly on the thickness of the lamellae and the chain orientation. From the

above discussed facts, the diffusion of small molecules is faster if the polymer chains are aligned in one direction and the diffusion direction is perpendicular to that.

As discussed previously on the morphology of the pipes the orientation of polymer chains in PP-R1 is along MD, while in PP-R2 it is randomly oriented at the inner surface and gradually aligned along MD towards the outer surface (Figure 45 and Figure 47). In the case of pipes the penetration of the inner medium is perpendicular to MD ie., along ND and TD. Hence, from the orientation of polymer chains coupled with the diffusion characteristics the rate of penetration of the ageing media can be higher in PP-R1 than PP-R2. Consequently, the rate of formation of radicals along the chain is larger in PP-R1 and leads to a higher rate of degradation of AOs at places remote to the surfaces of the pipes.

7.2.2.4 Summary

The changes occurring in the wall of PP-R pipes (α-nucleated PP-R1 and β–nucleated PP-R2) upon exposure to chlorinated water (chlorine concentration = 4 mg/L and temperature at 95 and 110 °C) was monitored by μFT-IR, DSC and SEC. From the experimental results the following conclusions can be drawn:

- The content of AOs consistently decreased with time while the increase in intensity of the bands at 3632, 1620 and 1640 cm^{-1} could be attributed to the degradation products of AO-18 and AO-13, respectively.
- Degradation of AOs occurred continuously across the wall of PP-R1 while the degradation was significant only at the inner surface in the case of PP-R2.
- Degradation/extraction of the degradation product of AO-13 was found in PP-R1 and PP-R2.
- From the AO loss coefficients (D′) determined by μFT-IR, the loss of both AO-18 and AO-13 was higher in PP-R1 than PP-R2.
- M_w of PP determined by SEC showed a more significant reduction in the case of PP-R1 than PP-R2.
- A linear relation connecting the M_w of the polymer with the corresponding C/C_0 of AOs was established. In comparison to that of PP-$R2_{Cl}$, the greater slope of the linear relations indicates a faster degradation of AO and the polymer in PP-$R1_{Cl}$.

7.2.3 Influence of chlorine concentration

The effect of the chlorine concentration on the ageing of PP-R1 and PP-R2 was investigated using the analytical techniques and methods described in section 5.

7.2.3.1 ATR spectroscopy

At 10 mg/L a white powdery substance was formed at the inner surface of the pipes. Images of the virgin and aged pipe and the ATR spectrum of the powder formed at the inner surface of the pipe are presented in Figure 68.

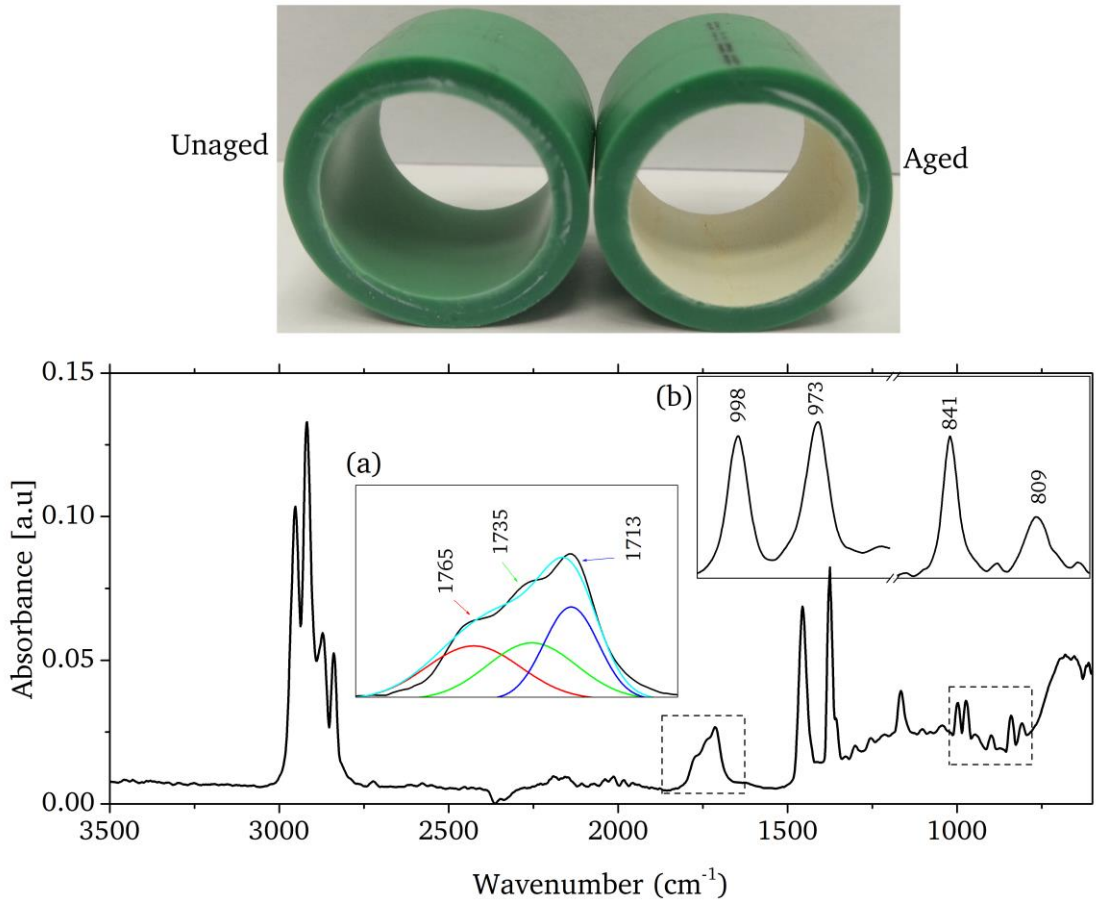

Figure 68: ATR spectrum of the white powder from the inner surface of PP-R1$_{Cl}$, aged at 95 °C and 10 mg/L of chlorine (a) region corresponding to the absorption of PP degradation products (b) region corresponding to the characteristic absorption of PP between 1000-800 cm^{-1}.

The absorptions of degradation products of PP at 1713 (ketones), 1735 (peracids) and 1765 cm^{-1} (γ-lactones) were detected [109, 110]. The formation of these degradation products was discussed in section 3.3.

7.2.3.2 Infrared microscopy

The distribution of AO-18 across the pipe wall for different chlorine concentrations was determined as explained in section 7.2.1.3 and the obtained results are presented in Figure 69.

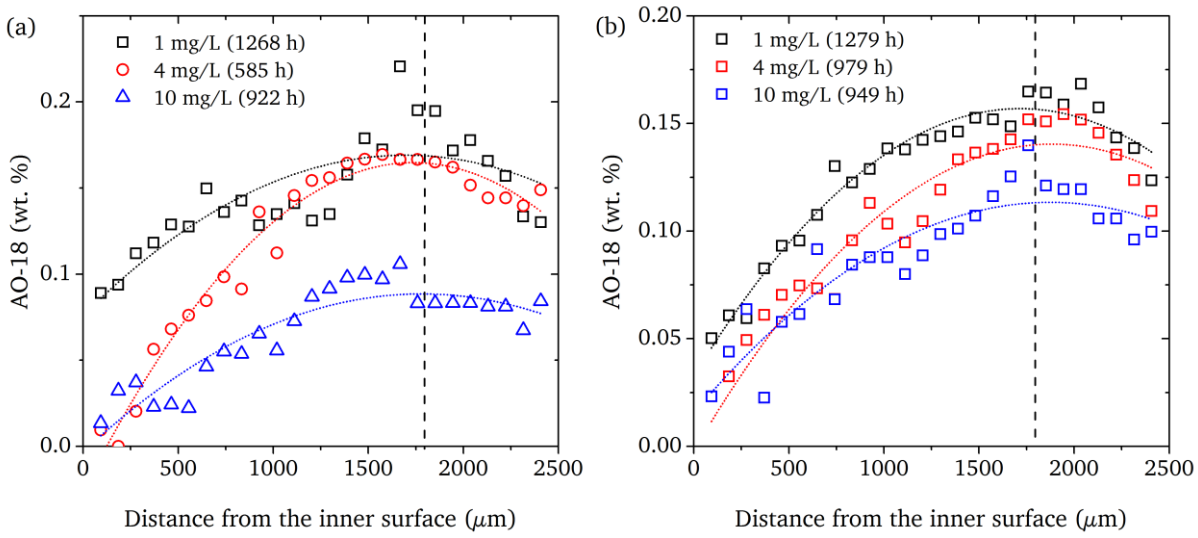

Figure 69: Distribution of AO-18 across the wall of (a) PP-R1$_{Cl}$ and (b) PP-R2$_{Cl}$.

For both series the loss of AO-18 is bilateral in nature, but with different rates. The loss of AO was higher from the inner surface than from the outer one. Since the contact with chlorinated water takes place at the inner surface, the loss of AO-18 through the outer surface is not related to the effect of chlorinated water. Consequently, to carve out the effect of chlorinated water on the loss of AOs the content was averaged until 1800 μm (dotted line in Figure 69) from the inner surface. The variation of the C/C_0 of AOs (determined as discussed in section 7.2.1.3) in PP-R1$_{Cl}$ and PP-R2$_{Cl}$ with ageing time for different chlorine concentrations was determined (Figure 70).

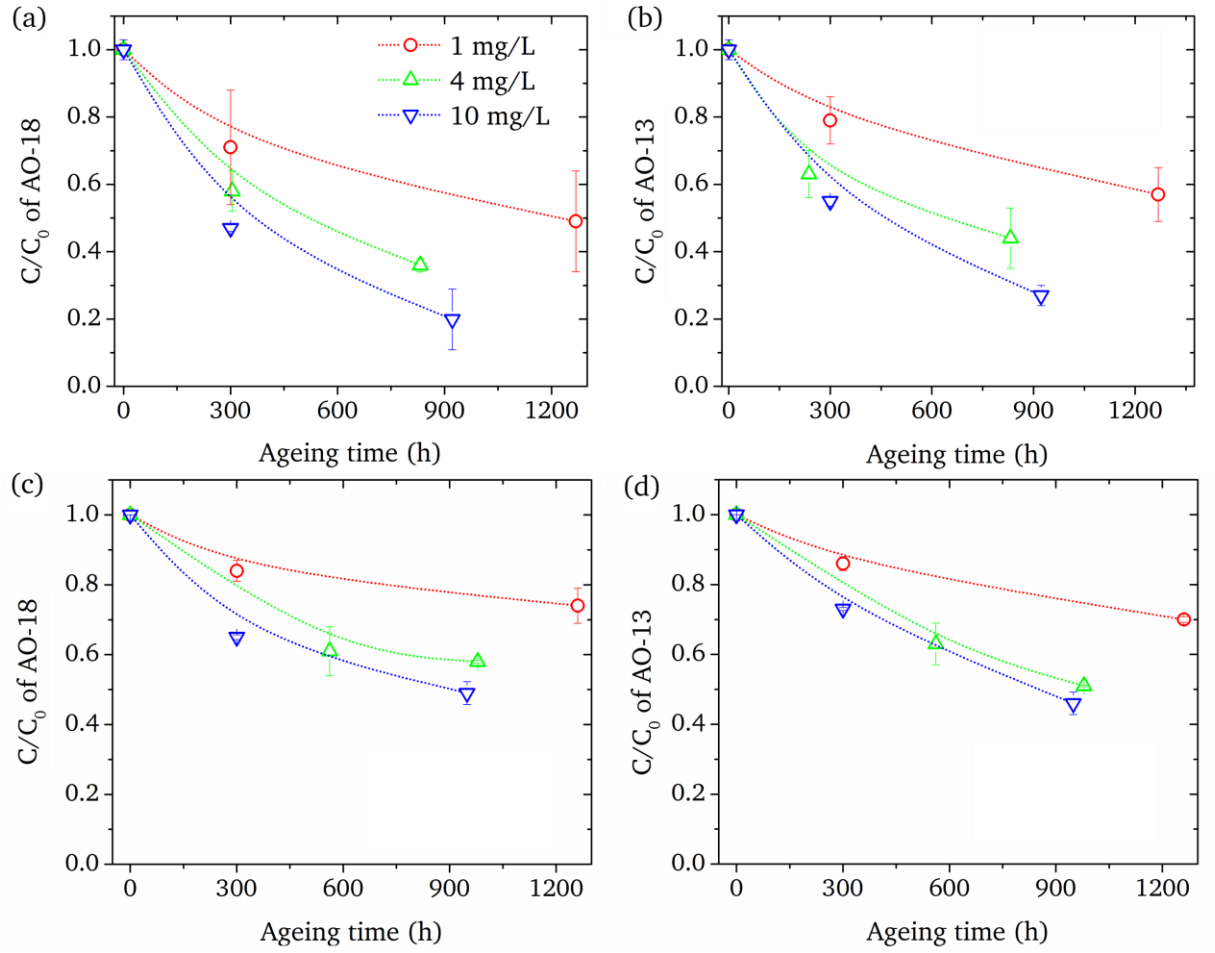

Figure 70: Effect of chlorine concentration on the content of AOs (averaged until 1800 µm from the inner surface) in PP-R1$_{Cl}$ (a) AO-18 and (b) AO-13 and in PP-R2$_{Cl}$ (c) AO-18 and (d) AO-13.

An increase in the concentration of chlorine leads to a higher concentration of the reactive species HOCl, $Cl_2^{-\bullet}$ and $^{\bullet}OH$ (eq. 8 and 9). Consequently, an accelerated formation of radicals by hydrogen abstraction from the polymer can be expected, which has to be terminated by the donation of phenolic hydrogen from AOs. Hence, it can be expected that the loss of AOs will be more significant with increasing the concentration of chlorine in the water (Figure 70). A significant difference in the loss rate of AOs between PP-R1$_{Cl}$ and PP-R2$_{Cl}$ is observed in Figure 70. The content of both AO-18 and AO-13 in PP-R2$_{Cl}$ is above that in PP-R1$_{Cl}$ irrespective of the chlorine concentration. Hence the loss of AOs from PP-R2$_{Cl}$ was less favored than from PP-R1$_{Cl}$.

7.2.3.3 OIT measurements

In analogy to section 7.2.3.2, the OIT values were averaged up to a depth of 1800 μm from the inner wall surface. The variation of the normalized OIT for pipes aged at

different chlorine concentrations as a function of ageing time is presented in Figure 71.

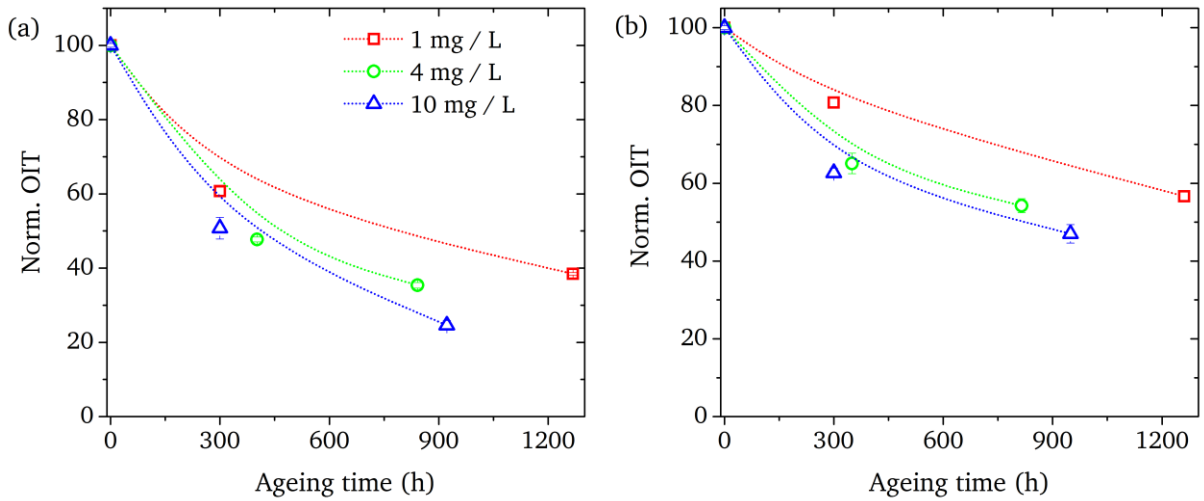

Figure 71: Variation of OIT values as a function of ageing time of samples aged under different chlorine concentration (averaged until 1800 µm from inner surface) (a) PP-R1 and (b) PP-R2.

The OIT values of pipes aged under different chlorine concentration decrease with time for both pipes. However, the values for PP-R1 decrease faster than for PP-R2. The OIT values averaged from the inner surface to 1800 μm across the pipe wall are plotted against the chlorine concentration to determine the effect of chlorinated water on the OIT of PP-R1$_{Cl}$ and PP-R2$_{Cl}$ (Figure 72).

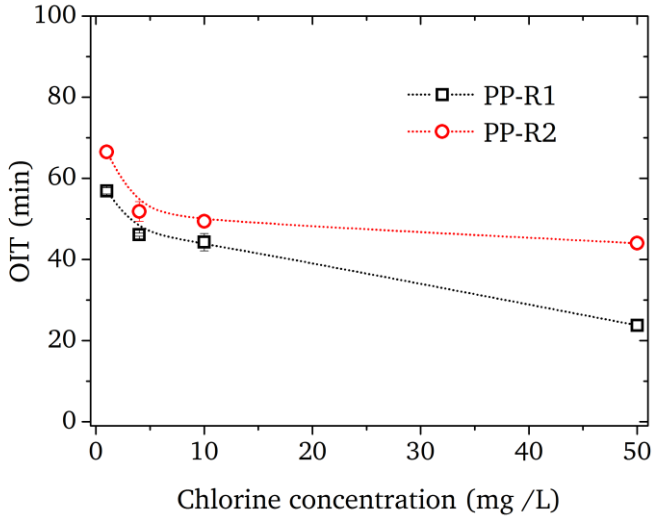

Figure 72: Variation of OIT values of samples aged for 300 h with chlorine concentration (averaged until 1800 µm from the inner surface).

From Figure 72 it can be seen that the OIT values decrease continuously with increasing chlorine concentration. However, the impact of chlorinated water is more pronounced for PP-R1. These results confirm that the rate of radical formation differs between PP-R1 and PP-R2, which will subsequently result in different rates of AO degradations. As discussed previously for the case of samples aged at 4 mg/L, the difference in degradation rates obtained for pipes aged at higher chlorine concentrations can be attributed to the different morphology of the polymer.

7.2.3.4 Size exclusion chromatography

The MMD of samples taken at different depths of PP-R1$_{Cl}$ aged for 900 h at a chlorine concentration of 10 mg/L is presented in Figure 73.

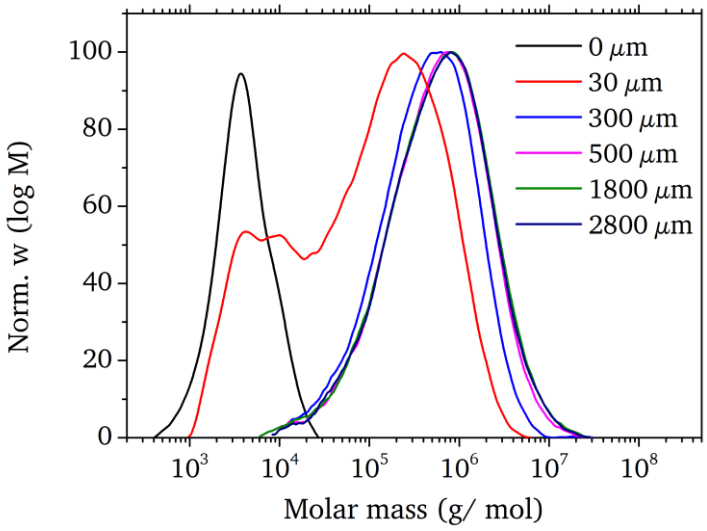

Figure 73: MMD of PP-R1$_{Cl}$ at different positions of the pipe wall

A shift of the MMD towards the low molar mass region can be seen from the outer to the inner surface of PP-R1$_{Cl}$. The MMD of the polymer at a depth of 30 μm shows a bimodal character in which the average molar mass of the lower half-distribution is comparable to that of the powder layer. The bimodal nature can be explained by the fact that this sample (up to a depth of 30 μm) contains highly degraded material (powdery layer) and a portion of partly degraded polymer.

The MMD of PP-R1$_{Cl}$ and PP-R2$_{Cl}$ aged at different chlorine concentrations for ~300 h is presented in Figure 74.

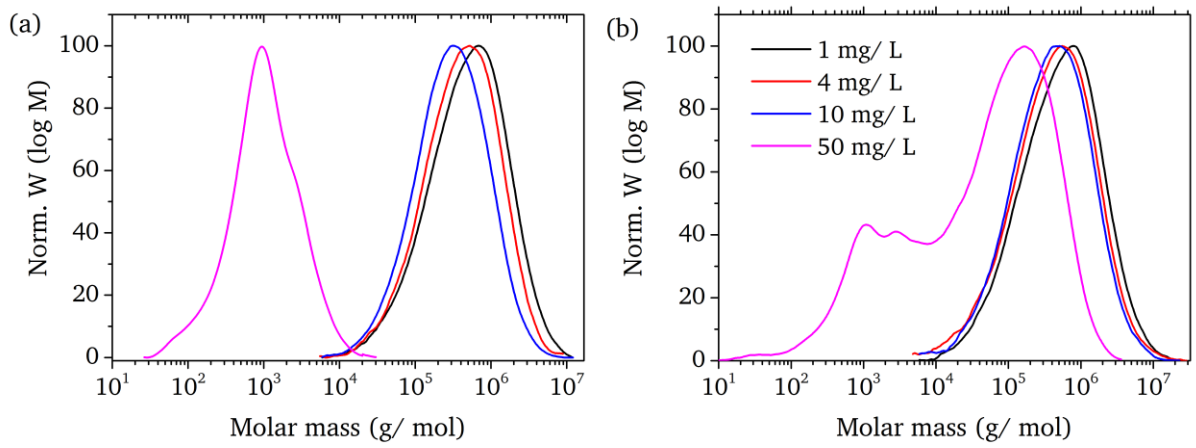

Figure 74: MMD of the polymer taken at ~20 µm depth from the inner surface of PP-R pipes aged (~300 h) at different chlorine concentration (a) PP-R1$_{Cl}$ and (b) PP-R2$_{Cl}$.

The degradation rate of AOs was higher in PP-R1$_{Cl}$ than in PP-R2$_{Cl}$. Consequently, a higher degradation rate of the polymer can also be expected in PP-R1$_{Cl}$. The shift in MMD to the low molar mass region at higher chlorine concentration can be seen in Figure 74. A crucial difference in the MMD can be recognized for samples aged at a chlorine concentration of 50 mg/L. In this case, PP-R1$_{Cl}$ shows a unimodal MMD while PP-R2$_{Cl}$ shows a bimodal MMD. The MMD of the samples aged with a chlorine concentration of 50 mg/L has the lowest average molar mass than that of the samples aged with chlorine concentrations 1, 4 and 10 mg/L. The bimodal MMD of PP-R2$_{Cl}$ shows a peak maximum in the low molar mass region at a value similar to that of PP-R1$_{Cl}$, and another maximum in the high molar mass region. The bimodal nature of the MMD explains that it contains a fraction of highly degraded layer in combination with a partly degraded layer of polymer. From the intensity of the MMD curves it is clear, that the amount of highly degraded material present in PP-R1$_{Cl}$ is larger than that of the sample obtained from PP-R2$_{Cl}$. This indicates a higher rate of the degradation of polymer in PP-R1$_{Cl}$. The variation of M_w with ageing time for PP-R samples taken from the inner surface of the pipes aged under different chlorine concentration is presented in Figure 75.

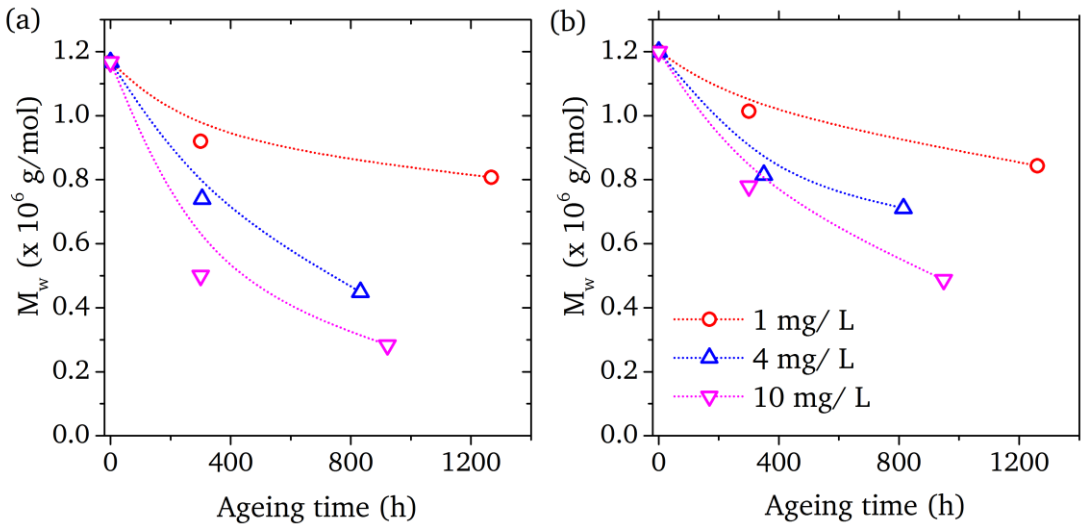

Figure 75: M_w for a layer of 20 µm from the inner surface of the pipe as a function of time for (a) PP-R1$_{Cl}$ and (b) PP-R2$_{Cl}$.

The decrease in M_w with ageing time is clearly visible in Figure 75. In order to characterize the effect of chlorine concentration, the M_w of the samples was plotted as a function of the chlorine concentration (Figure 76).

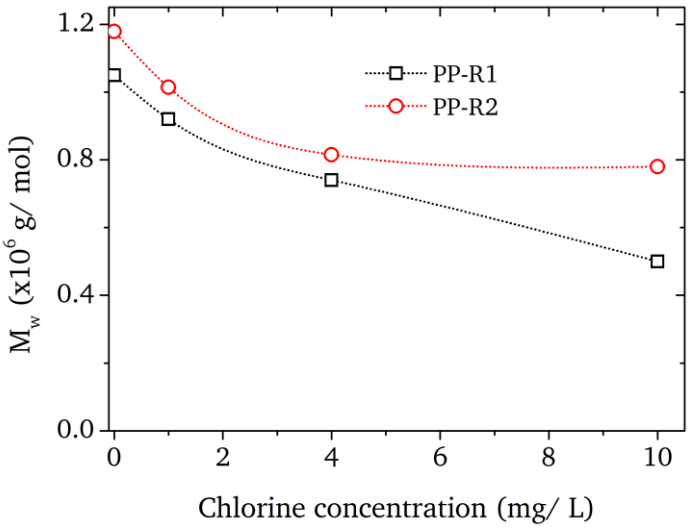

Figure 76: Variation of the M_w of polymer taken at a depth of ~20 µm from the inner surface of pipes aged for 300 h with different chlorine concentrations.

Figure 76 shows that the M_w of samples decreases with chlorine concentration. However, the rate of decrease is higher for PP-R1 compared to PP-R2. The relationship between M_w vs. chlorine concentration correlates well with the profile of OIT vs. chlorine concentration as depicted in Figure 72. As explained previously, an increase in the concentration of HOCl and its degradation products as a result of

higher chlorine concentrations triggers the formation of radicals in the polymer backbone. Consequently, the rate of chain scission will be higher and, thereby, a significant reduction in the molar mass of the polymer can be seen. An additional factor, which slowed the degradation of the polymer in PP-R2 was the lower permeability towards the ageing media due to the peculiar arrangement of polymer chains.

7.2.3.5 Summary

Pipes (α-nucleated PP-R1 and β–nucleated PP-R2) aged at different chlorine concentration were analyzed by ATR, μFT-IR, DSC and SEC. Based on the experimental results the following conclusions can be made:

- Due to the effect of high chlorine concentrations, a highly degraded white powder layer consisting of very low molar mass polymer was formed. Spectroscopically, carbonyl functionalities could be identified, hinting at a high degree of polymer degradation.
- The content of AOs in the pipes consistently decreased with time and chlorine concentration.
- The higher rate of radical formation along the polymer backbone caused the faster consumption of AOs in PP-R1. As a result the average molar mass of the polymer in PP-R1 dropped faster than PP-R2.

7.2.4 Ageing of pipes with hot water

Hydrostatic pressure tests of the pipes were carried out in hot water with the latter being present at both surfaces of the pipe. The temperature used for this study was set at 95 °C, and the samples are abbreviated as PP-R1$_W$ and PP-R2$_W$.

7.2.4.1 Infrared microscopy

The time and space resolved C/C$_0$ of AO-18 as determined from μFTIR is shown as color coded contour plot in Figure 77.

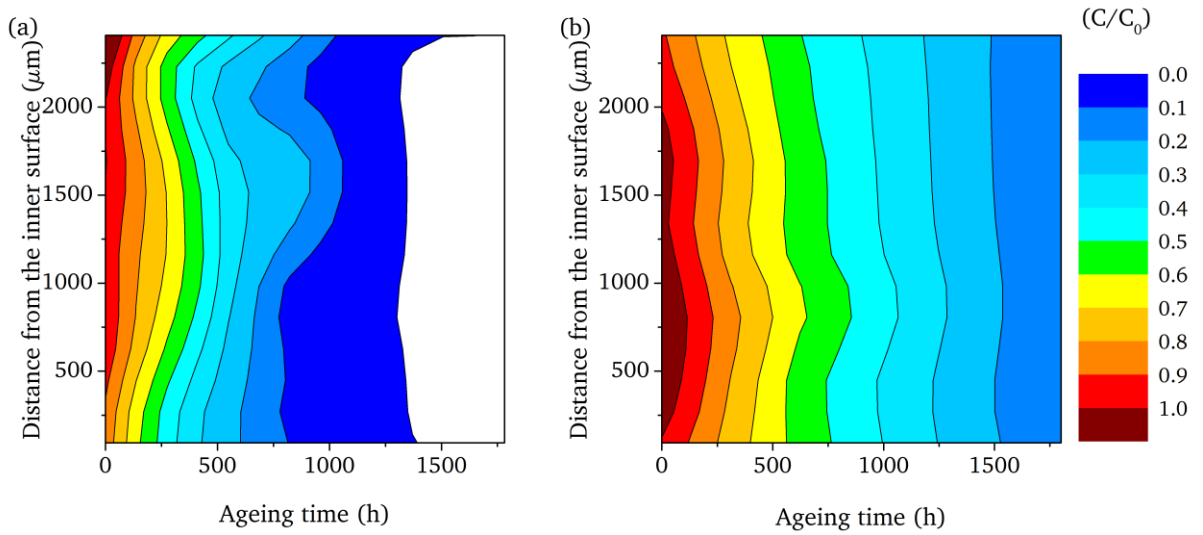

Figure 77: Time and space resolved contour plots of AO-18 in PP-R1$_W$ and PP-R2$_W$.

Figure 77 delivers that the loss of AO-18 in PP-R1$_W$ and PP-R2$_W$ takes place from both inner and outer surface, which is the result of the presence of water medium on both surfaces. However, the rate of AO-18 loss differs remarkably between PP-R1 and PP-R2. Comparing the content of AO-18 after 1500 h reveals that it is completely depleted from PP-R1$_w$ while PP-R2$_w$ is satisfactorily stabilized. This suggests that the rate of degradation of AO-18 is larger in PP-R1$_w$ than in PP-R2$_w$. Analogously, the content of AO-13 in PP-R1$_w$ and PP-R2$_w$ was determined from μFT-IR and the results are depicted in Figure 78.

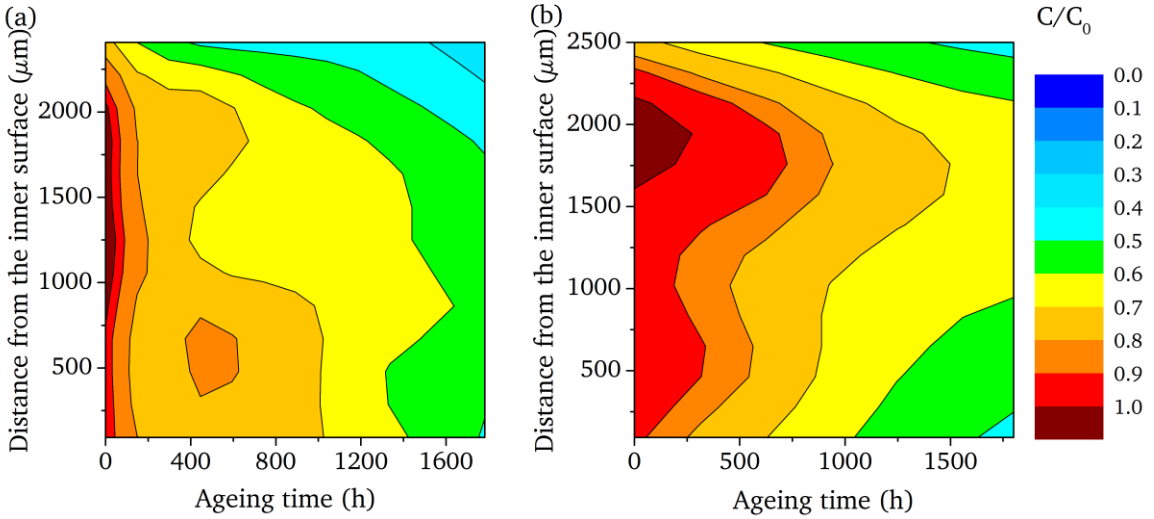

Figure 78: Time and space resolved contour plots of AO-13 in PP-R1$_W$ and PP-R2$_W$.

The drop in content of AO-13 also shows a bilateral nature, similar to AO-18. However, in PP-R1 the loss of AO-13 occurs mainly through the outer surface. The loss of AO-13 from the outer surface of PP-R1 pipes was already observed in chlorinated water ageing in which the outer surface of the pipe was exposed to air. From the comparison of the content of AOs from pipes aged in chlorinated water and hot water it can be concluded that the rate of deterioration is higher in chlorinated water. The formation of quinones was quantitatively analyzed for a specimen aged for 1316 h. Figure 79 shows the distribution of quinones and AO-13 remained in the pipe wall as determined by Extraction→HPLC and μFT-IR.

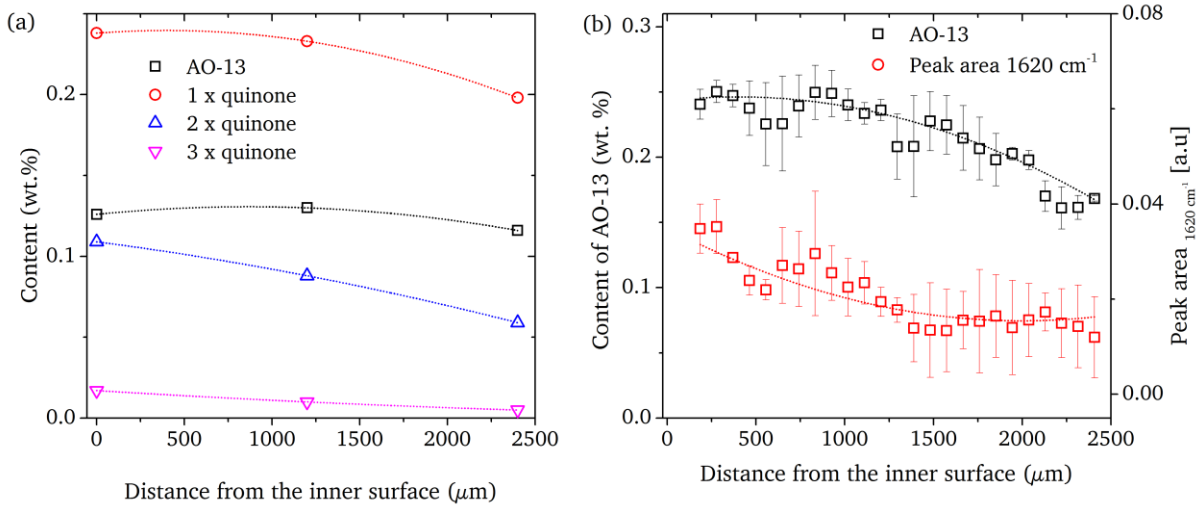

Figure 79: (a) Distribution of quinones and the remaining AO-13 as determined from Extraction→HPLC and (b) Distribution of AO-13 and the peak area of the band at 1620 cm^{-1} obtained from μFT-IR.

The content of quinones as determined by Extraction→HPLC decreases from the inner to the outer surface of the pipe, which is supported by the profile obtained by plotting the peak area of the band at 1620 cm^{-1} from μFT-IR. There are no additional bands observed in the IR spectrum, which could provide evidence for further reactions of quinones. The content of quinones in PP-$R1_W$ and PP-$R2_W$ at a depth of 100 μm from the inner surface was determined from the band area of 1620 cm^{-1} for different ageing times (Figure 80).

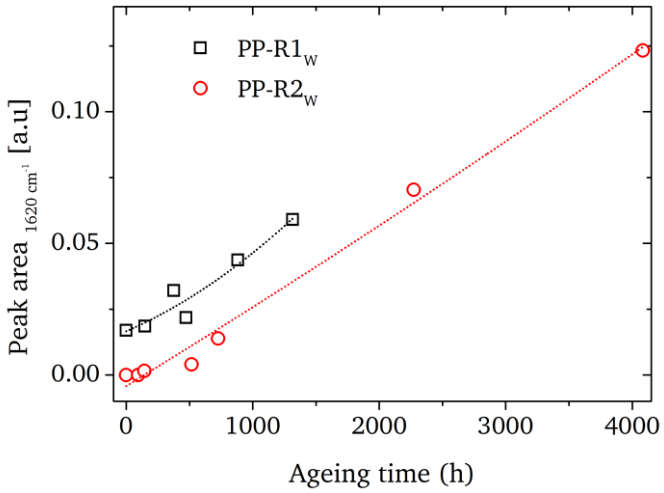

Figure 80: Variation of the peak area of 1620 cm^{-1} with ageing time

Figure 80 shows that the band area increases with time for both pipes. However, the higher area of the band in PP-R1 than PP-R2 indicates that AO-13 is more susceptible to degradation in PP-R1. It was previously discussed that AO-13 does not react with water as it is not susceptible to hydrolysis. Hence, the degradation of AO-13 can only proceed via oxidation. Therefore, the rate of degradation of AO-13 depends on the amount of radicals formed at the polymer. Radicals at the inner surface of the pipe can be formed by the reaction with oxygen at elevated temperatures, while the radicals at places remote to the surfaces can only be formed by chain transfer reactions or by the chlorine penetrated along with hot water into the pipe wall. It was previously discussed that chain transfer reactions are independent of the morphology while the penetration of the media highly depends on it. Moreover, the penetration of the media is greater in PP-R1 due to the alignment of polymer chains along MD. Therefore, a higher rate of radical formation in PP-R1 is observed, which implies a higher rate of degradation for AO-13. Unlike in the case of ageing in chlorinated water, the band area at 1620 cm^{-1} linearly increases with ageing time, which indicates that further reactions or extraction of quinones do not take place in hot water.

In order to explain the AO content profiles, D′ values were calculated as described previously and are tabulated in Table 12.

Table 12: D' values of AO-18 and AO-13 calculated by fitting the theoretical values of C/C_0 with the measured values.

Sample	Loss coefficient (D′) x 10^{-9} cm^2/ s	
	AO-18	AO-13
PP-$R1_W$	3	0.8
PP-$R2_W$	1.5	0.4

Comparing the two materials, the D′ values of AOs are two times higher for PP-$R1_W$ than for PP-$R2_W$. Additionally, on comparing the D′ values of AO-18 with AO-13 it can be concluded that the loss of AO-18 is almost 4 times faster than that of AO-13 in both pipes.

The loss of AOs from the pipes aged under hot water and chlorinated water significantly differs. Reaction of AO-13 with chlorinated water via dehydrogenation [37] leads to the formation of quinones, which can also be formed in parallel by donating the hydrogen to the radicals at the polymer. However, the quinones formed in pipes during ageing with hot water are solely the result of donating the phenolic hydrogen to the macroradicals. From Table 10 and Table 12 it becomes clear that the loss of AO-18 is faster in hot water medium, while AO-13 loss is faster in chlorinated water.

7.2.4.2 Oxidative Induction Time

To confirm the results obtained from μFT-IR with a reference technique, OIT measurements were performed on samples mechanically prepared from different depths of the pipe wall. The profiles of the OIT values across the pipe wall of PP-$R1_W$ and PP-$R2_W$ are presented for comparable ageing times in Figure 81.

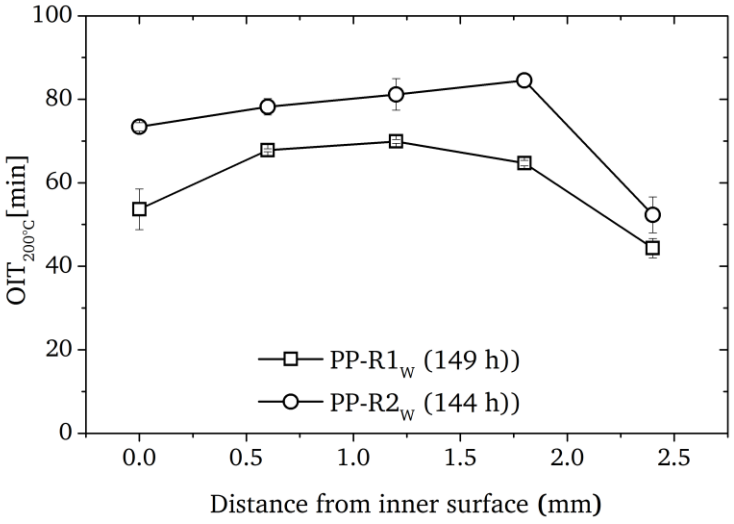

Figure 81: OIT profile across the pipe wall of PP-R1$_W$ and PP-R2$_W$.

Generally, the OIT values of PP-R2$_W$ are higher than those of PP-R1$_W$, which is due to the higher initial content of AO-13 (Table 8). Likewise, in the ageing of chlorinated water, a remarkable fall of the OIT values towards the outer surface can be observed for both samples. Hot water was applied from both surfaces of the pipe, which in turn results in a bilateral AO loss (Figure 77 and Figure 78). The comparison of the average value of the OIT across the pipe wall with a value of a sample taken at a depth of 200 μm from the inner surface is presented in Figure 82.

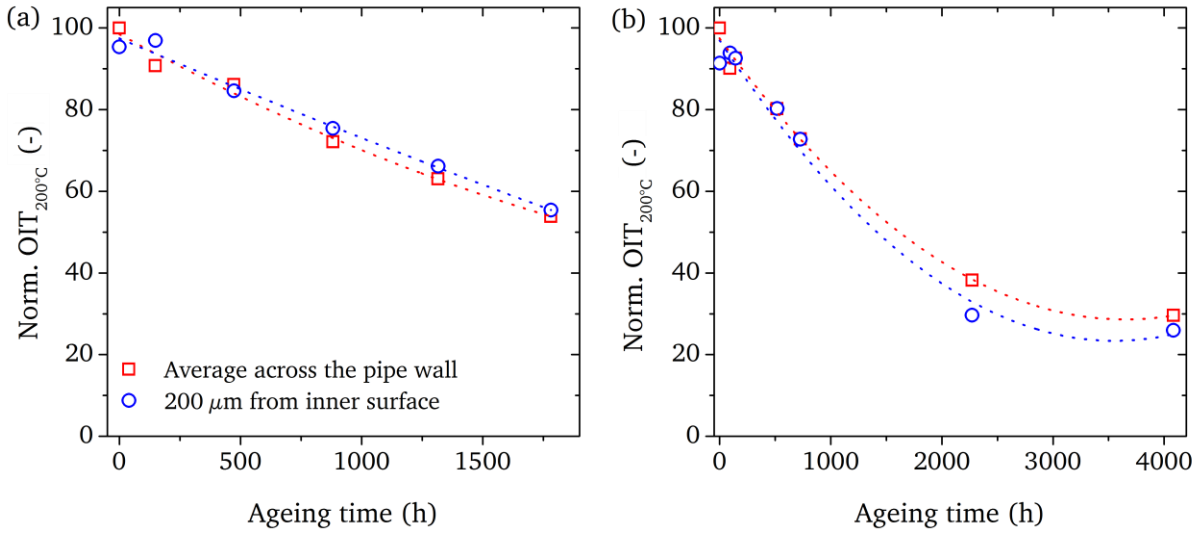

Figure 82: Effect of hot water on OIT values of (a) PP-R1$_W$ and (b) PP-R2$_W$.

Figure 82 demonstrates that the OIT does not show any significant variation when comparing the average value across the wall with the value at the inner surface. From

the profiles of OIT (Figure 82) and AO content (Figure 77 and Figure 78) it is evident that the loss of AO occurred from both the inner and outer surface. The time and space resolved OIT profiles of PP-R1$_W$ and PP-R2$_W$ are presented in Figure 83.

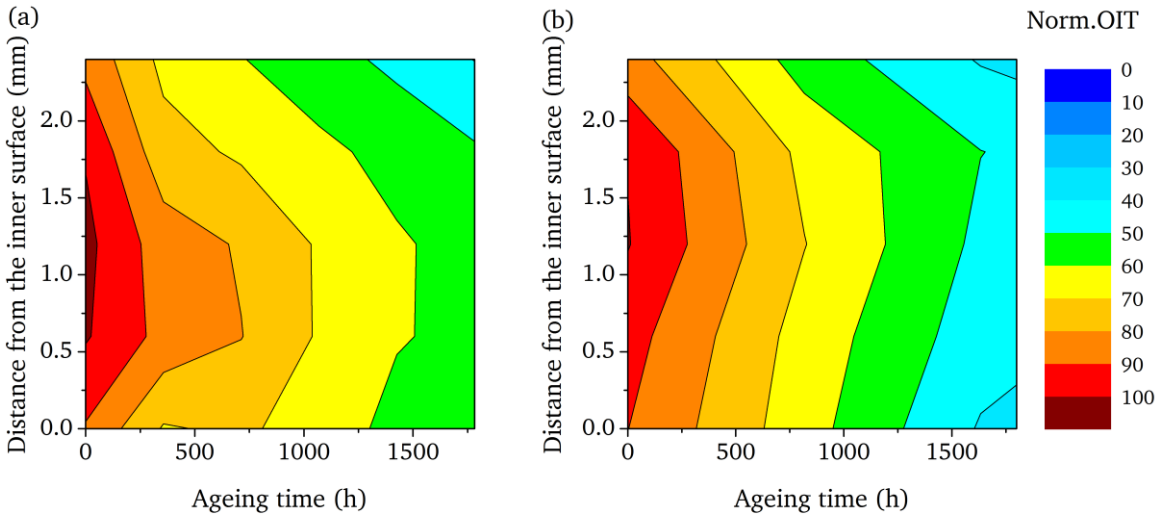

Figure 83: Time and space resolved OIT profiles of samples (a) PP-R1$_W$ and (b) PP-R2$_W$.

From Figure 83 the drop in OIT is observed all over the pipe wall of both PP-R1$_W$ and PP-R2$_W$, which is in agreement with the AO content profiles obtained from μFT-IR (Figure 77 and Figure 78).

7.2.4.3 Size exclusion chromatography

The molar mass distribution of the polymer was analyzed by SEC as explained previously and the variation of the M_w with time is presented in Figure 84.

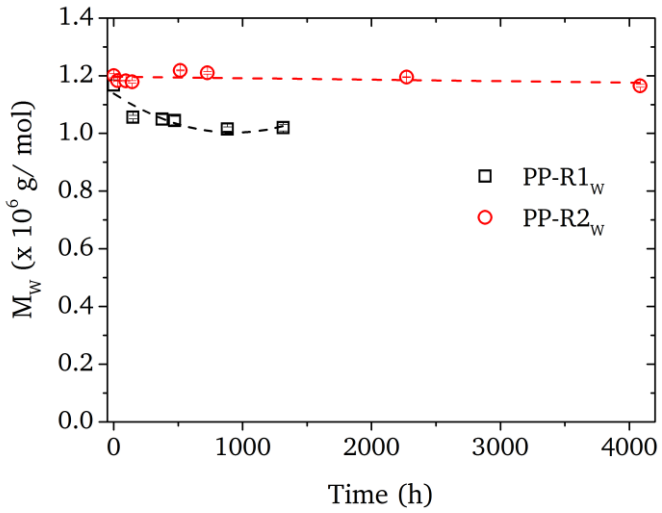

Figure 84: Variation of M_w of the samples taken at a depth of ~20 µm from the inner surface of PP-R1$_W$ and PP-R2$_W$ with time.

M_w of PP-R2$_W$ remains almost unchanged, whereas in the case of PP-R1$_W$ a minute decrease with time is observed. Due to a higher content of AO in PP-R2$_W$ (Table 8) the hot water is unable to impart the degradation of PP, which is clear from Figure 84. The relation between the M_w of the polymer and C/C_0 of AOs is plotted in Figure 85.

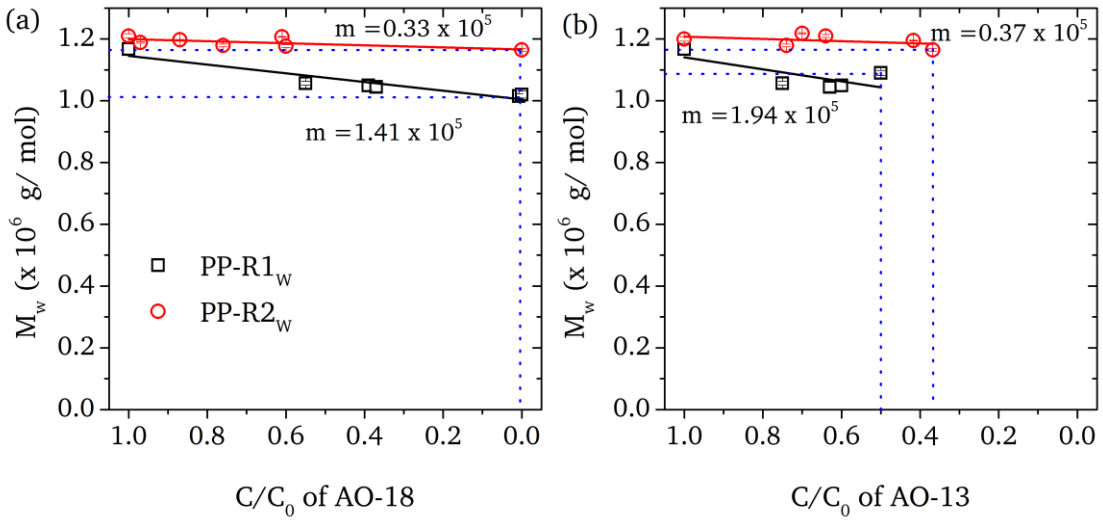

Figure 85: Relation between M_w and the C/C_0 of AO from the inner surface of the pipe for (a) AO-18 and (b) AO-13 in PP-R1$_W$ and PP-R2$_W$.

The decrease in the M_w of the polymer with ageing time correlates linearly with the content of AOs (C/C_0) present in the polymer. However, the slope of the linear relations varies significantly between PP-R1 and PP-R2, having a larger value for PP-R1. Hence, the rate of degradation of the AOs and thereby the degradation of the polymer is higher in PP-R1. The slope of the linear relation of M_w vs. the content of AOs obtained for PP-R1$_W$ and PP-R2$_W$ is tabulated in Table 13.

Table 13: Slope of the linear relations depicted in Figure 85.

Sample	Slope of the relation between M_w (x 10^5 g/mol) and	
	AO-18	AO-13
PP-R1$_W$	1. 41	1. 94
PP-R2$_W$	0. 33	0. 374

7.2.4.4 Summary

The changes in differently nucleated (α-nucleated PP-R1 and β-nucleated PP-R2) and stabilized pipes made from PP-R during hydrostatic pressure testing with hot water as

inner medium were evaluated. From the experimental results following conclusions can be made:

- The presence of hot water at both surfaces of the wall of the pipes caused the bilateral loss of antioxidants (AOs).
- The easiness of penetration of the ageing media through the polymer networks due to the consistent alignment of polymer chains in PP-R1 accelerated the degradation of AOs present in it when compared to PP-R2.
- As a result of the accelerated degradation of AOs the average molar mass of the polymer in PP-R1 dropped comparatively faster than PP-R2.
- The rate of degradation of AO-18 was higher than that of AO-13. In water the degradation of AO-18 proceeded via two mechanisms, namely the hydrolysis of the ester groups and the donation of hydrogen atom to the macroradicals. However, the degradation of AO-13 proceeded only via the donation of hydrogen to the macroradicals.

8 Conclusions

The aim of the research work was to quantify the effects of welding and the influence of deteriorating environments on products made of polypropylene (PP). A central aspect common to both aims was the development of methods based on infrared microscopy (μFT-IR) to monitor structural changes in polypropylene (PP). The results from μFT-IR were to be augmented by the classical analytical approach of mechanically preparing samples and analyzing them individually by differential scanning calorimetry (DSC), Extraction→HPLC, size exclusion chromatography (SEC) and polarized light microscopy (PLM).

Injection molded plates were prepared for welding from non-nucleated (PP-H1) and α-nucleated (PP-H2) polypropylene. In the injection molded plates of PP-H1, low crystallization rates caused the formation of clearly grown α- and β-spherulites, whereas in PP-H2, the crystallization rates were high and caused the formation of solely fine α-spherulites. For the welding the injection molded plates were brought into contact with a heated metallic plate until the polymer melts and the melted surfaces were compressed with a constant pressure until solidification of the melt. Due to the interplay between heating and cooling rates anisotropies with regard to crystal structures were formed in the welds. The qualitative analysis of the weld using PLM can clearly distinguish three regions, namely the injection molded plates, the weld seams and the weld core. In PP-H1, the high cooling rates at the weld seams lead to the formation of α-polymorph. The spherulites found in the weld seams were elongated as a result of the shear force exerted during welding. The lower cooling rates at the weld core met the crystallization conditions of α- and β-spherulites. Due to the fine size of the α-spherulites in PP-H2 it was difficult to distinguish the anisotropies with regard to spherulite size and shape developed upon welding.

The orientation of the polymer chains at the welds was determined from μFT-IR: In general, the degree of orientation in PP-H2 was higher than in PP-H1, which was the result of two facts: The first one was that the chains of the injection molded plates were preoriented along the direction of injection. Secondly, the fast crystallization of the oriented chains of the polymer melt, triggered by the nucleating agent, caused a freezing of the orientation inferred by the shear force. The orientation of the chains at the weld seams was influenced by the shear force and the outward melt flow direction (along ND). Crystallization of the sheared melt at the weld seams caused the

formation of stretched spherulites with an orientation of the chains along ND. Changes of the chemical composition as a result of the welding process were analyzed for the first time: During welding the polymer was in contact with oxygen at elevated temperatures, which can cause the degradation of antioxidants (AOs) and the polymer itself. Degradation of phenolic and phosphitic AOs either by physical loss or by chemical consumption was concluded from their distribution across the weld. Using the concept of dichroism it could be shown that thermo-oxidative degradation of PP chains occurred during welding, even in the presence of AOs. The extent of physical loss could not be quantified.

The pipes chosen for the durability studies were made of PP with a low percentage of ethylene comonomer, nucleated with α- and β-nucleating agents (PP-R1 and PP-R2, respectively). These pipes were stabilized with different contents of phenolic AOs. A major problem in the quantification AOs using μFT-IR was the overlapping of the characteristic bands, when it is in mixture with other AOs or with the polymer. A new method has been developed to quantify individually the phenolic AOs from the mixture.

The deterioration of the macroscopic properties of PP is the result of the loss of AOs and the subsequent drop in the molar mass of the polymer. In the case of pipes aged in chlorinated water degradation of AOs occurred continuously across the wall of PP-R1 while it was significant only at the inner surface of PP-R2. The degradation of AOs and the polymer at positions remote from the surfaces can take place either by chain transfer reactions of the macroradicals formed at the inner surface and or by the penetration of the ageing media through the polymer network. Random orientation of the polymer chains at the inner surface of PP-R2 hindered the penetration of the ageing media and thus led to a low rate of degradation of the AOs and the polymer. In PP-R1, the polymer chains were aligned consistently along the direction of extrusion, which made the penetration of the media easier and thus lead to a higher rate of degradation. In the meanwhile new bands, which were attributed to the degradation products of AOs, originated in the infrared spectrum at 3632, 1620 and 1640 cm^{-1} and their intensity increased with ageing time. These AO degradation products were further degraded/extracted from the pipe wall in the presence of chlorinated water while they were accumulated in the pipe during the ageing experiments with hot water. The consequence of the degradation of AOs was observed in the polymer as the reduction in molar mass. The average molar mass (M_w) of the polymer determined

from SEC was continuously decreasing with ageing time. A relation connecting the M_w of the polymer with the corresponding relative content (C/C_0) of AOs revealed that PP-R1 underwent degradation faster than PP-R2. The strong oxidizing radicals present in chlorinated water accelerated the degradation of AOs and the polymer compared to hot water as inner medium. At high chlorine concentrations in the water the formation of a highly degraded powdery layer of polymer at the inner surface of the pipes was observed. This layer consists of PP with very low molar mass and the IR spectroscopic analysis showed carbonyl functionalities of PP degradation products.

9 References

1. Manas Chanda, S.K.R., *Industrial Polymers, Specialty Polymers, and Their Applications* 2009: CRC Press, Taylor & Francis Group.
2. Soares, J.B.P. and T.F.L. McKenna, *Introduction to Polyolefins*, in *Polyolefin Reaction Engineering*. 2012, Wiley-VCH Verlag GmbH & Co. KGaA. p. 1-13.
3. Struik, L.C.E., *The mechanical behaviour and physical ageing of semicrystalline polymers: 2.* Polymer, 1987. **28**(9): p. 1534-1542.
4. Struik, L.C.E., *Mechanical behaviour and physical ageing of semi-crystalline polymers: 4.* Polymer, 1989. **30**(5): p. 815-830.
5. Yu, L., et al., *Polypropylene random copolymer in pipe application: Performance improvement with controlled molecular weight distribution.* Thermochimica Acta, 2014. **578**(0): p. 43-52.
6. Maier, C. and T. Calafut, *Polypropylene: The definitive user's guide and databook*, C. Maier and T. Calafut, Editors. 1998, William Andrew Publishing: Norwich, NY. p. 11.
7. Natta, G., et al., *CRYSTALLINE HIGH POLYMERS OF α-OLEFINS.* Journal of the American Chemical Society, 1955. **77**(6): p. 1708-1710.
8. Sterzynski, T., et al., *Structure and properties of nucleated random and block copolymers of propylene.* Advances in Polymer Technology, 1994. **13**(1): p. 25-36.
9. Hikosaka, M. and T. Seto, *The Order of the Molecular Chains in Isotactic Polypropylene Crystals.* Polym J, 1973. **5**(2): p. 111-127.
10. C, S.J., *Polymeric materials encyclopedia*. 1996, Boca Raton (USA): CRC press.
11. Jacoby, P., et al., *Studies on the beta-Crystalline form of Isotactic Polypropylene.* Journal of Polymer Science: Part B Polymer Physics, 1986. **24**(3): p. 461-491.
12. Karger-kocsis, J. and J. Varga, *Effects of β-α transformation on the static and dynamic tensile behavior of isotactic polypropylene.* Journal of Applied Polymer Science, 1996. **62**(2): p. 291-300.
13. Li, J.X., W.L. Cheung, and C.M. Chan, *On deformation mechanisms of β-polypropylene 2. Changes of lamellar structure caused by tensile load.* Polymer, 1999. **40**(8): p. 2089-2102.
14. Tjong, S.C. and S.A. Xu, *Non-isothermal crystallization kinetics of calcium carbonate-filled β-crystalline phase polypropylene composites.* Polymer International, 1997. **44**(1): p. 95-103.
15. Tordjeman, P., et al., *The effect of alpha, beta crystalline structure on the mechanical properties of polypropylene.* Eur. Phys. J. E, 2001. **4**(4): p. 459-465.
16. Lotz, B. and J.C. Wittmann, *The molecular origin of lamellar branching in the α (monoclinic) form of isotactic polypropylene.* Journal of Polymer Science Part B: Polymer Physics, 1986. **24**(7): p. 1541-1558.
17. Samuels, R.J., *Structured polymer properties: the identification, interpretation, and application of crystalline polymer structure*. Structured polymer properties. 1974, New York: Wiley.
18. Khoury, F., *The Spherulitic Crystallization of Isotactic Polypropylene From Solution: On the Evolution of Monoclinic Spherulites From Dendritic Chain-Folded Crystal Precursors.* Journal of research of the National Bureau of Standards. Section A. Physics and chemistry., 1966. **70A**(1): p. 29-61.
19. Varga, J., *Supermolecular structure of isotactic polypropylene.* Journal of Material Science, 1992. **27**(10): p. 2557-2579.
20. Marentette, J.M. and G.R. Brown, *Polymer spherulites: I. Birefringence and morphology.* Journal of Chemical Education, 1993. **70**(6): p. 435.
21. Luo, F., et al., *New Understanding in Tuning Toughness of β-Polypropylene: The Role of β-Nucleated Crystalline Morphology.* Macromolecules, 2009. **42**(23): p. 9325-9331.
22. Chen, Y.-H., et al., *Unusual Tuning of Mechanical Properties of Isotactic Polypropylene Using Counteraction of Shear Flow and β-Nucleating Agent on β-Form Nucleation.* Macromolecules, 2009. **42**(12): p. 4343-4348.

23. Zheng, G., et al., *Negative effect of stretching on the development of β-phase in β-nucleated isotactic polypropylene.* Polymer International, 2011. **60**(7): p. 1016-1023.
24. Phulkerd, P., et al., *Anomalous mechanical anisotropy of β form polypropylene sheet with N,N'-dicyclohexyl-2,6-naphthalenedicarboxamide.* Polymer, 2011. **52**(21): p. 4867-4872.
25. Xu, L., et al., *Variation of non-isothermal crystallization behavior of isotactic polypropylene with varying β-nucleating agent content.* Polymer International, 2010. **59**(10): p. 1441-1450.
26. Zhou, J.-J., et al., *Atomic force microscopy study of the lamellar growth of isotactic polypropylene.* Polymer, 2005. **46**(12): p. 4077-4087.
27. Padden, F.J. and H.D. Keith, *Spherulitic Crystallization in Polypropylene.* Journal of Applied Physics, 1959. **30**(10): p. 1479 - 1484.
28. Campbell, R.A., P.J. Phillips, and J.S. Lin, *The gamma phase of high-molecular-weight polypropylene: 1. Morphological aspects.* Polymer, 1993. **34**(23): p. 4809-4816.
29. Mezghani, K. and P.J. Phillips, *The γ-phase of high molecular weight isotactic polypropylene. II: The morphology of the γ-form crystallized at 200 MPa.* Polymer, 1997. **38**(23): p. 5725-5733.
30. *The university of York, The essential chemical industry online.* http://www.essentialchemicalindustry.org/polymers/polypropene.html.
31. Nezbedova, E., A. Zahradnickova, and P. Bartaskova, *Influence of processing conditions on the structural and fracture behavior of PP pipe grades.* Journal of Macromolecular Science Part B Physics, 2007. **B41**(4-6): p. 711-723.
32. Stokes, V.K., *Joining methods for plastics and plastic composites: An overview.* Polymer Engineering & Science, 1989. **29**(19): p. 1310-1324.
33. Nguyen, T.Q., *Polymer Degradation and Stabilization*, in *Handbook of Polymer Reaction Engineering*. 2008, Wiley-VCH Verlag GmbH. p. 757-831.
34. A P Fraise, P.A.L.a.J.-Y.M., *Russell, Hugo and Ayliffe's Principles and Practice of Disinfection, Preservation and Sterilization*. 2004: Blackwell.
35. Kumar, A.B.P.a.J.K., *Drinking water disinfection techniques*. 2013: CRC press.
36. Yu, W., et al., *Deterioration of polyethylene pipes exposed to water containing chlorine dioxide.* Polymer Degradation and Stability, 2011. **96**(5): p. 790-797.
37. Deborde, M. and U. von Gunten, *Reactions of chlorine with inorganic and organic compounds during water treatment—Kinetics and mechanisms: A critical review.* Water Research, 2008. **42**(1–2): p. 13-51.
38. Brigante, M., et al., *Formation and reactivity of the dichloride radical () in surface waters: A modelling approach.* Chemosphere, 2014. **95**(0): p. 464-469.
39. Jacobi, H.W., et al., *A laser flash photolysis kinetic study of reactions of the Cl2− radical anion with oxygenated hydrocarbons in aqueous solution.* International Journal of Chemical Kinetics, 1999. **31**(3): p. 169-181.
40. Masuda, T., T. Hayashi, and M. Kondo, *Reactions of Dichloride Anion Radicals with Aliphatic Peptides in Aqueous Solutions.* Journal of Radiation Research, 1982. **23**(3): p. 298-305.
41. Hassinen, J., et al., *Deterioration of polyethylene pipes exposed to chlorinated water.* Polymer Degradation and Stability, 2004. **84**(2): p. 261-267.
42. Gill TS, K.R., Bradley WL, Bradley SW, *Long term durability of crosslinked polyethylene tubing used in chlorinated hot water systems.* Plastics, Rubber and Composites, 1999. **28**(6): p. 309-313.
43. Yu, W., et al., *Antioxidant consumption in squalane and polyethylene exposed to chlorinated aqueous media.* Polymer Degradation and Stability, 2012. **97**(11): p. 2370-2377.
44. Pospíšil, J., *Mechanistic action of phenolic antioxidants in polymers—A review.* Polymer Degradation and Stability, 1988. **20**(3–4): p. 181-202.
45. Lundbäck, M., *Long-term performance of polyolefins in different environments including chlorinated water: Antioxidant consumption and migration and polymer degradation*, in *KTH fibre and polymer technology*. 2005, KTH: Stockholm.

46. Fraser, R.D.B., *The Interpretation of Infrared Dichroism in Fibrous Protein Structures.* The Journal of Chemical Physics, 1953. **21**(9): p. 1511-1515.
47. Fraser, R.D.B., *Interpretation of Infrared Dichroism in Axially Oriented Polymers.* The Journal of Chemical Physics, 1958. **28**(6): p. 1113-1115.
48. Beer, M., *Quantitative Interpretation of Infra-Red Dichroism in Partly Oriented Polymers.* Proceedings of the Royal Society of London. Series A. Mathematical and Physical Sciences, 1956. **236**(1204): p. 136-140.
49. Brüll, R., R. Maria, and K. Rode, *Characterizing the Three-Dimensional Orientation in Polymers using FT-IR Spectroscopy with Linear Polarized Light.* Macromolecular Chemistry and Physics, 2010. **211**(20): p. 2233-2239.
50. Schuster, T., et al., *Quantification of highly oriented nucleating agent in PP-R by IR-microscopy, polarised light microscopy, differential scanning calorimetry and nuclear magnetic resonance spectroscopy.* Polymer, 2014. **55**(7): p. 1724-1736.
51. Lamberti, G. and V. Brucato, *Real-time orientation and crystallinity measurements during the isotactic polypropylene film-casting process.* Journal of Polymer Science Part B: Polymer Physics, 2003. **41**(9): p. 998-1008.
52. Nieh, J.-Y. and L. James Lee, *Hot plate welding of polypropylene. Part I: Crystallization kinetics.* Polymer Engineering & Science, 1998. **38**(7): p. 1121-1132.
53. Schuster, T., et al., *Spatially resolved monitoring of crystalline suprastructure and molecular orientation in α- and β-nucleated polypropylene pipes using differential scanning calorimetry, infrared microscopy, and polarized light microscopy.* Journal of Applied Polymer Science, 2013. **130**(6): p. 4182-4190.
54. *ASTM F2023-2010. Standard test method for evaluating the oxidative resistance of crosslinked Polyethylene (PEX) tubing and systems to hot chlorinated water. 2010; 08; 04.*
55. *DIN EN ISO 1167-1 Thermoplastics pipes, fittings and assemblies for the conveyance of fluids – determination of the resistance to internal pressure – part 1: general method. Berlin: Beuth-Verlag; 2006.*
56. Maria, R., et al., *Monitoring the influence of different weathering conditions on polyethylene pipes by IR-microscopy.* Polymer Degradation and Stability, 2011. **96**: p. 1901-1910.
57. 728, D.E., *Plastic piping and ducting systems-polyolefin pipes and fittings-determination of oxidation indcution time. Berlin: Beuth-Verlag; 1997.*
58. Koenig, J.L., *Vibrational spectroscopy of polymers*, in *Spectroscopy of Polymers (Second Edition)*. 1999, Elsevier Science: New York. p. 61.
59. Mirabella, F.M., *Surface orientation of polypropylene. I. Theoretical considerations for the application of internal reflection spectroscopy.* Journal of Polymer Science: Polymer Physics Edition, 1984. **22**(7): p. 1283-1291.
60. Bao, R., et al., *Deformation-induced morphology evolution during uniaxial stretching of isotactic polypropylene: effect of temperature.* Colloid and Polymer Science, 2012. **290**(3): p. 261-274.
61. J. Varga, G.W.E., A. K. Schlarb, *Vibration welding of alpha and beta isotactic polypropylenes: Mechanical properties and structure.* eXPRESS Polymer Letters, 2008. **2**(3): p. 148-156.
62. Oliveira, M.J., C.A. Bernardo, and D.A. Hemsley, *Morphology and mechanical behavior of polypropylene hot plate welds.* Polymer Engineering & Science, 2001. **41**(11): p. 1913-1922.
63. Schmachtenberg, E. and C. Tüchert, *Long-Term Properties of Butt-Welded Poly(propylene).* Macromolecular Materials and Engineering, 2003. **288**(4): p. 291-300.
64. Way, J.L. and J.R. Atkinson, *Some studies of deformation processes in fully-spherulitic polypropylene.* Journal of Materials Science, 1971. **6**(2): p. 102-109.
65. Petraccone, V., I.C. Sanchez, and R.S. Stein, *The orientation of amorphous chains in spherulites.* Journal of Polymer Science: Polymer Physics Edition, 1975. **13**(10): p. 1991-2029.
66. Lotz, B., J.C. Wittmann, and A.J. Lovinger, *Structure and morphology of poly(propylenes): a molecular analysis.* Polymer, 1996. **37**(22): p. 4979-4992.

67. Lovinger, A.J., J.O. Chua, and C.C. Gryte, *Studies on the α and β forms of isotactic polypropylene by crystallization in a temperature gradient.* Journal of Polymer Science: Polymer Physics Edition, 1977. **15**(4): p. 641-656.
68. Forgács, P., B.R. Tolochko, and M.A. Sheromov, *Study of the β — α solid-solid transition of isotactic polypropylene by synchrotron radiation.* Polymer Bulletin, 1981. **6**(1-2): p. 127-133.
69. Rawashdeh, S. and I.A. Raheil, *The structure of Isotactic Polypropylene Crystallized from the Melt.* Journal of Chemical Engineering & Process Technology, 2012. **3**(5): p. 140.
70. Haudin, J.-M., et al., *Shear-induced crystallization of polypropylene. Growth enhancement and rheology in the crystallization range.* Macromolecular Symposia, 2002. **185**(1): p. 119-133.
71. Brüll, R., et al., *Analysis of the Influence of Processing Conditions on the Supramolecular Structure and Antioxidant Distribution in PP-Pipes Using Infrared Microscopy.* Macromolecular Materials and Engineering, 2008. **293**(5): p. 400-408.
72. Gahleitner, M., et al., *Propylene–ethylene random copolymers: Comonomer effects on crystallinity and application properties.* Journal of Applied Polymer Science, 2005. **95**(5): p. 1073-1081.
73. Wei, Z., et al., *Crystallization and melting behavior of isotactic polypropylene nucleated with individual and compound nucleating agents.* Journal of Thermal Analysis and Calorimetry, 2010. **102**(2): p. 775-783.
74. Kang, J., et al., *Comparative study on the crystallization behavior of β-isotactic polypropylene nucleated with different β-nucleation agents —effects of thermal conditions.* Journal of Applied Polymer Science, 2014. **131**(7): p. n/a-n/a.
75. Geertz, G., et al., *Stabiliser diffusion in long-term pressure tested polypropylene pipes analysed by IR microscopy.* Polymer Degradation and Stability, 2009. **94**: p. 1092-1102.
76. Yamaguchi, M., et al., *Anomalous molecular orientation of isotactic polypropylene sheet containing N,N'-dicyclohexyl-2,6-naphthalenedicarboxamide.* Polymer, 2009. **50**(6): p. 1497-1504.
77. Grabmayer, K., et al., *Accelerated aging of polyethylene materials at high oxygen pressure characterized by photoluminescence spectroscopy and established aging characterization methods.* Polymer Degradation and Stability, 2014. **109**(0): p. 40-49.
78. Pospíšil, J., et al., *Influence of testing conditions on the performance and durability of polymer stabilisers in thermal oxidation.* Polymer Degradation and Stability, 2003. **82**(2): p. 145-162.
79. Hawkins, W.L., M.A. Worthington, and W. Matreyek, *Loss of antioxidants from polyethylene by evaporation and aqueous extraction.* Journal of Applied Polymer Science, 1960. **3**(9): p. 277-281.
80. Bertoldo, M. and F. Ciardelli, *Water extraction and degradation of a sterically hindered phenolic antioxidant in polypropylene films.* Polymer, 2004. **45**(26): p. 8751-8759.
81. Zhang, L., G. Cai, and W. Eli, *Synthesis and characterization of novel liquid ester-phenolic antioxidant based on dipentaerythritol.* Lubrication Science, 2013. **25**(3): p. 209-216.
82. Zweifel H MR, S.M., *Plastics additives handbook. 6 ed.* Hanser Publications, 2009.
83. Beißmann, S., et al., *Monitoring the degradation of stabilization systems in polypropylene during accelerated aging tests by liquid chromatography combined with atmospheric pressure chemical ionization mass spectrometry.* Polymer Degradation and Stability, 2013. **98**(9): p. 1655-1661.
84. Barret, J., et al., *A molecular study towards the interaction of phenolic anti-oxidants, aromatic amines and HALS stabilizers in a thermo-oxidative ageing process.* Polymer Degradation and Stability, 2002. **76**(3): p. 441-448.

85. Black, R.M. and B.J. Lyons, *Radiation-Induced Changes in the Structure of Polypropylene.* Proceedings of the Royal Society of London. Series A. Mathematical and Physical Sciences, 1959. **253**(1274): p. 322-330.
86. Aymes-Chodur, C., et al., *Structural and physico-chemical studies on modification of polypropylene and its polyphenolic antioxidant by electron beam irradiation.* Polymer Degradation and Stability, 2006. **91**(4): p. 649-662.
87. Koch, V.J., *Zum mechanismus der inhibierenden reaktion phenolischer antioxydantien bei der verarbeitung von polypropylen. I. Modellreaktionen von 1,3,5-trimethyl-2,4,6-tris-(3,5-di-tert.-butyl-4-hydroxybenzyl)-benzol.* Die Angewandte Makromolekulare Chemie, 1971. **20**(1): p. 7-20.
88. Rodil, R., J.B. Quintana, and R. Cela, *Oxidation of synthetic phenolic antioxidants during water chlorination.* Journal of Hazardous Materials, 2012. **199–200**(0): p. 73-81.
89. Mittelman, G., et al., *Prediction of polymer tube life for solar hot water systems: A model of antioxidant loss.* Solar Energy, 2008. **82**(5): p. 452-461.
90. Brocca, D., E. Arvin, and H. Mosbæk, *Identification of organic compounds migrating from polyethylene pipelines into drinking water.* Water Research, 2002. **36**(15): p. 3675-3680.
91. Thörnblom, K., M. Palmlöf, and T. Hjertberg, *The extractability of phenolic antioxidants into water and organic solvents from polyethylene pipe materials - Part I.* Polymer Degradation and Stability, 2011. **96**(10): p. 1751-1760.
92. Viebke, J., M. Hedenqvist, and U.W. Gedde, *Antioxidant efficiency loss by precipitation and diffusion to surrounding media in polyethylene hot-water pipes.* Polymer Engineering & Science, 1996. **36**(24): p. 2896-2904.
93. Crank, J., *The mathematics of diffusion*. 1975, London: Oxford university press.
94. Carlslaw HS, J.J., *Conduction of heat in solids*. 2nd ed. 1959: Oxford university press.
95. Ilja N. Bronshtein, K.A.S., Gerhard Musiol, Heiner Muehlig, *Differential Equations*, in *Handbook of Mathematics*. 2007, Springer Berlin Heidelberg. p. 487-551.
96. Adams, J.H. and J.E. Goodrich, *Analysis of nonvolatile oxidation products of polypropylene. II. Process degradation.* Journal of Polymer Science Part A-1: Polymer Chemistry, 1970. **8**(5): p. 1269-1277.
97. Hedenqvist, M. and U.W. Gedde, *Diffusion of small-molecule penetrants in semicrystalline polymers.* Progress in Polymer Science, 1996. **21**(2): p. 299-333.
98. Frank, H.P. and H. Lehner, *Distribution of ultraviolet stabilizers in crystalline polypropylene.* Journal of Polymer Science Part C: Polymer Symposia, 1970. **31**(1): p. 193-203.
99. Billingham, N.C., P. Prentice, and T.J. Walker, *Some effects of morphology on oxidation and stabilization of polyolefins.* Journal of Polymer Science: Polymer Symposia, 1976. **57**(1): p. 287-297.
100. Saleem, M., et al., *Diffusion of organic penetrants through low density polyethylene (LDPE) films: Effect of size and shape of the penetrant molecules.* Journal of Applied Polymer Science, 1989. **37**(3): p. 617-625.
101. Asfour, A.-F.A., et al., *Diffusion of saturated hydrocarbons in low density polyethylene (LDPE) films.* Journal of Applied Polymer Science, 1989. **38**(8): p. 1503-1514.
102. Földes, E., *Mobility of additives in ethylene polymers.* Polymer Bulletin, 1995. **34**(1): p. 93-99.
103. Möller, K. and T. Gevert, *An FTIR solid-state analysis of the diffusion of hindered phenols in low-density polyethylene (LDPE): The effect of molecular size on the diffusion coefficient.* Journal of Applied Polymer Science, 1994. **51**(5): p. 895-903.
104. Eby, R.K., *Diffusion in a Polymer With Lamellar Morphology, Polyethylene.* Journal of Applied Physics, 1964. **35**(9): p. 2720-2724.
105. Moisan, J.Y., *Diffusion des additifs du polyethylene—III: Influence de l'orientation.* European Polymer Journal, 1980. **16**(10): p. 997-1002.

106. Moisan, J.Y., *Diffusion des additifs du polyethylene—IV: Etude de materiaux-modeles.* European Polymer Journal, 1981. **17**(8): p. 857-864.
107. Schlotter, N.E. and P.Y. Furlan, *A review of small molecule diffusion in polyolefins.* Polymer, 1992. **33**(16): p. 3323-3342.
108. Masoud, H. and A. Alexeev, *Permeability and Diffusion through Mechanically Deformed Random Polymer Networks.* Macromolecules, 2010. **43**(23): p. 10117-10122.
109. Duvall, D., *Oxidation Resistance of Polypropylene Random Copolymer Pipe to Chlorinated Water.* Journal of Failure Analysis and Prevention, 2014. **14**(3): p. 336-342.
110. Rjeb, A., et al., *IR spectroscopy study of polypropylene natural aging.* Journal of Applied Polymer Science, 2000. **77**(8): p. 1742-1748.

Subin Damodaran

August-Metz-Weg 3
64297 Darmstadt

30. April 2015

Eidesstattliche Erklärung

Ich erkläre hiermit, dass ich meine Dissertation selbstständig und nur mit den angegebenen Hilfsmitteln angefertigt habe.

Subin Damodaran

Subin Damodaran

August-Metz-Weg 3
64297 Darmstadt

30. April 2015

Erklärung

Ich erkläre hiermit noch keinen Promotionsversuch unternommen zu haben.

Subin Damodaran

Subin DAMODARAN

Apartment 282, August-Metz-Weg 3, 64297 Darmstadt

Phone: +49 17631042515

E-mail: subin.damodar@gmail.com

Date and place of birth: 10 Apr 1986, Kerala, India

Professional Experience:

Product Specialist Jan 2016	**Tosoh Bioscience GmbH, Griesheim Darmstadt, Germany**
Scientific Assistant Jan 2012 - Jan 2015	**Fraunhofer Institute for Structural Durability and System Reliability LBF, Darmstadt, Germany**
Junior Research Fellow Jun - Dec 2011	**Mar Athanasios College for Advanced Studies Thiruvalla, India**

Thesis Works:

Master of Science Mar - Aug 2010	**University of Rouen, France** [Material Science] **Title:** Green Composites, by using wheat and rice flour thermoplastic matrices reinforced by natural fibers
Master of Philosophy Mar - Sep 2009	**University of South Brittany, France/M. G. University, India** [Chemistry] **Title:** Synthesis and Characterization of PMMA & PS Nanocomposites with CdS Quantum dots
Master of Science Jan - Jun 2008	**Central Salt & Marine Chemicals Research Institute, India** [Chemistry] **Title:** Engineering of hydrogen bonded molecular adducts derived from exobidentate N-donor ligands with dicarboxylic acids: synthesis, characterization and single crystal investigation

Educational Qualification:

Doctor of Philosophy Since Jan 2012	**Technical University of Darmstadt, Germany** [Chemistry]
Master of Philosophy Oct 2008- Sep 2011	**Mahatma Gandhi University, Kerala, India** [Chemistry]
Master of Science Sep 2009- Aug 2010	**University of Rouen, France** [Material Science]
Master of Science Aug 2006- Jun 2008	**Mahatma Gandhi University, Kerala, India** [Chemistry]
Bachelor of Science Jun 2003- Apr 2006	**Mahatma Gandhi University, Kerala, India** [Chemistry]

Publication:

S. Damodaran et. Al. Polymer (2015) 60, 125-136

S. Damodaran et. Al. Polym. Degrad. Stab. (2015) 111, 7-19

Subin Damodaran **Darmstadt, 30 March 2016**